Improving the electrocatalytic abilities for CO2 reduction via functionalization with a redox-active metal complex

著者	HABIB Md. Ahsan
学位授与機関	Tohoku University
学位授与番号	11301甲第18270号
URL	http://hdl.handle.net/10097/00124054

Doctoral Thesis

Improving CO_2 reduction electrocatalytic abilities via functionalization with a redox-active metal complex

(酸化還元活性金属錯体を用いた二酸化炭素還元電極触媒能の向上)

Habib Md. Ahsan

2018

Acknowledgements

First of all I want to thank Professor Masahiro Yamashita for giving me the opportunity to come to Japan to work in an interesting project. I am very grateful to my Professor Masahiro Yamashita for his guidance and suggestions on how to improve my research. Especially, I would like to thank Associate Professor Brian K. Breedlove for his commitment to guide me and advise me through the challenging periods of the project. I also appreciate a lot the opportunity they have given me to present my work in national and international conferences where I have learned a lot. This work carried out at the Department of Chemistry, Tohoku University, and was financially supported by MEXT.

I enjoyed myself very much a highly professional and friendly environment at Coordination Chemistry Laboratory. It was a great experience to work with everyone. In particular, I have to thank Dr. Shinya Takaishi, Dr. Keiichi Katoh, Dr. Hiroaki Iguchi and Dr. Ryo Nakanishi. I would like to thank Dr. Goulven Cosquer for solving crystal structure. I really want to thank Emi Nitto, Sawako Mizuma and Ayako Sakurai for make my life easier in sendai and helping for all official work.

I would like to thank Dr. Shunsuke Mochizuki for helping GC-Mass measurements at Instrumental Analysis Group, Graduate School of Engineering, Tohoku University.

I would like thank Mritunjoy Kamila, Ahmed Fatoh, Ramji Kandle, Takafumi Yoshida and Yuji Horii for their helping and encouragement. I would like to thank Dr. Kanchan Chakma, Mohammad Aftabuzzaman, Abdul Lotif and Unjila Afrin, Dr. Soumava Biswas, Dr. Leena Mondal and especial thank to Mohammad Rasel mian that have been there for me all this time.

I also had the opportunity to work with a number of funny and talented students: Tsutomu Yamabayashi, Yongbing Shen, Liyuan Qu, Saiful Islam, Satoshi Ito, Tetsu Sato, Jun Suzuki, Hideaki Murasugi, Wu Chaojan, Hsiao Hsin-Ning, Kaiji Uchida, Syohei Koyama, Kentaro Fuku, Yui Fujihara, Clement Yohan, Haruna Taniguchi, Ea Nakagawara, Hirotaka Nakajima, Michiyuki Suzuki, Kon Kazuki, Shuntaro Yamanaka and especial thank to Piangrawee Santivongskul Erk.

In addition to those who had a scientific impact on my career, I am thankful for the presence of the many people who supported me on a personal level throughout.

Finally, I would like to thank my elder brother Dr. Shofiur Rahman for continuous support and encouragement. I want to thank all of my family members that, regardless of the distance, have been a part of my life. You have been a great support through the effortful times and I devote this thesis to you.

Habib Md. Ahsan

2018

List of abbreviations

bpy: 2,2’-bipyridine

qlca: Quinoline-2-carbaldehyde(pyridine-2-carbonyl)hydrazine

$TBAPF_6$: tetrabutylammonium hexafluorophosphate

[Ru]: $[Ru(bpy)_2Cl]^+$

py: 4-pyridal

pic: 4-methylpyridyl

nic: isonicotinoyl

E_{app}: applied potential

$E^{o}_{CO_2/CO}$: standard reduction potential of CO_2 to CO

FE: Faradaic efficiency

η: overpotential

TOF: turnover frequency

k_{cat}: catalytic rate constant

[cat]: catalyst concentration

CPE: control potential electrolysis

F: Faraday constant

R: universal gas constant

T: temperature

Cyclen: 1,4,7,10-Tetraazacyclododecane

Cyclam: 1,4,8,11-Tetraazacyclotetradecane

Abstract

Electrochemical carbon dioxide reduction is a promising way for the synthesis of carbon based chemical or chemical precursors. Efficient electrocatalyst that selectively reduce carbon dioxide at lower overpotential are needed. Research in this area already explored and the majority of the work focuses to improving electrocatalytic abilities such as high selectivity and low overpotential. This thesis began with the modification of electrocatalysts by tethered with ligand-coordinated redox-active metal complex ($\{Ru(bpy)_2\}^{2+}$, bpy = 2,2'-bipyridine). During electrolysis, ligand-coordinated redox-active metal complex reduce before electrocatalytic active site and increase electron density to improved CO_2 reduction abilities.

A ditopic planar pseudo-pincer ligand supported nickel based electrocatalyst modified by attaching ligand-coordinated redox-active metal complex and investigated the reduction abilities of carbon dioxide to carbon monoxide. Electrocatalytic results suggest that the ligand-coordinated redox-active metal complex tethered electrocatalyst improved turnover frequency by utilize electron influence from redox-active ligand and decreased overpotential due to the inductive effects of Ru^{2+} ions on catalytic active site.

Nickel cyclen metal complex modified by tethered ligand-coordinated redox-active metal complex via 4-methylpyridal linker. Electroanalytical investigation of electocatalysts suggest that the ligand-coordinated redox-active metal complex enhance carbon dioxide reduction abilities of nickel cyclen electrocatalysts. Ligand-coordinated redox-active metal complex reduce before catalytic active site and transferred electron to enhance catalytic activity and allow to decrease overpotential. In other words, ligand-coordinated redox-active metal complexes tethered to an electrocatalytic active site is a new way of improving CO_2 reduction abilities.

Table of Contents

Chapter 3 Enhancement of electrocatalytic abilities of a modified Ni(cyclen) complex towards CO_2 reduction……………………………………………………………………………78–118

List of Tables

List of figures

Chapter 1

General Introduction

1.9 Fossil fuels and carbon dioxide

The earth's atmosphere is out of balance from simple chemical equilibrium due to excess amount carbon dioxide (CO_2).[1,2] The Industrial Revolution took off in the 18th century, and fossil fuels (oil, coal and natural gas) seemed to be the ideal energy source. Moreover, transportation uses to large amount of energy consuming sector.[3,4] Global fossil fuel consumption is increasing

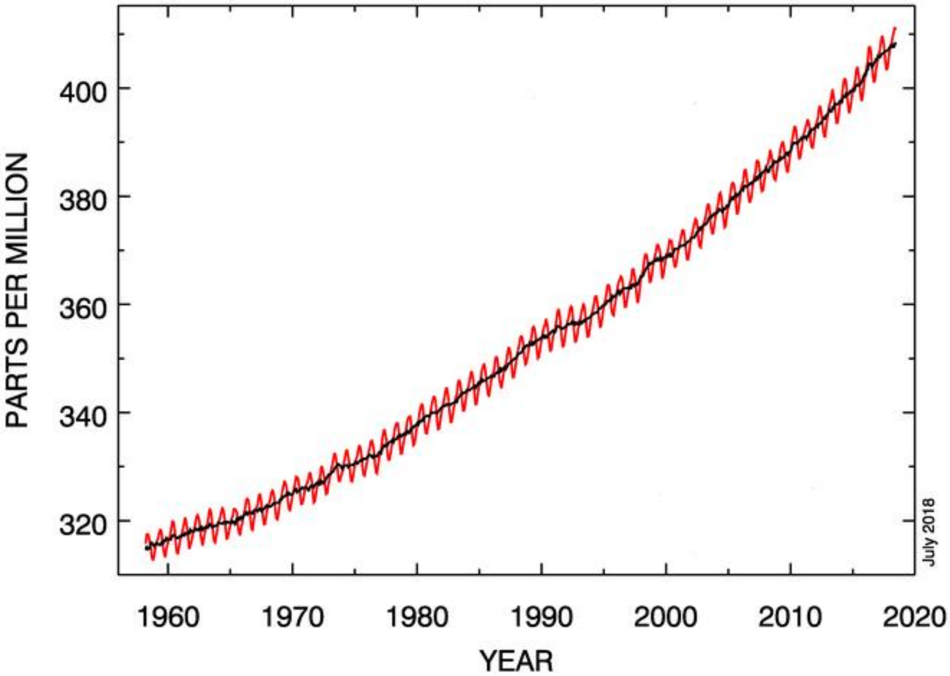

Figure 2.1: Atmospheric CO_2 concentration at Mauna Loa Observatory. Figure taken with permission from Ref. 3.

dramatically, and CO_2 is an unsustainable by-product of all process involving oxidation of fossil fuels.

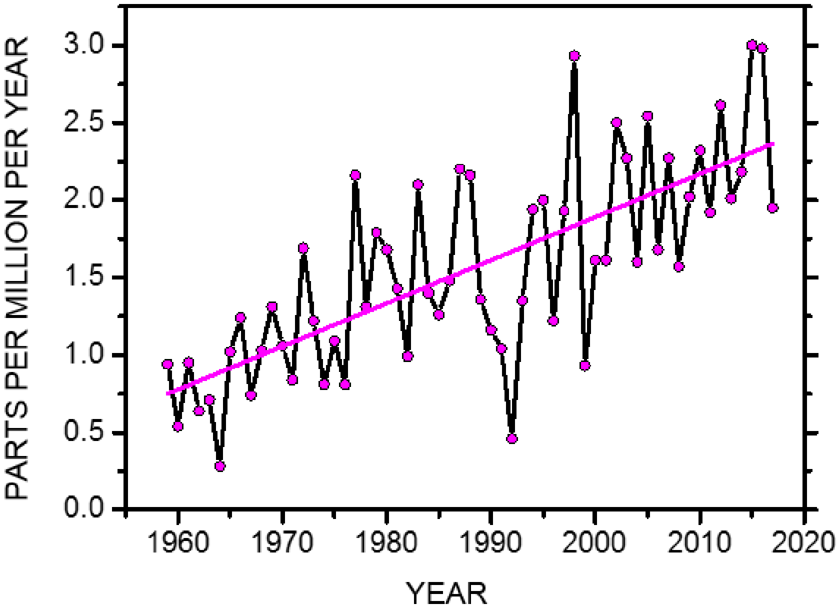

Figure 1.2: Atmospheric CO_2 concentration increasing trends from 1959 to 2017. Figure is reproduced from Ref. 4.

As a result, the CO_2 concentration in the atmosphere has increased from 280 to 410 ppm,[5] and the rate of increase is about 2 ppm per year (Figure 1.2). The global concentration of CO_2 in the atmosphere is 410.79 ppm (July, 2018),[6] which is higher than the level thought safe for living organisms (350 ppm). The concentration of CO_2 in the atmosphere will continue to increase in the future and therefore, the excess CO_2 in the atmosphere, which is a primary greenhouse gas is contributing to an increase in the global average temperature. On the other hand, the main energy source is still fossil fuels, and resources are limited. At the same time, good methods for reducing atmospheric CO_2 levels are needed. Promising solutions to reduce atmospheric CO_2 level by using

CO_2 capture and conversion to fuel precursors through electrochemical reduction are being developed.

1.10 Electrochemical and electrocatalytic reduction of CO_2

CO_2 is a potential starting material for many organic chemical, such as urea, synthesis gas, acetic acid, etc. In nature, conversion of CO_2 to chemicals occurs via photosynthesis. There are several methods for converting CO_2 to fuels and chemicals, such as, electrochemical reduction, electrocatalytic (homogeneous and heterogeneous) reduction and photocatalytic reduction.[7] The direct and uncatalyzed electrochemical reduction of linear CO_2 to bent $CO_2^{\cdot-}$ anion by an outer-sphere single electron transfer from inert (outer sphere) electrode needs large reorganization energy. The large reorganization energy between linear CO_2 and bent $CO_2^{\cdot-}$ anion leading very negative equilibrium potential ($E^o = -1.9$ V vs. NHE).[8–10] However, the conversion of CO_2 needs to meet two significant criteria, high energy efficiency and high reaction rates.[11]

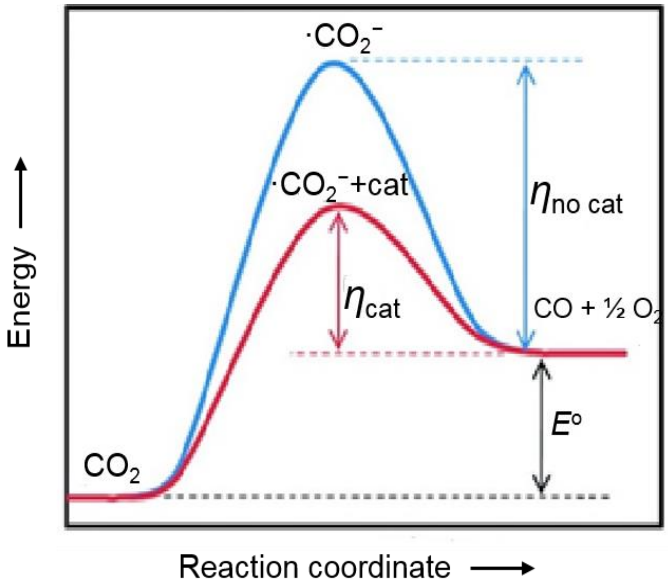

Figure 1.3: Reaction scheme for electrochemical conversion of CO_2. Figure is reproduced from Ref. 11

A high energy efficient system is obtained, when the process occurs at low overpotentials (η), which is a thermodynamic parameter defined as the difference between the applied potential and the standard potential for the formation of CO_2 reduction product from CO_2,[12] with high selectivity. Therefore, electrocatalysts must increase the selectivity and conversion rate at low η. In elecrocatalytic systems, electrocatalysts act as a shuttle between the working electrode and CO_2,[13] and the reduction carried out at the potential of the electrocatalyst. Therefore, electrocalaysts can operate less negative potential then electrochemical process.[14] The electrocatalysts play a vital role to transfer electron from electrode to CO_2 and increase chemical reaction rates. A good electrocatalysts should be able to operate near the thermodynamic potential of the reaction, E^o (product/substrate). In order to decrease η, elecrocatalysts should be operate that E^o ($[cat]^{2+}/[cat]^{1+}$) is closed to E^o (product/substrate).[8] In other words, a variety metal ions and ligands can be used to prepare a complex with E^o (cat) close to E^o (substrate/product).

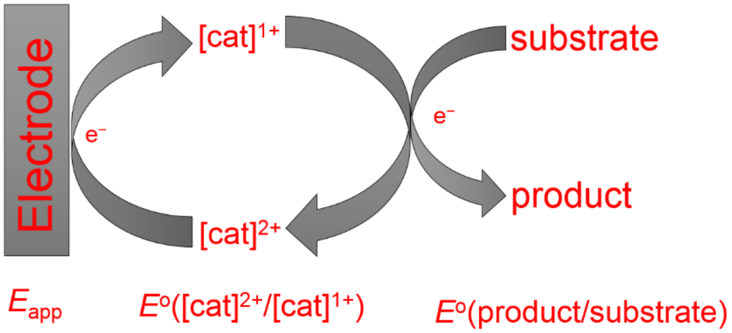

Figure 1.4: Electrocatalytic process diagram with electron source (electrode) and electrocatalyst. Figure is reproduced from Ref. 8.

1.11 Basic chemistry of carbon dioxide

Carbon is the central atom with two terminal oxygen atoms in CO_2 molecule. Carbon and both oxygen atom has 2s and 2p atomic orbital. The molecular orbital of $1\pi_g$ and $2\pi_u$ orbitals represent HOMO and LUMO, respectively. CO_2 is a linear molecule, and the C=O bond distance is 1.16 Å.[15] Due to the difference in the electronegativities of C and O in CO_2, the C=O bond is polar. However, since the molecule is linear there is no dipole moment. A molecular orbital energy level diagram is given in Figure 1.4.[16–18] CO_2 is a sixteen bonding electron in its valence shell with linear structure, and adopts $D_{\infty h}$ symmetry.

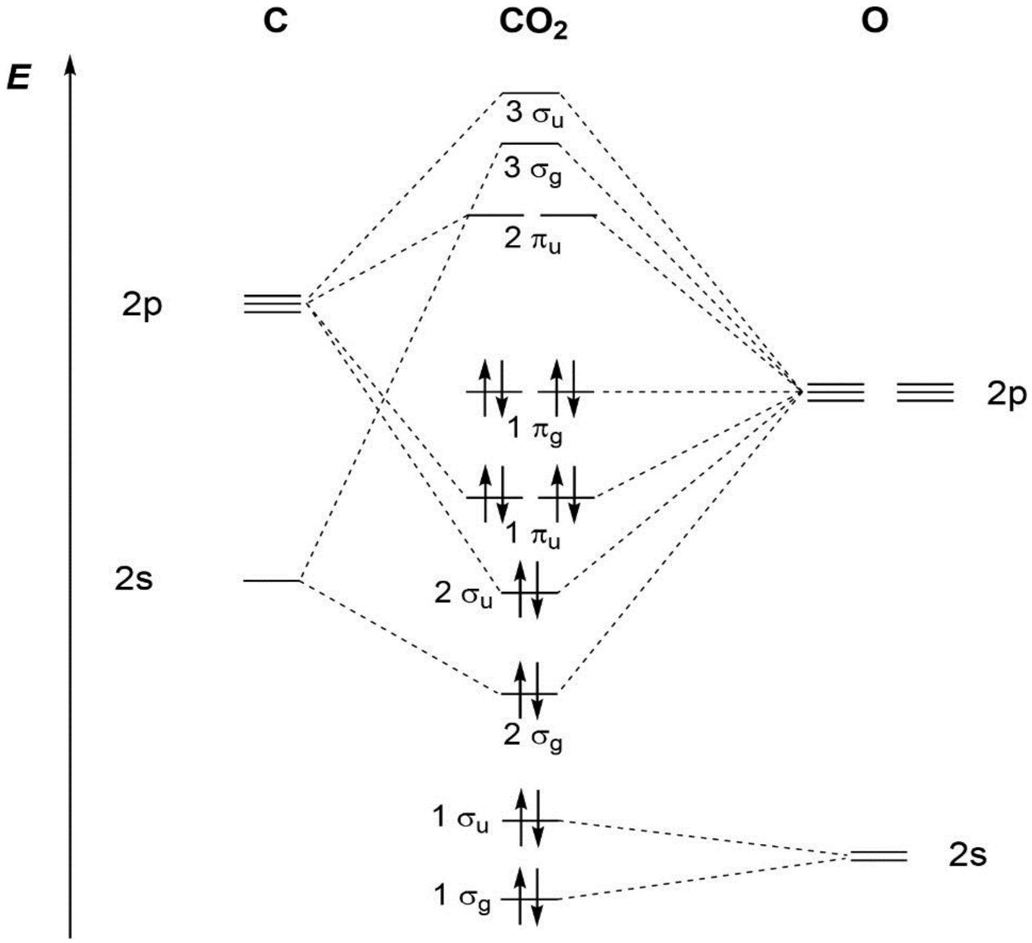

Figure 1.5: Molecular orbital diagram of CO_2. Figure taken Ref. 19

The $1\pi_g$ nonbonding molecular orbital are doubly occupied and mainly localized at the terminal oxygen atom. However, the $2\pi_u$ antibonding orbital are unoccupied and centered on the carbon atom. Therefore, CO_2 can be able to react both as a base and as an acid. The carbon atom act as a Lewis acidic center and the oxygen atom act as a Lewis basic character.[19] The best electronic representation of CO_2 is $O^{-\delta}–C^{+2\delta}–O^{-\delta}$, suggesting the nucleophilic attack at carbon and electrophilic attack at oxygen are favorable. The ionization potential of CO_2 is 13.78 eV (vs 12.6 for water, 10.0 for ammonia),[20,21] meaning that CO_2 is a better acceptor than donor and that the reactivity of the molecule is dominated by the electrophilic character of the carbon atom rather the weak nucleophilic character of the oxygen atoms. When the LUMO orbitals of CO_2 are the filled via an electron transfer, the HOMU orbitals with its strongly localized electron density as oxygen in-plane lone pairs is conductive to interaction with electrophile and the resulting lowest energy state corresponds to a bent geometry. A large amount of energy is needed for activating CO_2, meaning that a large negative potential is needed. After one electron reduction CO_2 becomes $CO_2^{\bullet-}$, which is bent with an equilibrium angle of 134°.[22] Those, two electron reduction of CO_2 is more favorable. The electrochemical conversion of CO_2 can proceed via two, four, six and eight-electron processes.[23] Affording, carbon monoxide (CO), formic acid or formate ($C_2O_4H_2/C_2O_4^{2-}$), formaldehyde (CH_2O) and methanol (CH_4), respectively. Methane (CH_4), ethane (CH_2CH_2) and ethanol (CH_3CH_2OH) are energetically more difficult to generate. The corresponding standard reduction potential for aqueous solution (pH 7 in aqueous solution versus NHE, 25 °C, 1 atm of H_2, the H_2/H^+ couple is −0.42 V). The reduction processes strongly depend on the pH and the number of electrons (eq. 2−7) for the half-reactions as shown below.[8,18,19,23]

CO_2 (aq) + e^- → $CO_2^{\bullet-}$ (aq) $E^o = -1.9$ V (eq. 1)

CO_2 (g) + $2H^+$ + $2e^-$ → CO (g) + H_2O $E^o = -0.52$ V (eq. 2)

CO_2 (g) + H^+ + $2e^-$ → HCO_2^- (aq) $E^o = -0.43$ V (eq. 3)

CO_2 (g) + $4H^+$ + $4e^-$ → HCHO (aq) + H_2O $E^o = -0.51$ V (eq. 4)

CO_2 (g) + $6H^+$ + $6e^-$ → CH_3OH (aq) + H_2O $E^o = -0.38$ V (eq. 5)

CO_2 (g) + $8H^+$ + $8e^-$ → CH_4 (aq) + $2H_2O$ $E^o = -0.24$ V (eq. 6)

Again, one electron reduction of CO_2 (eq. 1) requires a large negative potential due to a large reorganizational energy between the linear molecule and bent radical anion.[24] However, the multi electron couple multi proton reactions are required relatively low negative potential (eq. 2−6)

1.12 Coordination chemistry of carbon dioxide

The coordination of CO_2 to a metal center occurs three major modes, such as η^1−C, η^2(C,O) and η^1−O binding modes.[25] Electron-rich metal ions prefer η^1−C type coordination because of strong charge transfer the between metal center and the antibonding π^* orbital of CO_2. In this case, CO_2 binds to the metal center as Lewis acid through C atom.[13] [Rh(diars)$_2$(Cl)(CO_2)] (diars = *o*-phenylene-bis(dimethyl)arsine) was the first reported stable complex with CO_2 coordinated in η^1−C type.[26] Aresta and co-workers were the first to report a structure with CO_2 in the η^2(C,O) type fashion mode in [Ni(PCy$_3$)$_2$(CO_2)].

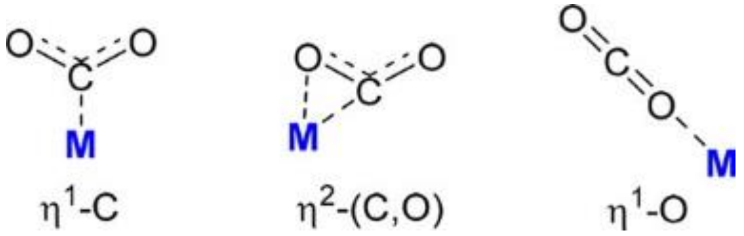

Figure 1.6: Carbon dioxide coordination mode on metal center. Figure reproduce from Ref. 13

In both mode, the CO_2 molecule is bent.[27] Although, the first example of η^2(C,O) type coordination mode showed nickel complex, Sakaki et al. have reported that $[Ni^{I}F(NH_3)]^0$ can bind CO_2 is an η^1−C mode.[28] From recent theoretical studies, the η^1−C type coordination mode is energetically more favorable for $[Ni(cylam)]^+$.[29–34] In η^1−O type coordination modes, the CO_2 bind to electron poor metal ions through an O atom. Mayer and co-workers reported the first η^1−O type coordination mode, which is very rare.[35]

1.13 Benchmarking of electrocatalysts for CO_2 reduction

Electrocatalytic abilities are describe with various metrics, such as faradaic efficiency (FE), overpotential (η), turnover frequency (TOF), catalytic rate constant (k_{cat}) and catalytic tafel plot.[18,36–41] However, the measurement conditions, such as reference electrode, working electrode, solvent, electrolyte and proton source can vary from case to case. Therefore, direct comparison between electrocatalysts is difficult. However, important information about electrocatalytic abilities are obtained.

Faradaic efficiency (FE): Faradaic efficiency describe the selectivity of electrocatalysts towards a particular reduction product from CO_2, and it is defined as a ratio of the number of moles CO_2 reduction product and the number of mole of charge passed during electrocatalysis experiment. A high faradaic efficiency for a reduction product (100%) indicates that an electrocatalyst is highly selective. However, it does not provide information about electrocatalytic activity.

Overpotential (η): The overpotential (η) describe the extra potential needed to drive the reaction at specific rate. In general, it is the deference between the applied potential for electrolysis and the standard potential for the reduction of CO_2.[12]

Turnover frequency (TOF): The turnover frequency (TOF) is a kinetic parameter that gives information about catalytic activity. In general, TOF is defined as the number of moles of product produces per mole of catalyst per unit time. In general, TOF describes the activity of the catalyst molecule present in the reaction-diffusion layer at the working electrode.[41] Therefore, TOF does not give information about the bulk solution. TOF values are calculated from cyclic voltammograms (construction for catalytic tafel plot) and control potential electrolysis (CPE) experiments. In this work, TOF values were calculated similarly. The TOF values were calculated from (CPE) data using the equation reported by Saveant co-workers and modified by McCrory *et al*.[42−44]

$$\mathrm{TOF} = \frac{(i_{el})^2\left(1+exp\left[\frac{F}{RT}\left(E_{app}-E_{\frac{1}{2}}\right)\right]\right)}{F^2A^2D[cat]^2}$$

where i_{el} is average current of CPE for reduction product generation (A), F is Faraday constant, R is the universal gas constant, T is the temperature, E_{app} is the applied potential during CPE, $E_{1/2}$ is the standard redox potential of catalyst, A is the surface area of working electrode, D is the diffusion coefficient for catalyst and [*cat*] is the concentration of catalyst in solution.

Catalytic rate constant (k_{cat}): The catalytic rate (k_{cat}) represents the overall rate of homogeneous catalystalysis and the value determined from CV data.[18,38,45,46] The k_{cat} and TOF are equal when the applied potential is sufficiently negative of the redox couple, where the electrocatalytic process only occurs and TOF becomes $\mathrm{TOF}_{\mathrm{max}}$. The CV showed S-shaped wave at high scan rate, meaning no other electrochemical process is occurred and k_{cat} can be determined by following equation:

$$k_{\mathrm{cat}} = \left(\frac{i_{\mathrm{plateau}}}{i^0_{peak}}\right)^2 \times \frac{1}{(2\times 2.24)^2} \times \frac{Fv}{RT}$$

where i^0_{peak} is the noncatalytic current, F is the faraday constant, v is the scan rate of noncatalytic current (0.1 v/s), R is the universal gas constant and T is the temperature.

Catalytic tafel plot: The ideal method for comparing electrocatalysts is catalytic tafel plot introduced by Saveant and Costentin,[47] which shows the relationship between TOF as a function of η. A good catalyst is defined as having a high TOF at low η. In additional, TOF_0 represents the TOF value when $\eta = 0$, and is extrapolated from the plot. The catalytic tafel plot describes how fast a catalytic system can be driven in terms of TOF at a given η.

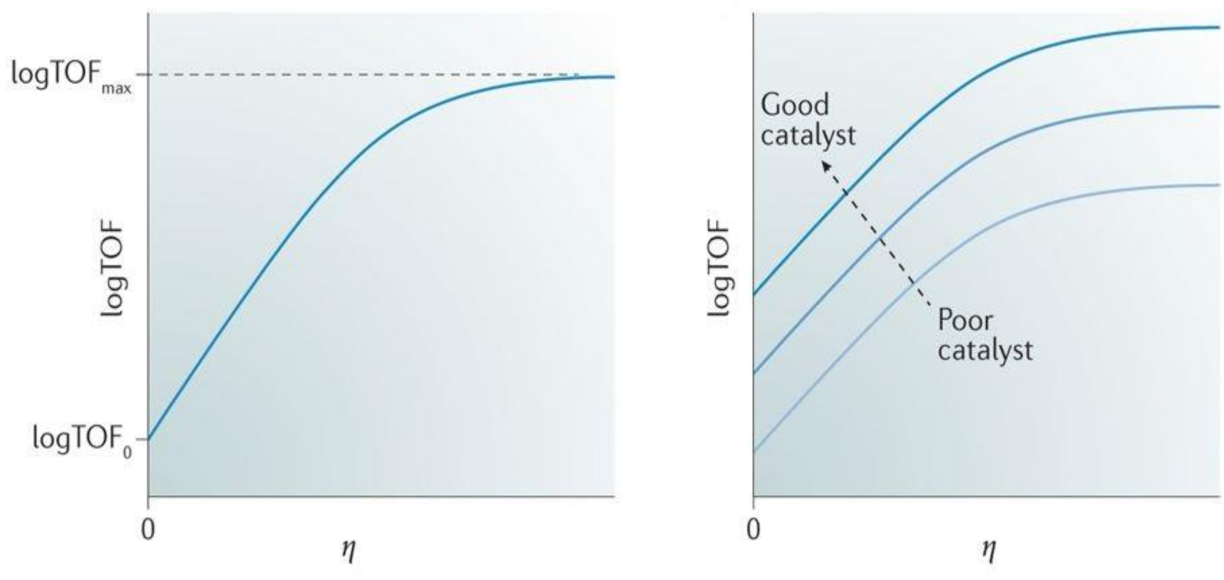

Figure 1.7: Left side: A typical catalytic Tafel plot is a graph of log TOF vs. η. At $\eta = 0$, the TOF value of TOF_0. At sufficient high η, the TOF value of TOF_{max}. Right side: The catalytic tafel plot of a good catalyst lies upwards and to the left of a poor catalyst. Thus, for a given TOF, a good catalyst will operate at a lower η. Figure taken with permission from Ref. 47.

1.14Previous strategy to improved catalytic activity

Eisenberg and co-workers reported the first tetraazomacrocylic complex of cobalt and nickel complexes for CO_2 reduction electrocatalysts.[48] These electrocatalysts are able to reduce CO_2 to

CO. However, elecrocatalytic abilities are poor. At that time, the main goal was to improved electrocatalytic abilities for CO_2 reduction. In 1991, Saveant and his group reported an iron(0)porphyrins electrocatalysts for CO_2 reduction.[49] The electrocatalytic reactivity is poor, and the complex is unstable. The electrocatalytic reactivity and activity is reported to increase after adding Mg^{2+} cation, which breaking of the CO_2 bound to iron. Later, Kubiak and co-worker utilized Mg^{2+} cation as Lewis acid to increase the catalysis rate at low overpotential for [Mn(mesbpy)$(CO)_3(CH_3CN)$](OTf) (mesbpy: 6,6'-dimesityl-2,2'-bipyridine and OTf: trifluoromethanesulfonate) electrocatalyst.[45] The electrocatalysts are operate at a high rate with a low overpotential (0.3 to 0.45 V). However, there are some disadvantages to using Mg^{2+} cations in electrolysis process, with the main being the disproportionation of CO_2 to CO and insoluble $MgCO_3$.

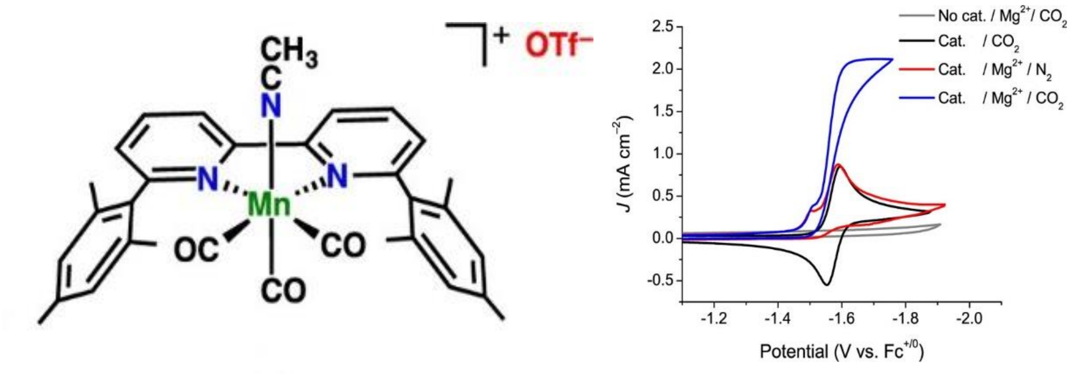

Figure 1.8: Left side: Schematic diagram of [Mn(mesbpy)$(CO_3)(CH_3CN)$](OTf) and right side: Cyclic voltammograms of 1 mM [Mn(mesbpy)$(CO_3)(CH_3CN)$](OTf) with Mg^{2+} cations. Figure taken from Ref. 45

Another strategy for improving CO_2 reduction is to utilize a proton source, and this has been explored by Saveant and co-workers.[50] They have found that iron(0)porphyrins could be utilized in the presence of weak Bronsted acids as a proton source, for the reduction of CO_2 to CO without formation of H_2. The electrocatalysts significantly improved efficiency and stability. Proton sources include 1-propanol, trifluoroethanol, methanol, phenol, trifluoroacetic acid and water and promote faster C−O bond cleavage.[43,45−52] The proton source play a vital role in CO_2 electrocatalytic reduction. During catalysis process, CO_2 molecule bind the electron rich metal center and push electron density into the CO_2 ligand at this stage protons facilitate the electron transfer by pulling out electron density, which leading to C−O bond cleavage and produce water. [Mn(mesbpy)(CO_3)(CH_3CN)](OTf) are highly active towards CO_2 reduction in the presence of 1.4 M trifluoroethanol (TFE), with TOF of 5000 s^{-1} at η 0.9 V. It should be noted that, there was no catalytic activity found without a proton source present.[52]

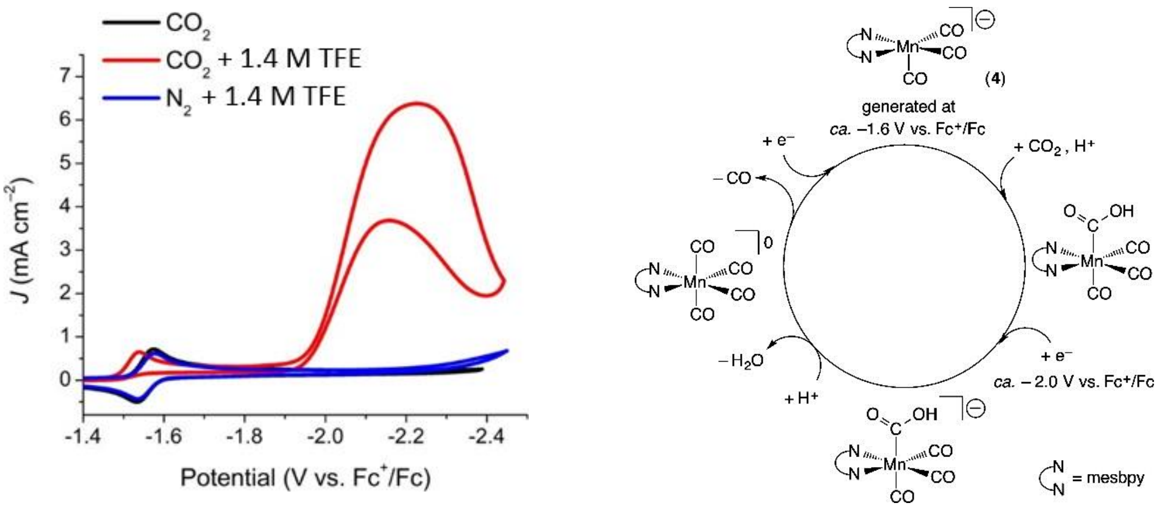

Figure 1.9: Left side: cyclic voltammograms of [Mn(mesbpy)(CO_3)(CH_3CN)](OTf). Right side: proposed catalytic mechanism of [Mn(mesbpy)(CO_3)(CH_3CN)](OTf) for CO_2 reduction in the presence of TFE as a proton source. Figure taken from Ref. 52

Attaching, the proton source near the active site has also been shown to improve the elecrocatalytic activity towards CO_2 reduction. Local proton sources increase proton concentration more than external proton source (water, methanol, trifluoroethanol or phenol) does and accelerates the electrocatalysis.[43,53−55] Similar effects have been observed when H−bond sites are available on the ligand. Co−H or $Ni-N_4$ (4-member azamacrocycle) electrocatalysts with N−H group has a stabilizing effect on M−(η^1−C) CO_2 intermediate via H−bond donation and increase the local proton concentration.[56,57]

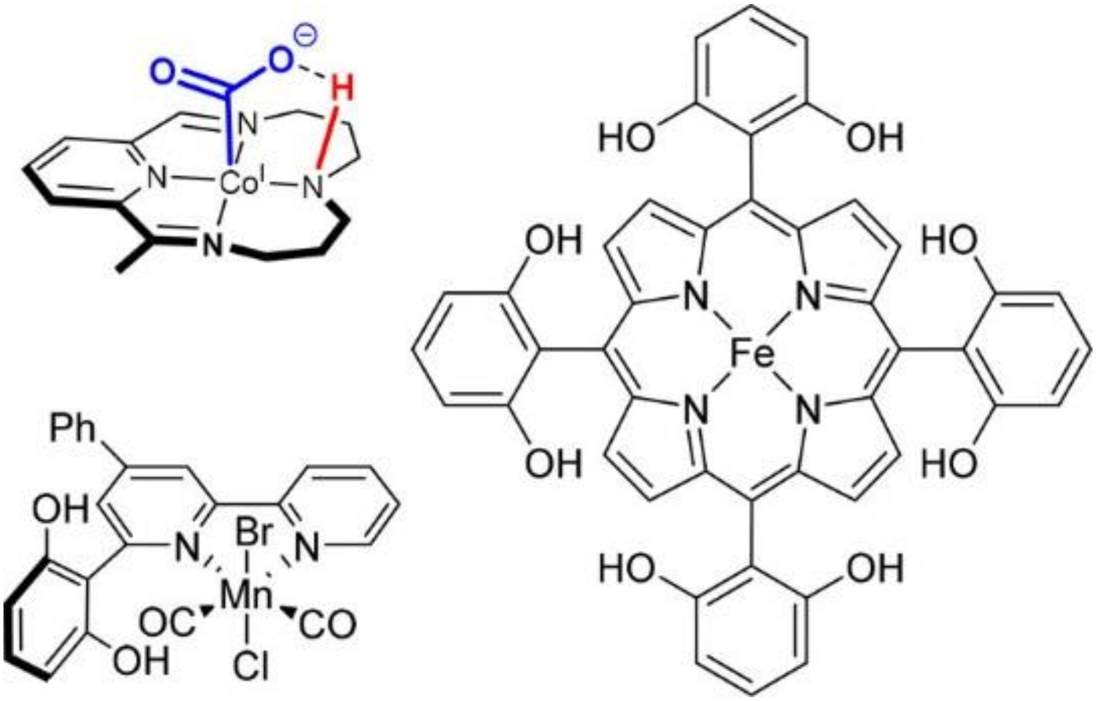

Figure 1.10: Electrocatalysts modified with local proton sources. Top left: macrocyclic cobalt complex bearing N−H group. Bottom left: [$Mn(pdbpy)(CO)_3Br$] (pdbpy: 4-phenyl-6-(phenyl-2,6-diol)-2,2’-bipyridine) bearing a bipyridyl derivative with OH groups. Right side: Iron 5,10,15,20-tetrakis(2’,6’-dihydroxylphenyl)-porphyrin bearing phenolic groups in ortho and ortho’ positions. Figure taken from Ref. 13

An interesting strategy for improving electrocatalysts involves the introduction of positively charged trimethylanilinium groups which exert inductive effects on the active site, could lowering the $E_{1/2}$ of the electrocatalyst and those η.[58]

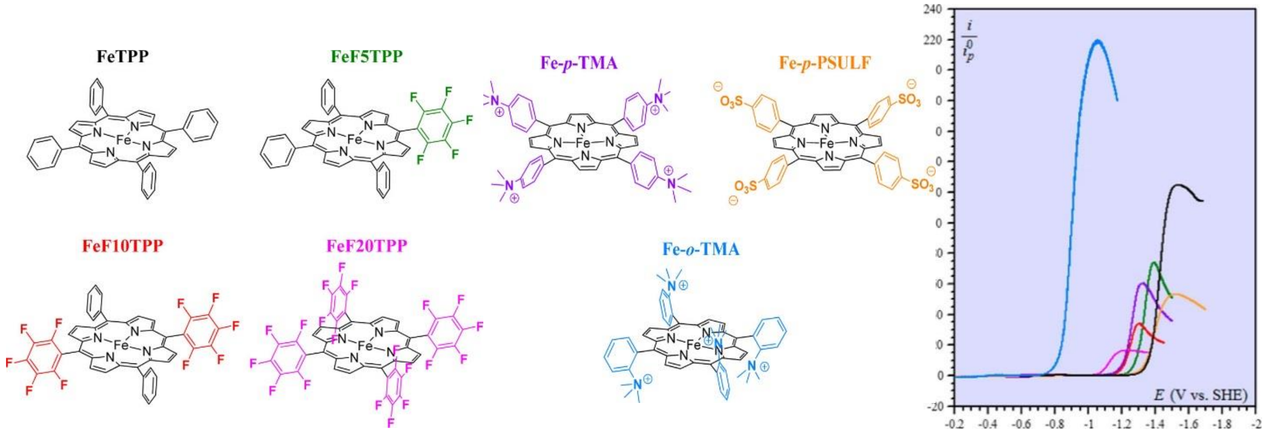

Figure 1.11: Cyclic voltammograms of a series of the substituted iron(0)tetraphenylporphyrins electrocatalysts. Figure taken from Ref. 58

Redox inactive Lewis acidic cation such as Na^+, K^+, Ca^{2+}, Sr^{2+} and Ba^{2+} have been used to tune $E_{1/2}$ of electrocatalysts in a similar manner.[59]

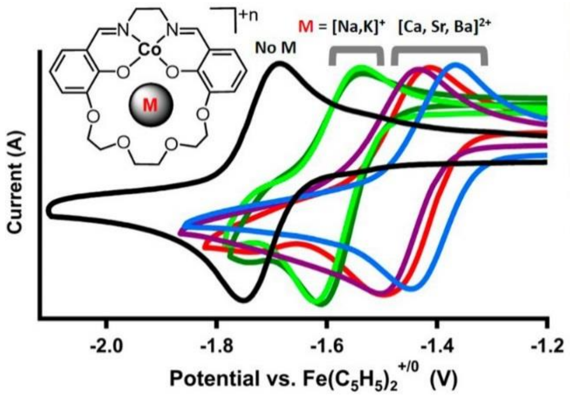

Figure 1.12: The effects of Lewis cation on Co(II/I) redox couples of Co(salen−OMe) complex. Figure taken from Ref. 59

1.15The strategy adapt in this research

Metalloenzymes such as nitrogenase consist of two parts: Fe and MoFe proteins. From the Fe protein electrons are transferred during catalysis process to MoFe protein site for conversion of N_2 to NH_3.[60]

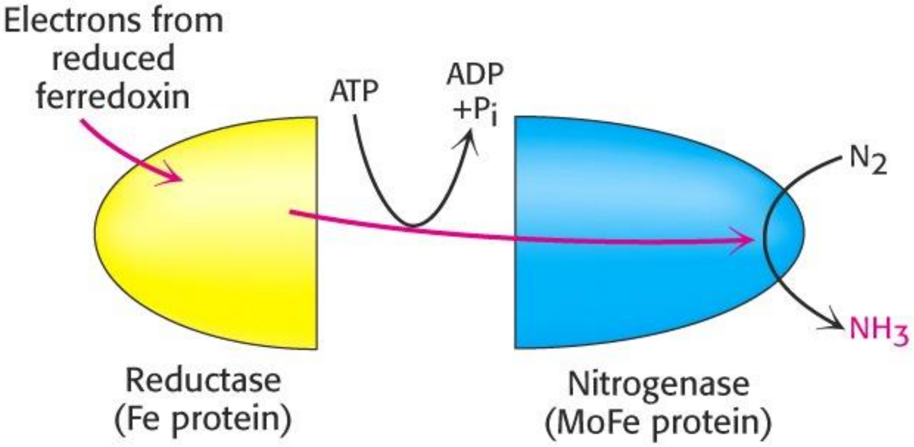

Figure 1.13: The two-component proteins of nitroganese metalloenzyme for conversion of N_2 to NH_3. Figure taken Ref. 60

I propose the use of redox-active metal complexes has been study the effects of redox-active ligand tethered near the electrocatalytic active site for electrochemical reduction of CO_2 to enhance the electrocatalytic abilities.

In Chapter 2, ligand-coordinated redox-active metal complex $\{Ru(bpy)_2\}^{2+}$ (bpy: bipyridine) tethered to an electrocatalysts is discussed. The presence of $\{Ru(bpy)_2\}^{2+}$ increased TOF while lowering η via inductive effects.

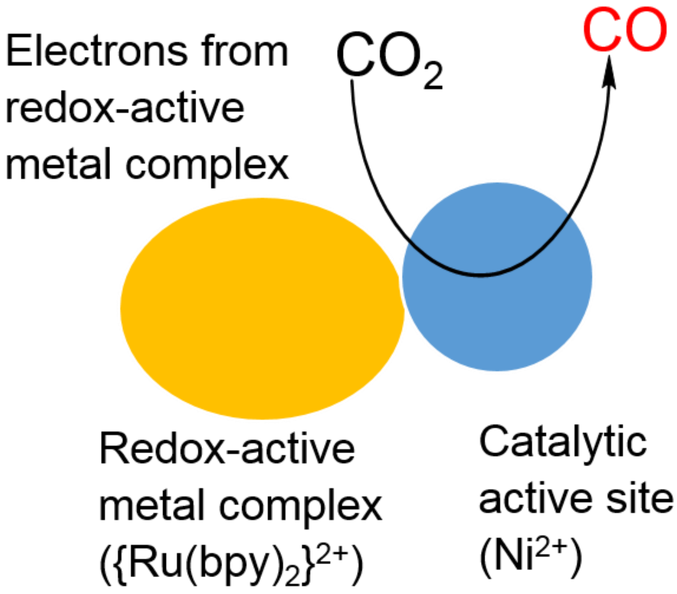

Figure 1.14: Diagram of electrocatalysts discussed in Chapter 2.

In Chapter 3, the main focus is improving electrocatalytic abilities of modified macrocyclic metal complex. The catalytic active site and ligand-coordinated redox-active metal complexes were connected via 4-pyridylmethyl groups. From a comparison of the abilities modified electrocatalysts with those of benzyl-substituted cyclen−Ni(II), it is clear that ligand-coordinated redox-active metal complex dramatically improves electrocatalytic of abilities of the cyclen−Ni(II) active site.

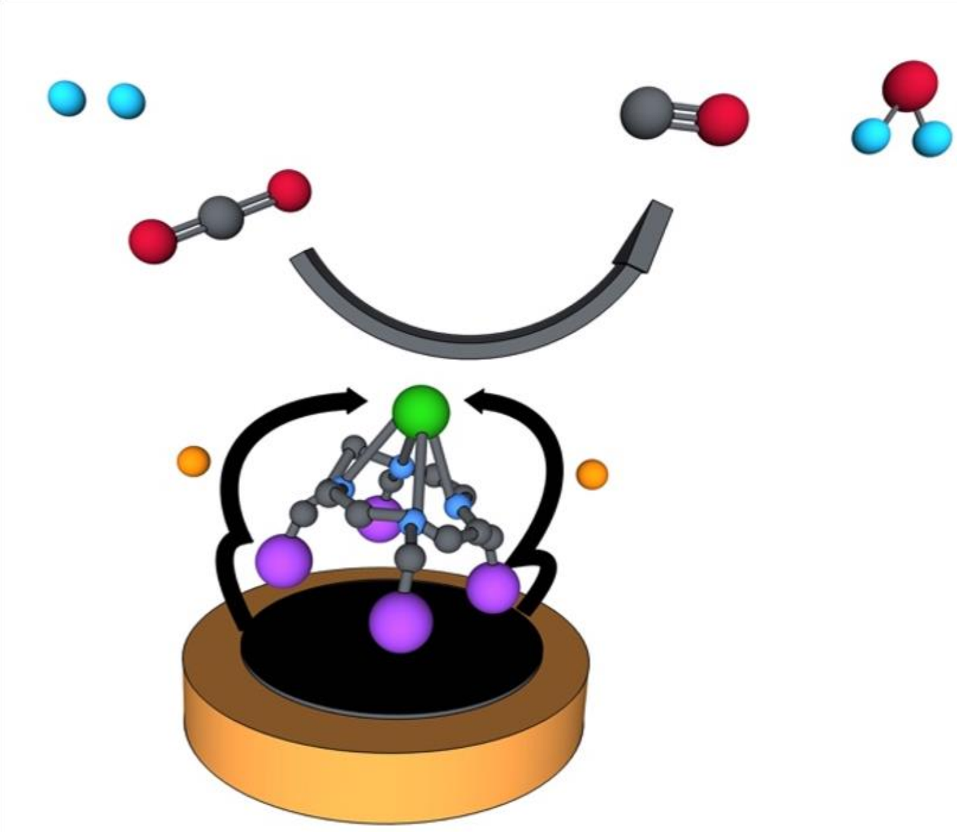

Figure 1.15: Electrocatalyst design with ligand-coordinated redox-active metal complex and electrocatalytic reduction of CO_2. Illustration of the electrocatalytic reduction of CO_2 at low overpotential. Here, first reduce the redox-active ligand coordinated metal complex moieties (purple spheres), and then the electrons (orange spheres) transfer to the Ni active center (green sphere) to reduce CO_2 to CO. Red spheres represent oxygen, gray spheres represent C atoms, and light blue atoms represent H atoms.

1.8 References

1. P. M. Votiousek, H. A. Mooney, J. Lubchenco and J. M. Melillo, *Science*, 1997, **277**, 494−499.
2. W. H. Wang, Y. Hemeda, J. T. Muckerman and G. F. Manbeck, *Chem. Rev.*, 2015, **115**, 12936−12973.
3. BP Statistical Review of World Energy, January 2013,
4. S. Chu and A. Majumdar, *Nature*, 2012, **488**, 294−303.
5. National Oceanic and Atmospheric Administration (NOAA), National Centers for Environmental Information, Global Climate Change Indicators, http://www.ncdc.noaa.gov/ monitoring-reference/ faq/indicators. php
6. National Oceanic and Atmospheric Administration (NOAA), Earth System Research Laboratory, Global Monitoring Division. http://www.esrl.noaa.gov/ gmd/ ccgg/trends/gr.html
7. J, A Cracknell, K. A. Vincent and F. A. Armstrong, *Chem. Rev.*, 2008, **108**, 2439−2461.
8. E. E. Benson, C. P. Kubiak, A. J. Sathrum and M. J. Smieja, *Chem. Soc. Rev.*, 2009, **38**, 89−99.
9. N. Yang, S. R. Waldvogel and X. Jiang, *ACS Appl. Mater. Interfaces*, 2016, **8**. 28357−28371.
10. A. Gennaro, A. A. Isse, M-G. Severin E. Vianello, I. Bhugun and J. M. Saveant, *J. Chem. Soc., Faraday Trans.*, 1996, **92**, 3963−3968.
11. D. T. Whipple and P. J. A. Kenis, *J. Phys. Chem. Lett.*, 2010, **1**, 3451−3458.
12. J. A. Bird and L. R. Faulkner, Electrochemical methods: Fundamentals and Applications, 2nd ed., John wiley & sons, Inc., Hoboken, NJ, 2001.

13. R. Francke and R. D. Little, *Chem. Soc. Rev.*, 2014, **43**, 2492−2521.
14. J. Jorissen and B. Speiser, Preparative Electrolysis on the Laboratory Scale. In *Organic Electrochemistry,* 5th ed., O. Hammerich, B. Speiser, Eds, CRC Press, Boca Raton, 2016, pp 263−330.
15. D. M. D'Alessandro, B. Smit and J. R. Long, *Angew. Chem., Int. Ed*. 2010, **49**, 6058−6082.
16. R. Steudel, *Chemie der Nichtmetalle, 2. Auflage*; de Gruyter: Berlin, 1998.
17. T. M. Klapotke, I. C. Tornieporth and I. C. T. Oetting, *Nichtmetallchemie*; Wiley VCH: Weinheim, 1994.
18. R. Francke, B. Schille and M. Roemelt, *Chem. Rev*., 2018, **118**, 4631−4701.
19. A. M. Appel, J. E. Bercaw, A. B. Bocarsly, H. Dobbek, D. L. DuBois, M. Dupuis, J. G. Ferry, E. Fujita, R. Hille, P. J. A. Kenis, C. A. Kerfeld, R. H. Morris, C. H. F. Peden, A. R. Portis, S. W. Ragsdale, T. B. Rauchfuss, J. N. H. Reek, L. C. Seefeldt, R. K. Thauer and G. L. Waldrop, *Chem. Rev.*, 2013, **113**, 6621−6658.
20. G. L. Gutsev, R. J. Bartlett and R. N. Compton, *J. Chem. Phy*., 1998, **108**, 6756−6762.
21. L. S. Wang, J. E. Reutt, Y. T. Lee and D. A. Shirley, *J. Electron Spectrosc. Relat. Phenom*., 1988, **47**, 167−186.
22. A. D. Walsh, *J. Chem. Soc*., 1953, 2266−2288.
23. J. Qiao, Y. Liu, F. Hong and J. Zhang, *Chem. Soc. Rev*., 2014, **43**, 631−675.
24. W. K. Frese, P. B. Sullivan, K. Krist and H. E. Guard, *Eds. Elsevier*, New York, 1993, Chapter 6.
25. J. Mascetti and M. Aresta, In *Carbon Dioxide as Chemical Feedstock*; Ed. Wiley-VCH: Weinheim, 2010, 55−88.
26. J. C. Calabrese, T. Herskovitz and J. B. Kinney, *J. Am. Chem. Soc*., 1983, **105**, 5914−5915.

27. M. Aresta, C. F. Nobile, V. G. Albano, E. Forni and M. Manassero, *J. Chem. Soc., Chem. Commun*., 1975, **0**, 636−637.
28. S. Sakaki, *J. Am. Chem. Soc.*, 1990, **112**, 7813−7814.
29. S. Sakaki, N. Koga and K. Morokuma, *Inorg. Chem*., 1990, **29**, 3110−3116.
30. A. Dedieu and F. Ingold, *Angew. Chem. Int. Ed. Engl*., 1989, **28**, 1694−1695.
31. J. Scneider, H. Jia, J. T. Muckerman and E. Fujita, *Chem. Soc. Rev*., 2012, **41**, 2036−2051.
32. J. D. Froehlich and C. P. Kubiak, *Inorg. Chem*., 2012, **51**, 3932−3934.
33. J. D. Froehlich and C. P. Kubiak, *J. Am. Chem. Soc*., 2015, **137**, 3565−3573.
34. J. Song, E. L. Klein, F. Neese and S. Ye, *Inorg. Chem*., 2014, **53**, 7500−7507.
35. I. Castro-Rodriguez, H. Nakai, L. N. Zakharov, A. L. Rheingold and K. Meyer, *Science*, 2004, **305**, 1757−1759.
36. V. S. Thoi, H. I. Karuadasa, Y. Surendranath, J. R. long and C. J. Chang, *J. Energy Environ. Sci.*, 2012, **5**, 7762−7770.
37. C. C. L. McCrory, C. Uyeda and J. C. Peters, *J. Am. Chem. Soc*., 2012, **134**, 3164−3170.
38. C. Costentin and J. M. Saveant, *ChemElectroChem*, 2014, **1**, 1226−1236.
39. C. Costentin, S. Drouet, M. Robert and J. M. Saveant, *J. Am. Chem. Soc*., 2012, **134**, 11235−11242.
40. J. M. Saveant, *Chem. Rev*., 2008, **108**, 2348−2378.
41. E. S. Rountree, B. D. McCarthy, T. T. Eisenhart and J. L. Dempsey, *Inorg. Chem*., 2014, **53**, 9983−10002.
42. W. Nie and C. C. L. McCrory, *Chem. Commun*., 2018, **54**, 1579−1582.
43. C. Costentin, S. Drouet, M. Robert and J. M. Saveant, *Science*, 2012, **338**, 90−94.
44. C. Costentin, M. Robert and J. M. Saveant, *Chem. Soc. Rev*., 2013, **42**, 2423−2436.

45. M. D. Samson and C. P. Kubiak, *J. Am. Chem. Soc*., 2016, **138**, 1386–1393.

46. C. Cometto, L. Chen, P. K. Lo, Z. Guo, K. C. Lau, E. A. Mallart, A. Fave, T C. Lau and M. Robert, *ACS Catal.*, 2018, **8**, 3411–3417.

47. C. Costentin and J. M. Saveant, *Nature Reviews Chemistry*, 2017, **1**, 1–8.

48. B. Fisher and R. Eisenberg, *J. Am. Chem. Soc*., 1980, **102**, 7361–7363.

49. M. Hammouche, D. Lexa, M. Momenteau and J. M. Saveant, *J. Am. Chem. Soc*., 1991, **113**, 8455–8466.

50. I. Bhugun, D. Lexa and J. M. Saveant, *J. AM. Chem. Soc*., 1996, **118**, 1769–1776.

51. J. M. Smieja, M. D. Sampson, K. A. Grice, E. E. Benson, J. D. Froehlich and C. P. Kubiak, *Inorg. Chem*., 2013, **52**, 2484–2491.

52. M. D. Sampson, A. D. Nguyen, K. A. Grice, C. E. Moore, A. L. Rheingold and C. P. Kubiak, *J. Am. Chem. Soc.*, 2014, **136**, 5460–5471.

53. F. Franco, C. Cometto, L. Nencini, C. Barolo, F. Sordello, C. Minero, J. Fiedler, M. Robert, R. Gobetto and C. Nervi, *Chem. Eur. J*. 2017, **23**, 4782–4793.

54. F. Franco, C. Cometto, F. F. Vallana, F. Ssordello, E. Priola, C. Minero, C. Nervi and R. Gobetto, Chem. Commun., 2014, 50, 14670–14673.

55. J. Agarwal, T. W. Shaw, H. F. Schaefer and A. B. Bocarsly, Inorg. Chem., 2015, 54, 5285–5294.

56. D. C. Lacy, C. C. L. McCrory and J. C. Peters, *Inorg. Chem*., 2014, **53**, 4980–4988.

57. M. Beley, J. P. Collin, R. Ruppert and J. P. Sauvage, *J. Am. Chem. Soc*. 1986, **108**, 7461–7467.

58. I. Azcarate, C. Costentin, M. Robert and J. M. Saveant, *J. Am. Chem. Soc*., 2016, **138**, 16639–16644.

59. A. H. Reath, J. W. Ziller, C. Tsay, A. J. Ryan and J. Y. Yang, *Inorg. Chem*., 2017, **56**, 3713–3718.

60. B. K. Burgess and D. J. Lowe, Chem. Rev., 1996, 96, 2983–3011.

Chapter 2

Tuning the electrocatalytic abilities of metal complex with a pseudo-pincer ligand functionalized with a redox-active metal complex

2.1 Introduction

Carbon dioxide (CO_2) is an abundant source of carbon atoms obtained from the burning fossil fuels for energy production. However, reserves of fossil fuels are becoming depleted. The use of fossil fuels has led to an increase in atmospheric CO_2, which has played a role in change climate as primary greenhouse gas. Utilization of CO_2 via electrochemical conversion is a promising approach toward the production of value added chemicals and fuels. Electrocatalytic CO_2 reduction to a value added chemicals is one of the way to utilized atmospheric CO_2. However, the electrocatalytic CO_2 reduction process suffers from poor selectivity and low efficiency. Therefore, it is a major challenge to develop selective and highly efficient electrocatalysts that operate at low overpotential.[1–5] Researchers have applied several methods to overcome this problem. In the 90's , Saveant and co-workers utilized Mg^{2+} cations as a Lewis acid with electrocatalysts to improved CO_2 reduction rate.[6] However, Kubiak and co-workers have utilized Mg^{2+} cations to increase the CO_2 reduction rate and decrease the overpotential.[7] The overall CO_2 reduction reaction in the presence of Mg^{2+} ion is

$$2\ CO_2 + Mg^{2+} + 2e = CO + MgCO_3$$

CO_2 reduction leads disproportionation to afford CO and $MgCO_3$. Although Mg^{2+} cations increase the CO_2 reduction rate, the selectivity for the reduction products are reduced, and $MgCO_3$ is insoluble in electrolysis solution to hamper further catalytic process. To avoid this problem, using acid as a proton source is one of the best ways, to increase the rate and selectivity. Proton-coupled electron transfer accelerates CO_2 reduction.[8–10] Weak acids, such as water, methanol, 2,2,2-triflouroethanol and phenol have been utilized as proton sources. The overall reaction of CO_2 reduction in the presence of protons is

$$CO_2 + 2H^+ + 2e = CO + H_2O$$

In the presence of a proton source, the active metal species binds CO_2, and then a proton adds to from M-COOH adduct, which promotes faster C–O bond breaking and theselective formation CO. Ligand design is very important for improving catalytic abilities. [11–16] Redox-active ligands are very popular for electrocatalysts because they can store electrons in their structure to activate CO_2 on metal centres. In addition, redox-active metal complex functionalized electrocatalysts are able to reduce CO_2 to CO selectively in the presence of proton sources.[17–26] Pincer-type ligands metal complexes have been studied as electrocatalysts for CO_2 reduction, it has been shown good catalytic reduction ability,[27–29] although, most pincer-type electrocatalysts have been used for CO_2 hydrogenation at high temperatures and pressures.[30] Penta-coordinate pincer ligands for nickel complexes have been studied for CO_2 reduction, [31–32] because penta-coordinate nickel complex has a vacant site for CO_2 activation on the metal centre. However, pincer-type electrocatalysts suffer from low selectivities and high overpotential.

In this works, the catalytic activity of a penta-coordinated electrocatalyst were improved by utilizing a redox-active ligand coordinated metal complex instead of using an acid. Previously a μ_3-oxo-triruthenium cluster tethered to an electrocatalysts was used. The triruthenium cluster can provide one electron to the catalytic active centre at a lower overpotential.[33] In my research, a ruthenium polypyridine complex, $\{Ru(bpy)_2\}^{2+}$ (bpy = 2,2'-bipyridine) was used, it has rich redox properties and donate up to four electrons on catalytic process.[34,35] Although cation such as Ca^{2+}, Ba^{2+}, Na^+ and K^+ could be tuning redox potential of analogous redox-active sites by an inductive effect due to the cationic charge,[36] a redox-active ligand coordinated metal complex is more useful than cations in solution because its redox-activity increases the electron density near the to enhance the activation of CO_2 and lower the overpotential. To utilize redox-active metal complex with catalytic active site a ditopic planar pseudo-pincer ligand, quinolone-2-carbaldehyde (pyridine-2-carbonyl) hydrazone (qlca) was selected. The qlca ligand has two donor sites allowing it to bridge $\{Ru(bpy)_2\}^{2+}$ and electrocatalytic active site. The $\{Ru(bpy)_2\}^{2+}$ is coordinated by the qlca through the amide O atom and imine N atom to afford $[(bpy)_2Ru^{II}(\mu\text{-qlca})]Cl$ and a Ni^{II} ion as the electrocatalytic active site to afford $[(bpy)_2Ru^{II}(\mu\text{-qlca})Ni^{II}Cl_2]Cl\cdot 4H_2O\cdot CH_3OH$. To understand the effect of redox-active metal complex, $[Ni(qlca)Cl_2]^-$ was prepared and studied.

2.2 Result and Discussion

The bridging ligand qlca was prepared following a previously reported procedure.[37,38] $[Ni(qlca)Cl_2]^-$ was obtained from the reaction of $NiCl_2 \cdot 6H_2O$ and qlca in ethanol in the presence of trimethylamine. $[(bpy)_2Ru^{II}(\mu\text{-qlca})]Cl$ was synthesized by mixing *cis*-$[Ru(bpy)_2Cl_2]$ and qlca in ethanolic solution. $[\{(bpy)_2Ru^{II}\}(\mu\text{-qlca})Ni^{II}Cl_2]Cl \cdot 4H_2O \cdot CH_3OH$ was obtained by reacting $NiCl_2 \cdot 6H_2O$ and $[\{(bpy)_2Ru^{II}\}(\mu\text{-qlca})]Cl$ in ethanolic solution. Deep-red plate-like single crystals of $[\{(bpy)_2Ru^{II}\}(\mu\text{-qlca})Ni^{II}Cl_2]Cl \cdot 4H_2O \cdot CH_3OH$ were obtained after 3–4 days.

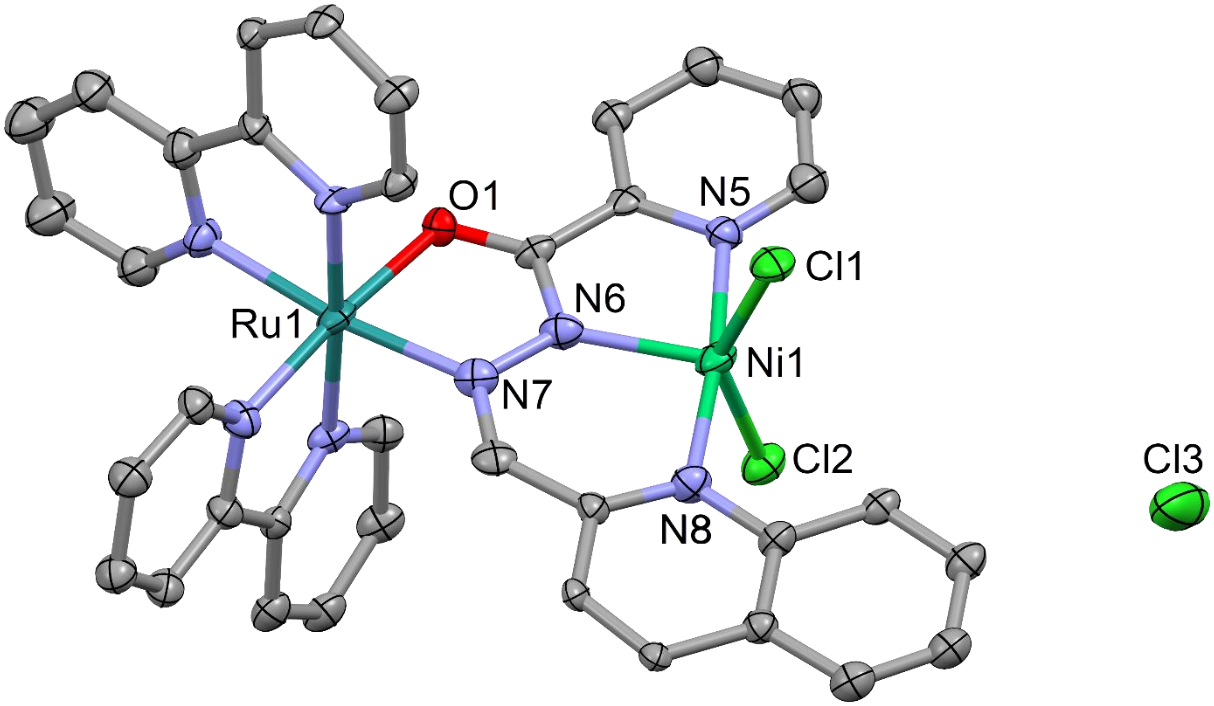

Figure 2.1: ORTEP diagram of $[\{(bpy)_2Ru^{II}\}(\mu\text{-qlca})Ni^{II}Cl_2]Cl$ at 50% probability. Hydrogen atoms and solvent molecule are omitted for clarity.

An ORTEP diagram of [{(bpy)$_2$Ru^{II}}(μ-qlca)Ni^{II}Cl$_2$]Cl·4H$_2$O·CH$_3$OH is shown in Figure 2.1, and the crystal data are summarized in Table 2.3. [{(bpy)$_2$Ru^{II}}(μ-qlca)Ni^{II}Cl$_2$]Cl·4H$_2$O·CH$_3$OH crystallized in the monoclinic space group $P2_1$. The asymmetric unit is composed of two bpy ligands coordinated to a Ru^{II} ion, one Ni^{II} ion coordinated by two Cl$^-$ ions, one qlca ligand bridging the Ru^{II} and Ni^{II} ions and a Cl$^-$ ion as a counter ion. Similar to the structure reported by A. Mori *et al*, the hydrazone group of the qlca ligand is deprotonated.[37] Atoms N8, N6 and N5 of the qlca ligand coordinate to the Ni^{II} ion in a tridentate mode. The Ru^{II} ion in the {Ru(bpy)$_2$}$^{2+}$ moiety adopts octahedral geometry and is coordinated by atoms N7 and O1 of qlca in a bidentate mode. The O1–C26, C26–N6 and N6–N7, N7–C27 bond lengths were determined to be 1.28(3), 1.36(3), 1.38(3), and 1.31(3) Å, respectively, suggesting that the negative charge of the ligand is delocalized in this region.[37,38] In ESI mass spectra (Figure 2.15), the molecular ion peak was observed at 817 *m*/*z*, which corresponds to the [{(bpy)$_2$Ru^{II}}(μ-qlca)Ni^{II}Cl$_2$]$^+$ unit. There are methanol and four water molecules per asymmetric unit at 93 K. Elemental analysis of desolvated [{(bpy)$_2$Ru^{II}}(μ-qlca)Ni^{II}Cl$_2$]Cl·4H$_2$O·CH$_3$OH agrees with the calculated value for [(bpy)$_2$Ru(μ-qlca)NiCl$_2$]Cl.

An ORTEP diagram of [{(bpy)$_2$Ru}(μ-qlca)]Cl is shown in Figure 2.13 , and the crystal data are summarized in Table 2.2. [Ni(qlca)Cl$_2$]$^-$ was characterization by ESI-Mass shown in (Figure 2.14)

Table 2.1

Selected bond distance (Å) and angles (deg) for $[\{(bpy)_2Ru^{II}\}(\mu\text{-qlca})Ni^{II}Cl_2]Cl$

Bond distance	Bond angles
Ni1–N5 = 2.073(2)	Cl1–Ni1–Cl2 = 147.1(2)
Ni1–N6 = 2.012(2)	N5–Ni1–Cl1 = 89.1(5)
Ni1–N8 = 2.078(2)	N5–Ni1–Cl2 = 92.0(5)
Ni1–Cl1 = 2.362(6)	N5–Ni1–N6 = 80.5(6)
Ni1–Cl2 = 2.333(6)	N5–Ni1–N8 = 174.0(6)
N6–N7 = 1.39(2)	N1–Ru1–N7 = 172.6(6)
Ru1–N7 = 2.04(2)	O1–Ru1–N7 = 79.3(3)
Ru1–O1 = 2.07(1)	
Ru1–N1 = 2.11(2)	
Ru1–N2 = 2.09(1)	
Ru1–N3 = 2.09(2)	
Ru1–N4 = 2.03(2)	
C26–O1 = 1.28(2)	

2.3 Electrochemical Studies

Cyclic voltammetry (CV) is the most commonly employed electroanalytical method for studying molecular electrocatalysts. Electrochemical properties of $[Ni(qlca)Cl_2]^-$ and $[\{(bpy)_2Ru\}(\mu\text{-qlca})NiCl_2]Cl$ were investigated by using CV (details in experimental section). The cyclic voltammograms of $[Ni(qlca)Cl_2]^-$ were acquired in 5% H_2O and CH_3CN (v/v) solutions of 0.1 M tetrabutylammonium hexafluorophosphate ($TBAPF_6$) saturated with N_2 and CO_2 and shown in Figure 2. The broad waves at −0.40 V and −0.72 V vs. NHE were assigned to due to qlca ligand based. The waves at −1.30 V and −1.61 V vs. NHE were assigned Ni(II/I) and Ni(I/0) couples, respectively. Under CO_2, the catalytic current increased and shifted positively and the anodic waves disappeared, indicating that was reduced CO_2. However, the enhancement small, indicating poor electrocatalysis.

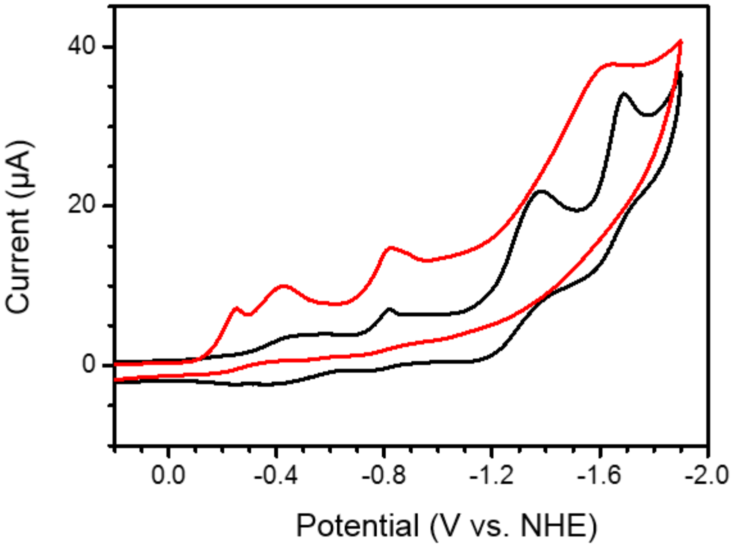

Figure 2.2: Cyclic voltammograms of $[Ni(qlca)Cl_2]^-$ (0.5 mM) in 5% H_2O and CH_3CN solution mixture contains 0.1 M $TBAPF_6$ under N_2 (black) and CO_2 saturated (red). The scan rate was 0.1 V/s. A glassy carbon electrode was used as the working electrode.

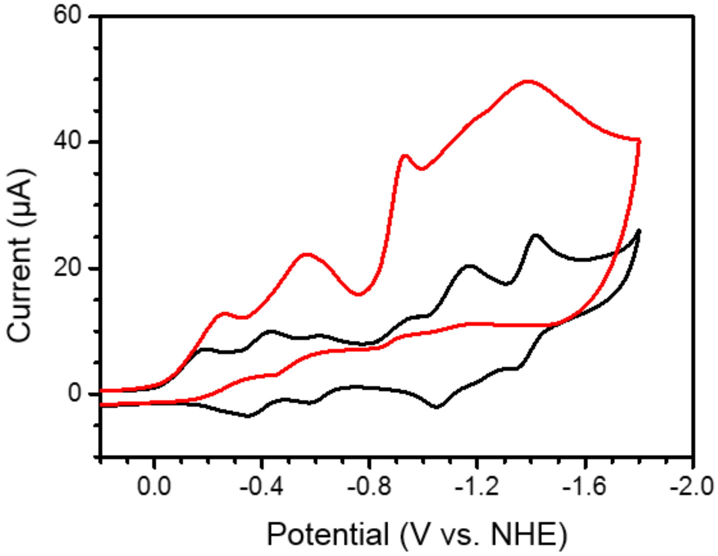

Figure 2.3: Cyclic voltammograms of [{(bpy)$_2$Ru}(µ-qlca)NiCl$_2$]Cl (0.5 mM) in dry CH$_3$CN containing 0.1 M TBAPF$_6$ under N$_2$ (black) and CO$_2$ saturated (red). The scan rate was 0.1 V/s. A glassy carbon electrode was used as the working electrode.

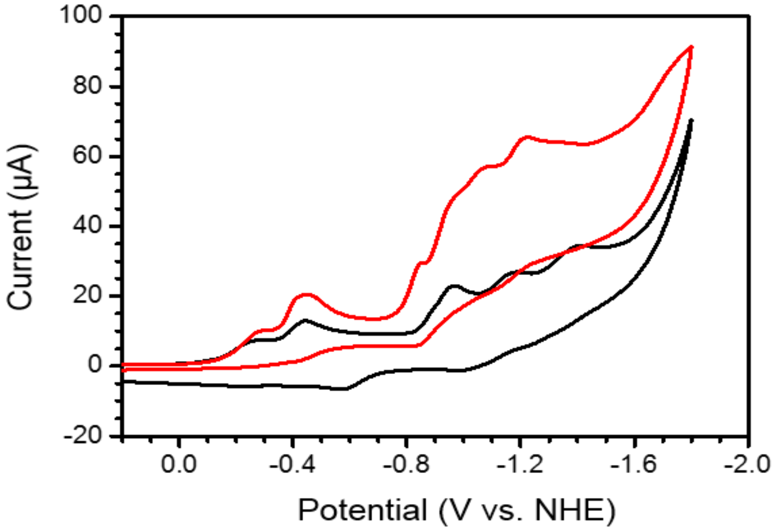

Figure 2.4: Cyclic voltammograms of [{(bpy)$_2$Ru}(µ-qlca)NiCl$_2$]Cl (0.5 mM) in 5% H$_2$O and CH$_3$CN contains 0.1 M TBAPF$_6$ under N$_2$ (black) and CO$_2$ saturated (red). The scan rate was 0.1 V/s. A glassy carbon electrode was used as the working electrode.

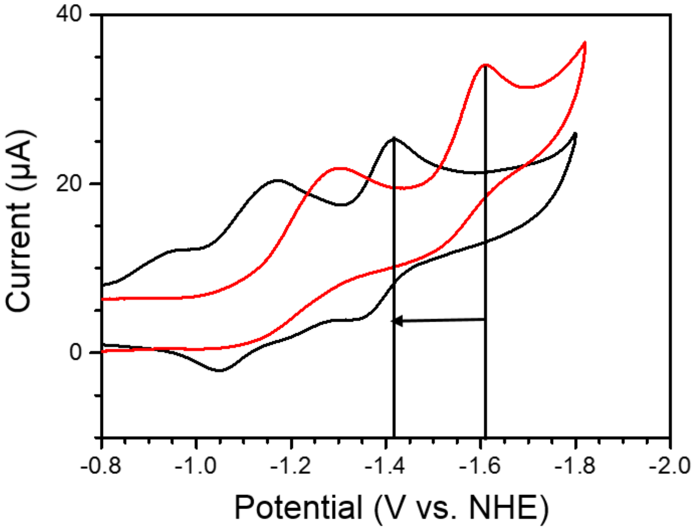

Figure 2.5: Comparison of the cyclic voltammograms (normalized) of [{(bpy)$_2$Ru}(μ-qlca)NiCl$_2$]Cl (black) and [Ni(qlca)Cl$_2$]$^-$ (red) in 5% H_2O and CH_3CN containig 0.1 M TBAPF$_6$ under N_2. The scan rate was 0.1 V/s. A glassy carbon electrode was used as the working electrode.

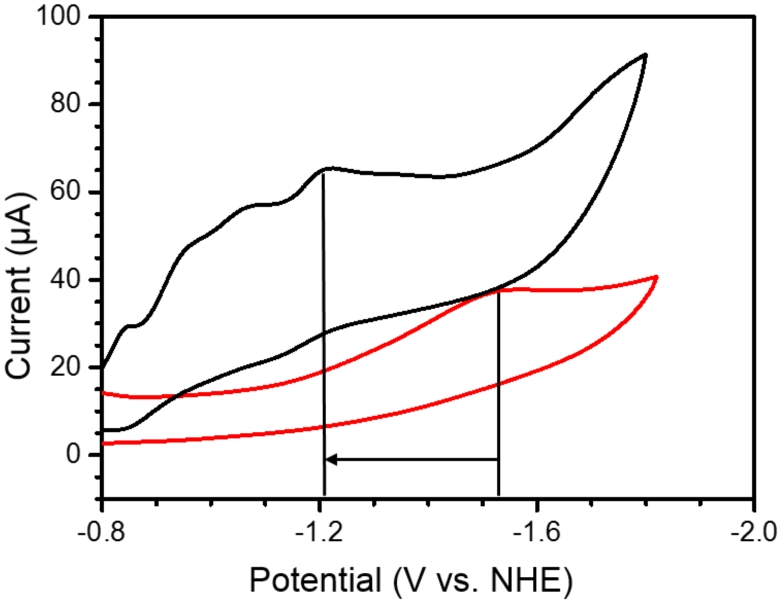

Figure 2.6: Comparison of the cyclic voltammograms (normalized) of [{(bpy)$_2$Ru}(μ-qlca)NiCl$_2$]Cl (black) and [Ni(qlca)Cl$_2$]$^-$ (red) in 5% H_2O and CH_3CN containing 0.1 M TBAPF$_6$ under CO_2. The scan rate was 0.1 V/s. A glassy carbon electrode was used as the working electrode.

CV was performed on [{(bpy)$_2$Ru}(μ-qlca)NiCl$_2$]Cl first in dry CH$_3$CN solution as shown in Figure 2.3. Waves at −0.18 (under CO$_2$ same wave appeared for [Ni(qlca)Cl$_2$]$^-$) and −0.62 V vs. NHE were assigned to the first and second reductions of ligand qlca. The waves at –0.45 V vs. NHE was assigned to first reduction of bpy and that at −0.95 V vs. NHE was assigned to the second bpy reduction. The waves at −1.20 V and −1.42 V vs. NHE were assigned to Ni(II/I) and Ni(I/0) couples, respectively. The waves for Ni(II/I) and Ni(I/0) couples were at less negative potentials than those for[Ni(qlca)Cl$_2$]$^-$ (Figure 2.2) because of an inductive effect from the Ru^{2+} centre. A similar behaviour has been observed when Ca^{2+} or Na$^+$ were added to the cell.[36] The current was enhanced, indicating the reduction of CO$_2$, and the enhancement was much higher than that for [Ni(qlca)Cl$_2$]$^-$, indicating electronic influence of {Ru(bpy)$_2$}$^{2+}$ unit on the electrocatalytic centre. In dry CH$_3$CN, disproportionation of CO$_2$ to CO and CO$_3^{2-}$ occurs due to the absence of a proton source.[39] The reduction process of CO$_2$ change due to the presence of proton. It is thought that, during electrolysis, a carboxylic intermediate forms in the presence of proton, and promote faster C−O bond cleavage to improve catalytic process.[40] When CV was performed on [{(bpy)$_2$Ru}(μ-qlca)NiCl$_2$]Cl in a 5% H$_2$O and CH$_3$CN (v/v) solution mixture and found that the reduction wave for Ni(II/I) decreased at −1.17 V and Ni(I/0) at −1.40 V vs. NHE. Here, H$_2$O is used for proton source. Under CO$_2$, in 5% H$_2$O and CH$_3$CN (v/v) solution mixture, the catalytic current was greater and shifted positively, indicating an electrocatalytic process. From a comparison of the cyclic voltammograms of [Ni(qlca)Cl$_2$]$^-$ and [(bpy)$_2$Ru(μ-qlca)NiCl$_2$]Cl, there is a distinct benefit having the redox-active ligand coordinated metal complex. The redox-active ligand increases electron density on catalytic active site, helping to enhance the catalytic current. At the same time, the Ru^{2+} centre causes the electrocatalytic potential shifted positively due to inductive effects.[36] In other words, attaching a cation to the active site has a bigger inductive effect than free ions in solution do. (Figure 2.17).

2.4 Control potential electrolysis (CPE) experiments

Control potential electrolysis (CPE) experiments were performed to confirm the catalytic abilities of [(bpy)$_2$Ru(μ-qlca)NiCl$_2$]Cl and [Ni(qlca)Cl$_2$]$^-$ towards electrocatalytic CO$_2$ reduction. The CPE experiments using [(bpy)$_2$Ru(μ-qlca)NiCl$_2$]Cl were performed with and without water, which acts as a proton source. The CPE using [Ni(qlca)Cl$_2$]$^-$ was performed in wet CH$_3$CN. The CPE experiments using [{(bpy)$_2$Ru}(μ-qlca)NiCl$_2$]Cl and [Ni(qlca)Cl$_2$]$^-$ were performed for 30 min to compare their electrocatalytic abilities. A blank CPE experiment was performed with at −1.6 V vs. NHE to confirm electrolysis occurs only with electrocatalysts and no activity was observed using the blank solution. The CPE experiments was performed using [{(bpy)$_2$Ru}(μ-qlca)NiCl$_2$]Cl at −1.40 V vs. NHE (based on peak current from CV data under CO$_2$ atmosphere) for 30 min in dry CH$_3$CN solution containing 0.1 M TBAPF$_6$. Headspace samples were obtained by using a gas-tight syringe and analysed by using gas chromatography-mass spectroscopy (GC-MS). After 30 min of electrolysis, it was determined that gaseous product was CO. The Faradaic efficiency was 30% and the TOF value was 2.30 s^{-1} (calculation describe in experimental section). Within a few minutes of electrolysis, the solution colour changed and became cloudy, indicating disproportionation reaction of CO$_2$. The lack of a proton source causes disproportionation of CO$_2$ and decreases The Faradaic efficiency for CO.[39] Further, CPE experiments were performed using [{(bpy)$_2$Ru}(μ-qlca)NiCl$_2$]Cl in a mixture of 5% H$_2$O and CH$_3$CN containig 0.1 M TBAPF$_6$ at −1.20 V vs. NHE (based on peak current from CV data under CO$_2$ atmosphere in similar solution mixture). After 30 min of electrolysis, headspace sample showed that the only gaseous product of CO_2 reduction is CO, and it formed with a Faradaic efficiency of 82%. The water clearly quenches the disproportionation mechanism. The TOF value was 120 s^{-1} in the presence of water. The colour of the solution did not change and no precipitated formed, indicating that in the presence of water , the complex remains stable.

The CPE experiments using $[Ni(qlca)Cl_2]^-$ in 5% H_2O and CH_3CN solution mixture containg 0.1 M $TBAPF_6$ was performed at −1.55 V vs. NHE (based on peak current from CV data under CO_2 atmosphere in H_2O and CH_3CN solution mixture) to understand the effect the redox-active metal complex on catalytic process. The gaseous CO_2 reduction product was determined CO by gas chromatography. The faradaic efficiency was 60%, and the TOF was 0.83 s^{-1}. These values are much lower than those using $[\{(bpy)_2Ru\}(\mu\text{-qlca})NiCl_2]Cl$. The results show the electronic influence of the redox-active metal complex on the electrocatalytic active site. In comparison to other pincer-type ligand supported nickel complexes for CO_2 reduction electrocatalysts, $[\{(bpy)_2Ru\}(\mu\text{-qlca})NiCl_2]Cl$ has a higher TOF value. The TOF values for pincer (carbine-pyridine-carbene) pincer and (NNN) bis(ketimino) pyridine pincer-type ligand supported nickel complexes have been reported to be 90 s^{-1} and 2.9 s^{-1}, respectively.[31,32]

The overpotential is a thermodynamic parameter related to the additional energy needed to drive a reaction. The overpotential is generally defined as the diference between the applied potential for electrolysis and the standard reduction potential for CO_2/CO couple.[41] The reduction potential for CO_2/CO has been reported to be −0.72 V vs. SHE (−0.72 V vs. NHE) in wet CH_3CN.[42] The onset electrolysis potential for $[\{(bpy)_2Ru\}(\mu\text{-qlca})NiCl_2]Cl$ was −1.20 V vs. NHE. The onset overpotential for $[\{(bpy)_2Ru\}(\mu\text{-qlca})NiCl_2]Cl$ calculated to be 480 mV. The onset potential for

$[Ni(qlca)Cl_2]^-$ was −1.55 V vs. NHE and the overpotential was calculated to be 830 mV. In other words, the onset overpotential of $[\{(bpy)_2Ru\}(\mu\text{-}qlca)NiCl_2]Cl$ is 350 mV lower than $[Ni(qlca)Cl_2]^-$.

The $\{Ru(bpy)_2\}^{2+}$ moiety causes not only an increase in the TOF value but also a decrease in the overpotential. The inductive effect from the Ru^{2+} ion decreases the electrocatalytic potential for CO_2 reduction. A similar effect has been observed when trimethaylanilinium groups were added to an iron(0) tetraphenylporphyrins electrocatalysts.[43]

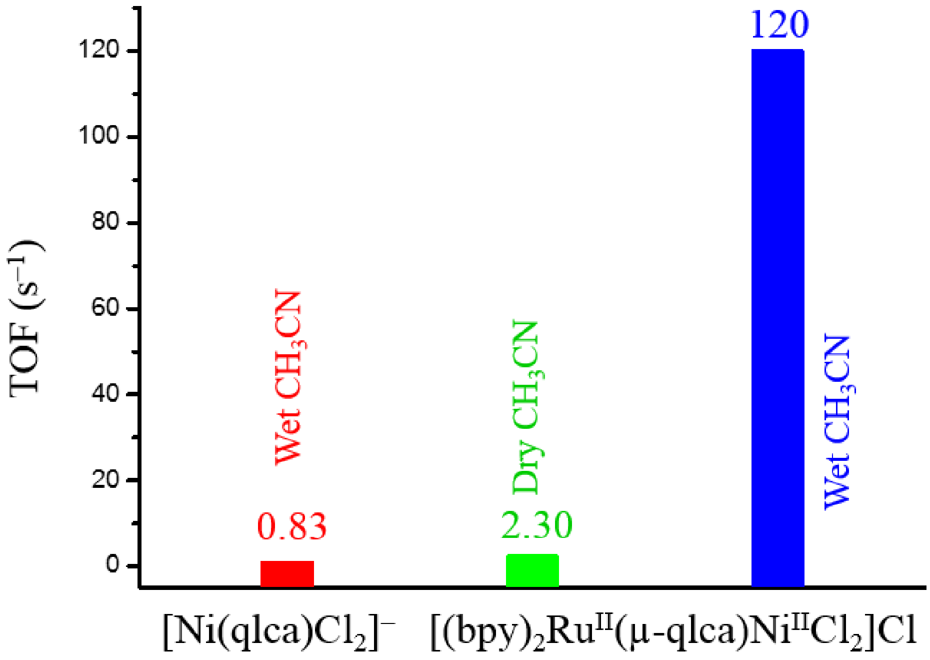

Figure 2.7: Comparison of turnover frequencies (TOF) using [{(bpy)$_2$Ru}(μ-qlca)NiCl$_2$]Cl (green: electrolysis performed in dry CH_3CN solution; blue: electrolysis performed in 5% H_2O and CH_3CN (v/v) solution) and [Ni(qlca)Cl$_2$]$^-$ (red: electrolysis performed in 5% H_2O and CH_3CN (v/v) solution). Electrocatalysts functionazed with redox-active ligand coordinated metal complexes show better performance.

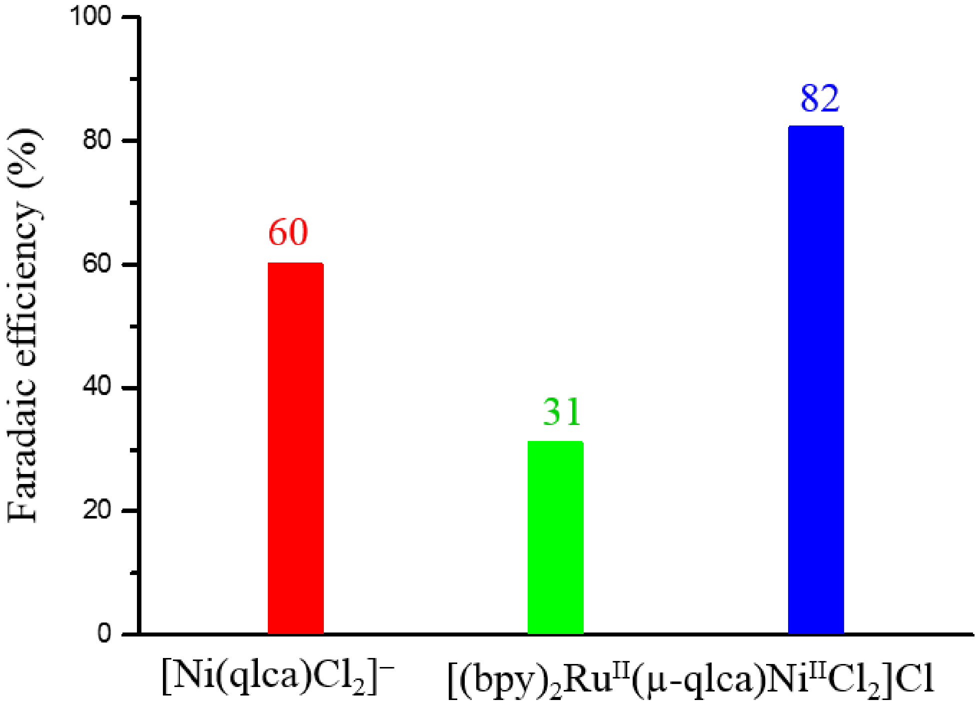

Figure 2.8: Comparison of the faradaic efficiencies (FE) using [{(bpy)$_2$Ru}(μ-qlca)NiCl$_2$]Cl (green: electrolysis performed in dry CH_3CN solution; blue: electrolysis performed in 5% H_2O and CH_3CN (v/v) solution) and [Ni(qlca)Cl$_2$]$^-$ (red: electrolysis performed in 5% H_2O and CH_3CN (v/v) solution).

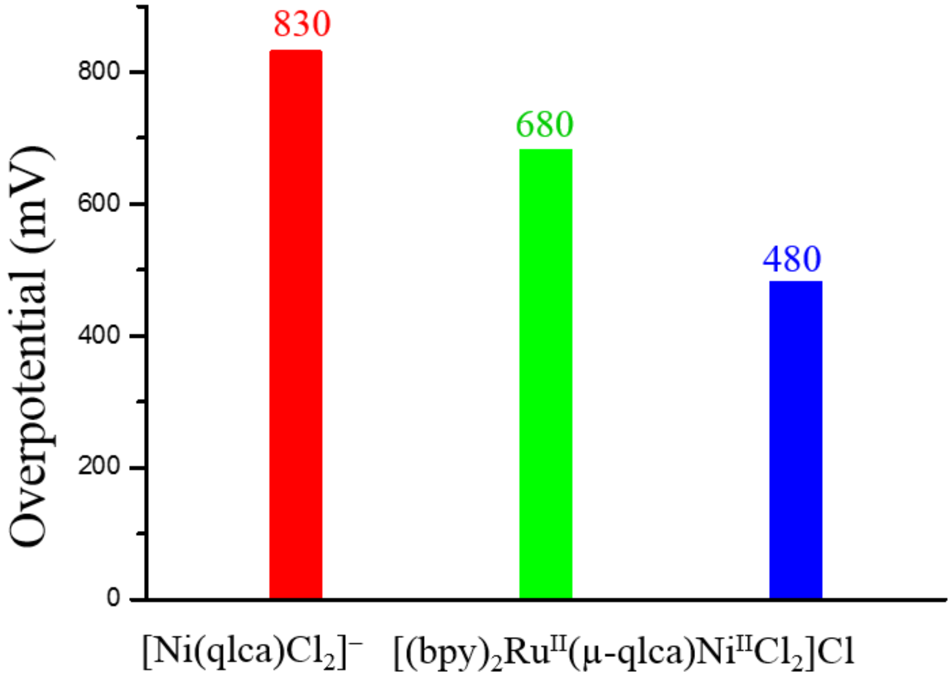

Figure 2.9. Comparison of the overpotential (η) using [{(bpy)$_2$Ru}(μ-qlca)NiCl$_2$]Cl (green: electrolysis performed in dry CH_3CN solution; blue: electrolysis performed in 5% H_2O and CH_3CN (v/v) solution) and [Ni(qlca)Cl$_2$]$^-$ (red: electrolysis performed in 5% H_2O and CH_3CN (v/v) solution). [{(bpy)$_2$Ru}(μ-qlca)NiCl$_2$]Cl operates at a lower overpotential than [Ni(qlca)Cl$_2$]$^-$ because the inductive effect of Ru^{2+} cations on catalytic active site.

2.5 Catalytic Tafel Plot

The catalytic tafel plot expresses the relationship between TOF and the overpotential (η) (=$E^{o}_{CO_2/CO} - E$); where $E^{o}_{CO_2/CO}$ is the standard reduction potential of CO_2 to CO couples and E is the applied potential on electrocatalysis process.[7,8,41,44,45] The catalytic tafel plot is important method for comparing electrocatalysts under different conditions. In other words, the conditions can be ignored when comparing electrocatalysts. A good electrocatalyst is defined to have a high

TOF at a low overpotential. The catalytic rate constant (k_{cat}), which describe the overall rate of homogeneous catalysis, can be determined form the CV data, and it is to the TOF and overpotentail.[7,41,43,47–49] The turnover frequency and catalytic rate constant are equal when the applied potential is sufficiently negative of the redox couple, where the electrocatalytic process occurs efficiently 100% active form.[46]

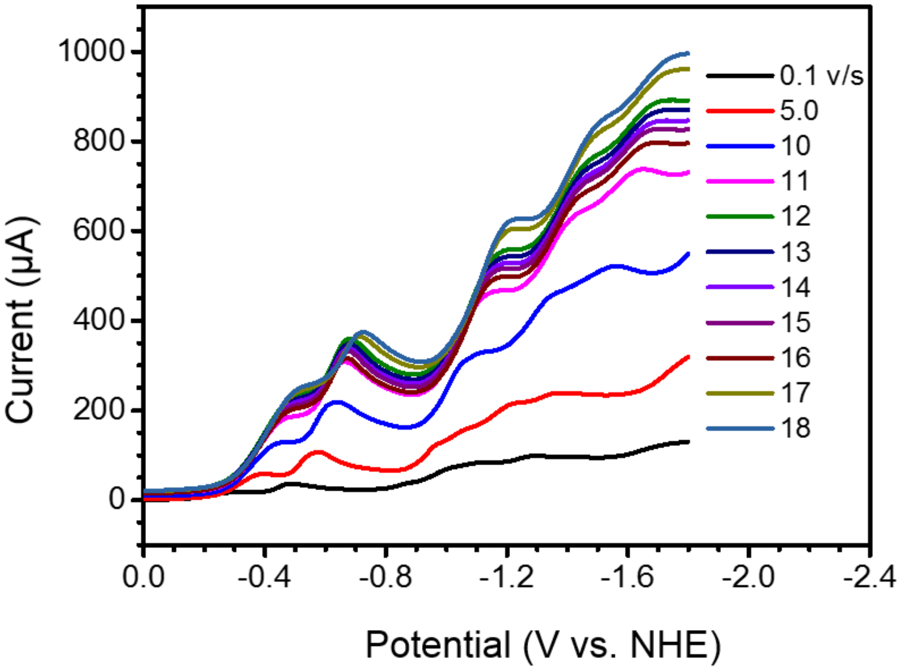

Figure 2.10. Linear sweep voltammograms (LSV) using [{(bpy)$_2$Ru}(μ-qlca)NiCl$_2$]Cl in 5% H_2O and CH_3CN (v/v) containing $TBAPF_6$ under CO_2 atmosphere using glassy carbon electrode at the following scan rates (V/s): 0.1, 5, 10, 11, 12, 13, 14, 15, 16, 17 and 18. The catalytic rate independent scan is obtain at scan rate 18 V/s, which is catalytic highest active form.

The electrocatalysts that display catalytic waves as idealized canonical ‘S-shaped’ tafel plot can be obtained as follows. At a high scan rate (18 v/s) a catalytic plateau independent scan rate, which indicates pure kinetic conditions due to correlation between the catalyst diffusion and fast catalytic rates. The k_{cat} can be obtained under such conditions by using Eq. 1

$$i_{plateau} = 2FS \times C^{o}_{cat} \times \sqrt{D_{cat}} \times \sqrt{k_{cat}} \qquad \text{……. Eq. 1}$$

where, $i_{plateau}$ is the catalytic plateau current, C^{o}_{cat} is the catalytic concentration in the solution, D_{cat} is the diffusion coefficient and k_{cat} is catalytic rate constant.

On the other hand, the one electron diffusion current of the catalysts is given by Eq. 2

$$i^{0}_{peak} = 0.446 \times \mathrm{FS} \times C^{o}_{cat} \times \sqrt{D_{cat}} \times \sqrt{Fv/RT} \quad \text{……..Eq. 2}$$

where, i^{0}_{peak} is the noncatalytic current, F is the faraday constant, v is the scan rate of noncatalytic current (0.1 v/s), R is the universal gas constant and T is the temperature. Dividing Eq. 1 by Eq. 2 allow to gives $i_{plateau}/\ i^{0}_{peak}$, from which k_{cat} can be determined independent of D_{cat} (Eq. 3

$$k_{cat} = (i_{plateau}/i^{0}_{peak})^{2} \times 1/\ (2 \times 2.24)^{2} \times Fv/RT \quad \text{………..Eq. 3}$$

From CV data, $i_{plateau} = 990$ μA and $i^{0}_{peak} = 25$ μA

Using Eq. 3, the k_{cat} value was calculated to be 305 s^{-1}. The tafel plot for $[\{(bpy)_2Ru\}(\mu\text{-}qlca)NiCl_2]Cl$ was built using Eq. 4.

$$\mathrm{TOF}_{max} = \frac{k_{cat}}{1+\exp\left[\frac{F}{RT}\left(E^{o}_{CO_2/CO} - E_{\frac{1}{2}}\right)\right] \times \exp\left(-\frac{\mathrm{F}}{\mathrm{RT}}\eta\right)} \qquad \text{….. Eq. 4}$$

In this Eq. 4, $E^{o}_{CO_2/CO}$ is −0.72 V vs. NHE,[42] $E_{1/2}$ is the half-plateau potential of −1.06 V vs. NHE. In this experiment, using overpotential 800 mV, the TOF was calculated to be 305 s^{-1}. Therefore, log TOF_{max} was 2.48 s^{-1} at 800mV overpotential and log TOF_0 was −4.28 s^{-1} at overpotential zero.

$[Ni(qlca)Cl_2]^-$ k_{cat} was calculated using Eq. 3 to be 0.31 s^{-1}. Using overpotential 1000 mV, the TOF value was 0.81 s^{-1}. Thus TOF_{max} was –0.50 s^{-1} and TOF_0 was –9.47 s^{-1}.

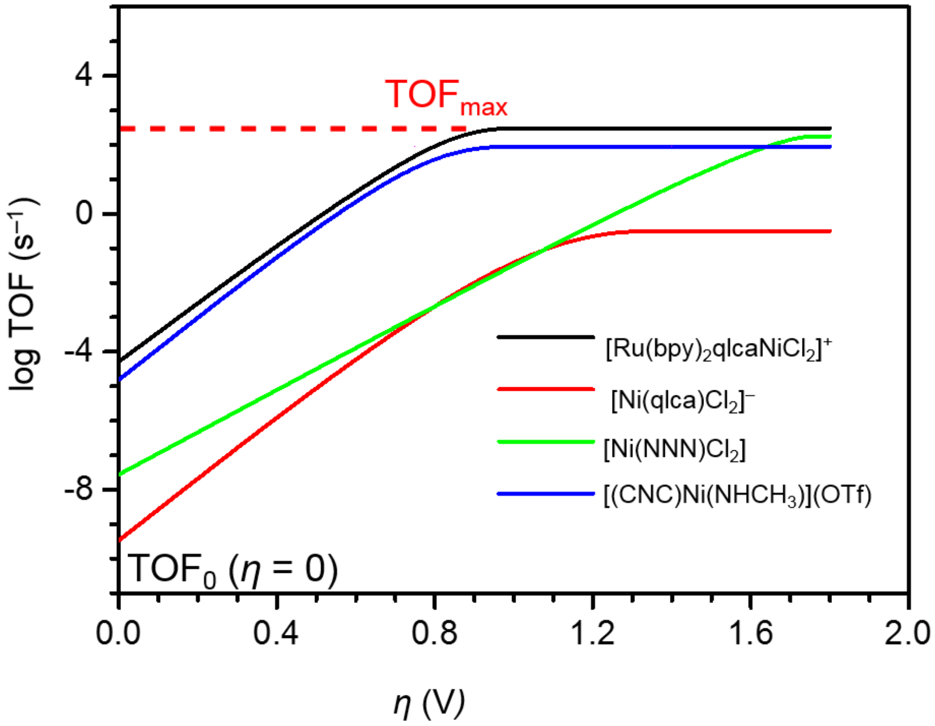

Figure 2.11. Catalytic tafel plots $[\{(bpy)_2Ru\}(\mu\text{-}qlca)NiCl_2]Cl$ with pincer type nickel based electrocatalysts ($[Ni(NNN)Cl_2]$[32] and $[(CNC)Ni(NHCH_3)](OTf)$[31]) and $[Ni(qlca)Cl_2]^-$.

From figure 11 $[\{(bpy)_2Ru\}(\mu\text{-}qlca)NiCl_2]Cl$ is better electrocatalysts than other pincer-type nickel-based electrocatalysts. $[\{(bpy)_2Ru\}(\mu\text{-}qlca)NiCl_2]Cl$ had a higher TOF_{max} at lower overpotential than other complexes. Moreover, the redox-active ligand coordinated metal complex has a dramatic effects on the electrocatalysts.

2.6 Proposed mechanism of CO_2 to CO by $[\{(bpy)_2Ru\}(\mu\text{-}qlca)NiCl_2]Cl$

In this section, a proposed mechanism for CO_2 to CO using $[\{(bpy)_2Ru\}(\mu\text{-}qlca)NiCl_2]Cl$ in the presence of H_2O as a proton source is proposed on the basis of studies involving other Ni_based electrocatalysts.[50,51] First, Ni^{II} accepts one electron affording to Ni^{I} and then bind CO_2 through carbon atom to form Ni^{I}–CO_2 adduct.[52–55] Electrocatalytic reduction of CO_2 to CO needs two electrons. Ni^{I}–CO_2 adduct accept one electron and one proton to form Ni^{I}–COOH intermediate. The final step of the reaction involves of breaking the C–O bond cleavage to generate CO, which is rate determining step.[56,57] The C–O bond breaking is facile in the presence of proton donor and consists with proton couple electron transfer process.

The overall reaction is shown below

$$CO_2 + 2e^- + 2H^+ = CO + H_2O$$

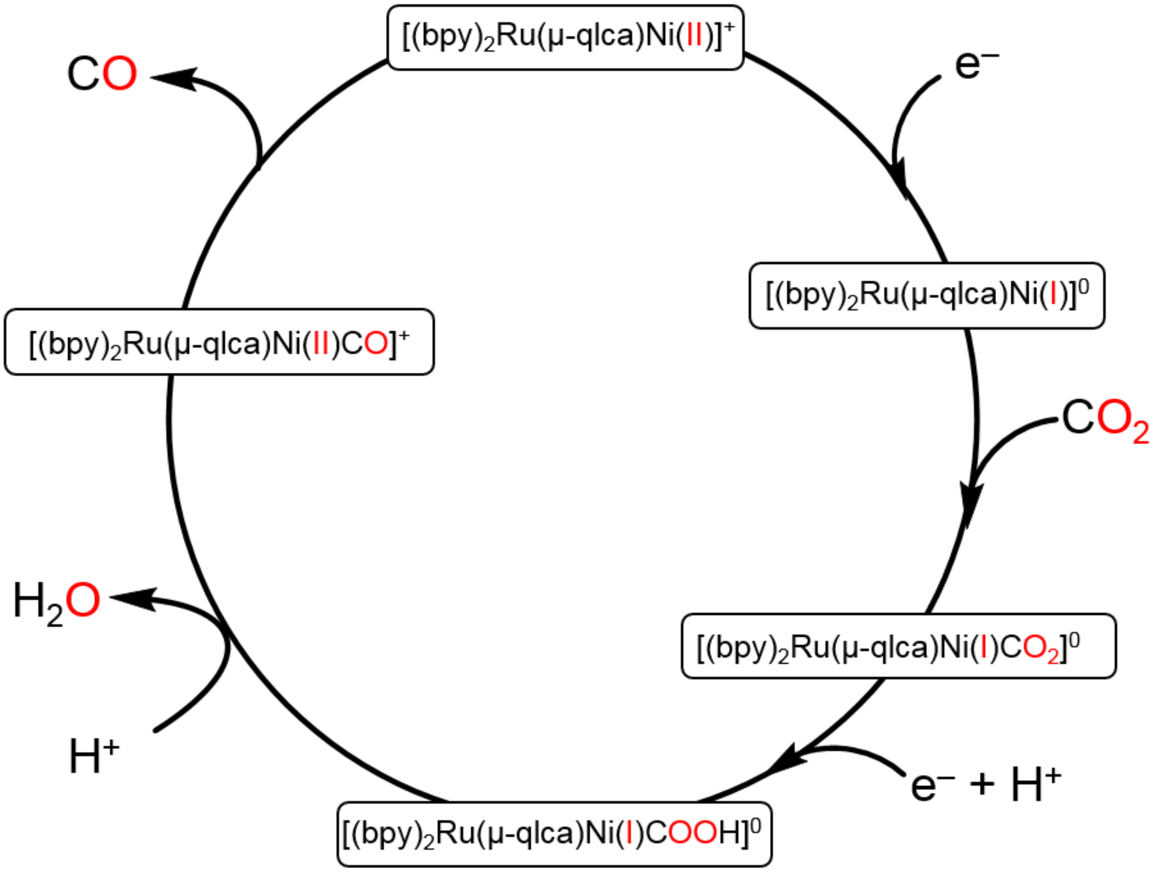

Figure 2.12. Propose catalytic mechanism for CO_2 reduction to CO by $[(bpy)_2Ru(\mu\text{-qlca})NiCl_2]Cl$ based on previous studies.

2.7 Conclusions

Incorporating, redox-active ditopic ligand coordinated metal complex into an electrocatalyst improved the electrocatalytic abilities towards the reduction of CO_2 to CO. Between the abilities $[\{(bpy)_2Ru\}(\mu\text{-qlca})NiCl_2]Cl)$ and $([Ni(qlca)Cl_2]^-$ to reduce CO_2 to CO in wet CH_3CN showed that the $\{Ru(bpy)_2\}^{2+}$ moiety has a dramatic effect on the electrocatalyst. The faradaic efficiency increased from 60% to 82%, and the turnover frequency increased by 144-fold. More importantly, the overpotential was 350 mV lower for $[\{(bpy)_2Ru\}(\mu\text{-qlca})NiCl_2]Cl$ than $[Ni(qlca)Cl_2]^-$. The redox-active ligand coordinated metal complex increases the electron density near the catalytic active site to increase catalytic rate and shifted the electrocatalytic potential positively due to inductive effects from Ru^{2+} ions. In other words, redox-active ligand coordinated metal complexes tethered electrocatalytic active site is a new way of improving CO_2 reduction abilities. In the future, we will explore our method using other electrocatalysts.

2.8 Experimental

General considerations. All chemicals were reagent grade obtained from commercial sources and used without further purification. Quinolone-2-carbaldehyde (pyridine-2-carbonyl) hydrazone (qlca) was synthesized following a reported procedure.[58] *cis*-[Ru(bpy)$_2$Cl$_2$] was prepared according to the reported procedure.[59] Tetrabutylammonium hexafluorophosphate (TBAPF$_6$, Aldrich, 98%) was recrystallized from hot ethanol and dry under a vacuum at 90 °C overnight.

Characterization and Instrumentation. Single-crystal X-ray diffraction data were collected on a Bruker APEX-II diffractometer with an APEX II CCD detector and *JAPAN thermal Engineering Co., Ltd* Cryo system DX-CS190LD. The crystal structure was solved by using direct methods (SIR2004[60] or SHELXS-97[61]), followed by Fourier syntheses. Structure refinement was performed by using full matrix least-squares procedures using SHELXL-97[2] on F^2 in the Yadokari-XG 2009 software.[5] Elemental analysis and ESI-MS measurements were performed at the Research and Analytical centre for Giant Molecules, Tohoku University.

Electrochemistry. Electrochemistry was performed using an ALS/HCH Model 620D electrochemical analyser. A glassy carbon (3 mm diameter) electrode was used as a working electrode, Pt wire was used as a counter electrode, and Ag wire was used as a reference electrode. The supporting electrolyte was 0.1 M tetrabutylammonium hexafluorophosphate (TBAPF$_6$) in dry CH$_3$CN and in 5% H$_2$O and CH$_3$CN (v/) solution mixture. N$_2$ and CO$_2$ gas were bubbled into the solutions at least 30 min before cyclic voltammetry was performed. All potentials were converted to NHE.

Controlled Potential Electrolysis. Controlled potential electrolysis (CPE) experiments were performed by using an ALS/HCH Model 620D electrochemical analyser. A Gamry five-neck cell was used for all experiments. A cell was equipped with three Ace-Thread ports used for each electrode and two joints used for gas purging and gas collection after electrolysis. A piece of Pt wire was used for the counter electrode and Ag wire for reference electrode. Both are separated from the bulk solution by the porous frit. A glassy carbon working electrode was used for the working electrode (surface area 0.196 cm^2). The experiment was performed using 0.1 M $TBAPF_6$ in dry CH_3CN and 5% H_2O and CH_3CN (v/v) solution mixture. The solution was purged with CO_2 gas for 30 min before electrolysis. Gas-phase products were sampled using a gas-tight syringe to confirm CO_2 reduction product. A gas chromatograph (Agilent 6890N, 5975C) equipped with Agilent HP-MOLESIEVE, length 30 m, ID, 0.32 mm, film 12 μm columns was used for product identification. Helium (99.99%) was used as the carrier gas, *m*/*z* range: 10–100. Gas chromatography calibration curve was prepared using a known volume of CO gas. CPE measurements were performed at three times for every sample. The Faradic efficiency was calculated by dividing the actual amount of CO produce during control potential experiment (CPE), and the amount of CO expected based on the charge passed during the CPE experiments. The Turnover frequency (TOF) was calculated based on Eq. S1 and Eq. S3. The reported TOF and Faradic efficiency are averaged values.

Synthesis of Ethyl pyridine-2-carboxylate: Concentrated sulfuric acid (25 mL) was added dropwise to a solution of 2-picolinic acid (24.6 g, 0.2 mol) in anhydrous ethanol (120 mL) surrounded by an ice-water bath. The mixture was refluxed for 24 h. Upon cooling to ambient temperature, the product was poured into 100 mL ice-water. The resulting solution was neutralized to pH of 7–8 with a solution of potassium carbonate. The precipitate was filtered, and the filtrate was extracted with ether (4 × 100 mL). After drying over magnesium sulfate, the organic phases were evaporated to dryness under reduced pressure. The unpurified ester can be used for next hydrazinolysis.

Synthesis of Pyridine–2-carbonylhydrazine: A mixture of above ester 2.80% hydrazine hydrate (19 mL, 0.4 mol) and ethanol (50 mL) was refluxed for 8 h. Then the solution was evaporated to dryness, and the resulting white solid was recrystallized from anhydrous ethanol to give 3 as colorless needles (20.4 g, 74.5% for a two-step reaction). Melting point: 97–98 °C (lit. mp 100–101°C[29]); FTIR (ν, cm^{-1}): 3310, 3213, 3051, 1676, 1652, 1594, 1570, 1521, 1473, 1070, 998.

Synthesis of Quinoline-2-carbaldehyde (Pyridine-2-carbonyl)-hydrazone (qlca): Quinoline-2-carbaldehyde (pyridine-2-carbonyl)-hydrazone was prepared according to literature procedure.[62] 2-Pyridinecarboxylic acid (1372 mg, 10 mmol) was dissolved in (50 mL) ethanol in round bottle flask, and then 2-quinoline-carbaldehyde (1572 mg, 10 mmol) was added with stirring. The solution mixture was heated to reflux for 5 h, and then the solution was cooleed to room temperature. The solution was concentrated to about 5 mL. The concentrated solution was allowed to stand 1 h, during which time a pale yellow precipitated formed. The precipitate was collected by using filtration and then dried in vacuo. Yield: 82%. Product was confirmed by using ^{1}H-NMR to be a mixture of *E/Z* isomers. The mixture was used for next step without separation.

Synthesis of [{(bpy)$_2$Ru^{II}}(μ-qlca)]Cl . To a solution of the qlca (276 mg, 1 mmol) in ethanol (50 mL) in a round bottle flask was added 484 mg (1 mmol) of *cis*-[Ru(bpy)$_2$Cl$_2$]. The solution mixture was refluxed for 8 h. The solvent was removed under reduced pressure. The solid was purified by using chromatography over Bio-beads S-X1 with CH_2Cl_2. The first fraction was collected, and the solvent evaporated to obtain black-red solid. Yield: 80%. ESI-MS: *m/z* = 669.13. Anal. Calcd for $C_{36}H_{28}N_8ORuCl$: C, 59.62; H, 3.89; N, 15.45%. Found: C, 59.71; H, 3.81; N, 15.47%.

Synthesis of [{(bpy)$_2$Ru^{II}}(μ-qlca)Ni^{II}Cl$_2$]Cl. [{(bpy)$_2$Ru^{II}}(μ-qlca)]Cl (69 mg, 0.1 mmol) was dissolved in 10 mL of ethanol, and then nickel chloride·6H_2O (23 mgm, 0.1 mmol) was added. The mixture was stirred at room temperature for 6 h, during which a blackish red precipitate formed. The precipitate was collect and washed with ethanol. Black plate-type single crystals were obtained from methanol/diethyl ether. Yield: 75%. ESI-MS: *m/z* = 817.00. Anal. Calcd for $C_{36}H_{27}N_8Cl_3ONiRu$: C, 50.64; H, 3.19; N, 13.12%. Found: C, 50.59; H, 3.27; N, 13.15%.

Synthesis of [Ni(qlca)Cl$_2$]$^-$. qlca (376 mg, 1 mmol) was dissolved in 15 mL of ethanol, and one drop of triethylamine was added. Nickel chloride·6H_2O (23 mg, 1 mmol) was dissolved in 10 mL ethanol, and the solution was added to the solution containing the ligand. The mixture was stirred for 1 h at room temperature, during which a precipitate formed. The precipitate was collected and washed with ethanol. Yield: 92%.

X-ray Crystallography

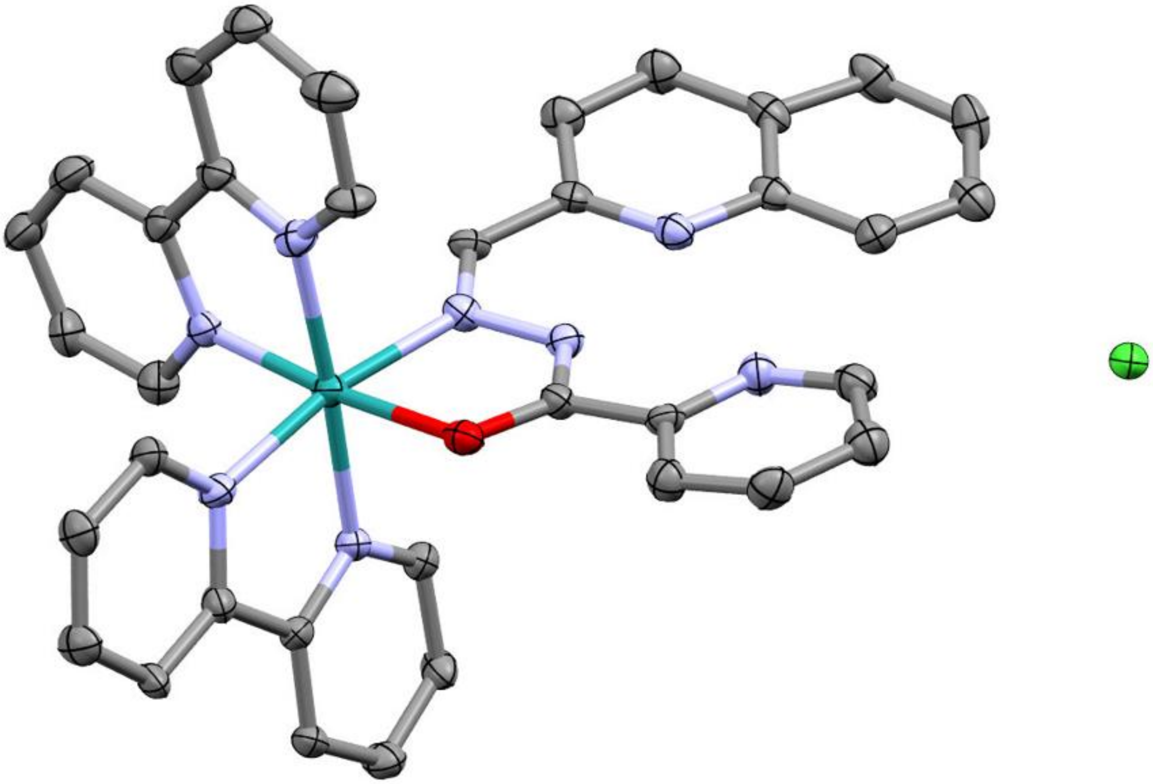

Figure 2.13: ORTEP diagram of [{(bpy)$_2$Ru^{II}}(μ-qlca)]Cl. All atoms are shown by a thermal ellipsoid drawn at the 50% probability level. Hydrogen atoms are omitted for clarity. Red, O; light blue, N; gray, C; green, Cl and Greenish-blue, Ru.

Table 2.2: Crystallographic details for [{(bpy)$_2$Ru^{II}}(μ-qlca)]Cl.

Radiation type, wavelength	Mo Kα, 0.71073
Formula	$C_{36}H_{28}N_8RuOCl\cdot H_2O$
Formula weight	743.20
Crystal system	monoclinic
Space group	*C*2/c
Crystal size (mm^3)	0.3 × 0.2 × 0.06
a (Å)	21.0959(15)
b (Å)	15.0221(10)
c (Å)	27.802(2)
β (deg)	101.891(3)
V (Å^3)	8621.5(10)
Z	2
Temperature (K)	93
Calcd density (g/cm^3)	1.29
μ (mm^{-1})	0.5929
R_1, wR_2 [I>2σ(I)]	0.1462,
R_1, wR_2 [all data]	0.1198, 0.3255
R$_{int}$	0.0886
F(000)	3372
GOF	1.213

Table 2.3: Crystallographic details for $[\{(bpy)_2Ru^{II}\}(\mu\text{-}qlca)Ni^{II}Cl_2]Cl$.

Radiation type, wavelength	Mo Kα, 0.71073
Formula	$C_{37}H_{38.86}Cl_3N_8NiO5.43Ru$
Formula weight	948.64
Crystal system	monoclinic
Space group	P_{21}
Crystal size (mm^3)	0.3 × 0.2 × 0.06
a (Å)	12.458(7)
b (Å)	11.207(7)
c (Å)	15.772(9)
β (deg)	101.850(8)
V (Å^3)	2155(2)
Z	2
Temperature (K)	93
Calcd density (g/cm^3)	1.462
μ (mm^{-1})	1.023
R_1, wR_2 [$I > 2\sigma(I)$]	0.0507, 0.1139
R_1, wR_2 [all data]	0.0623, 0.1207
R_{int}	0.0385
$F(000)$	967
GOF	1.075
Flack parameter	0.17(6)

ESI mass spectrum

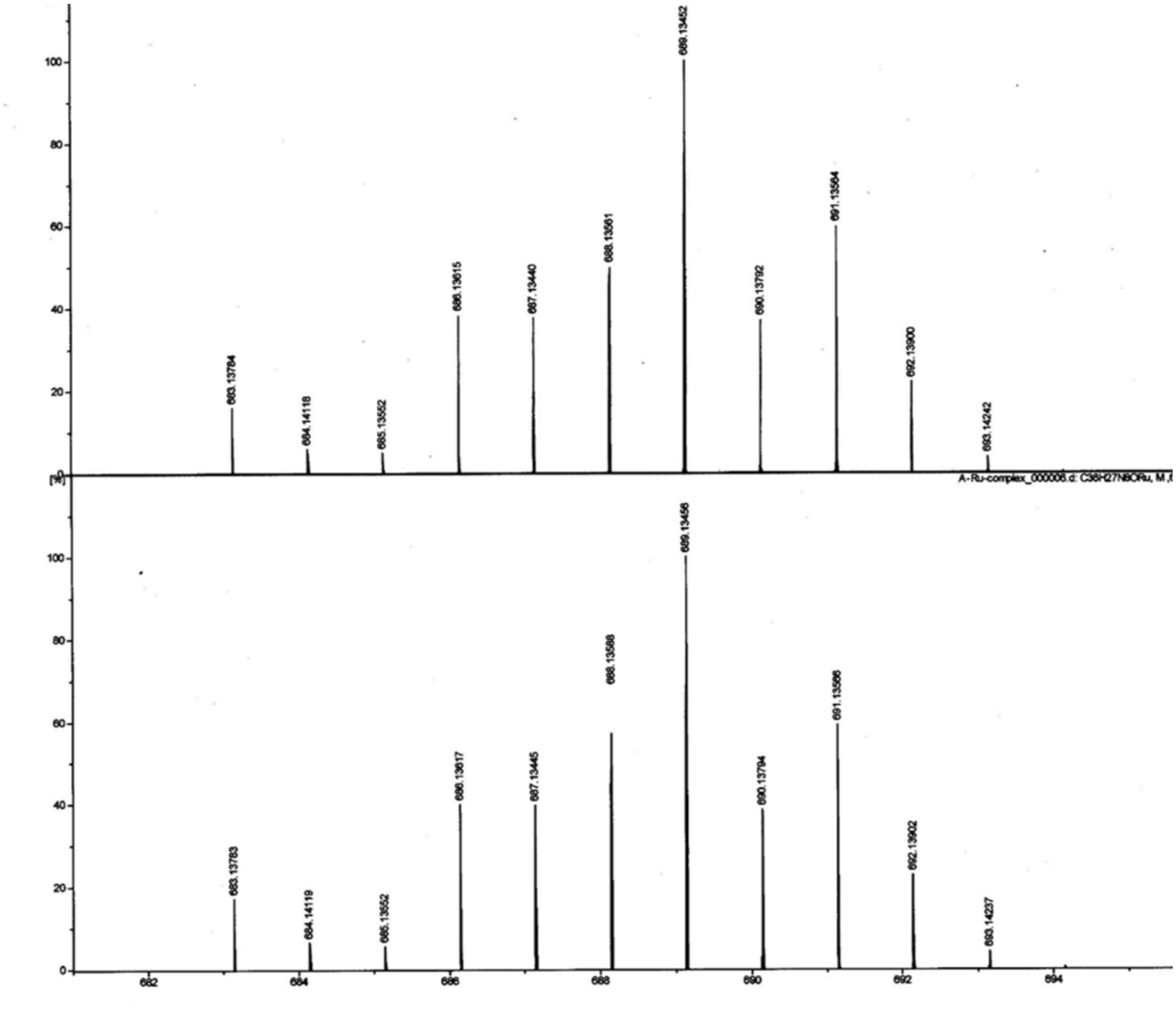

Figure 2.14: ESI mass spectrum of $[\{(bpy)_2Ru^{II}\}(\mu\text{-}qlca)]Cl$ with simulation (upper) and experimental (lower)

ESI mass spectrum

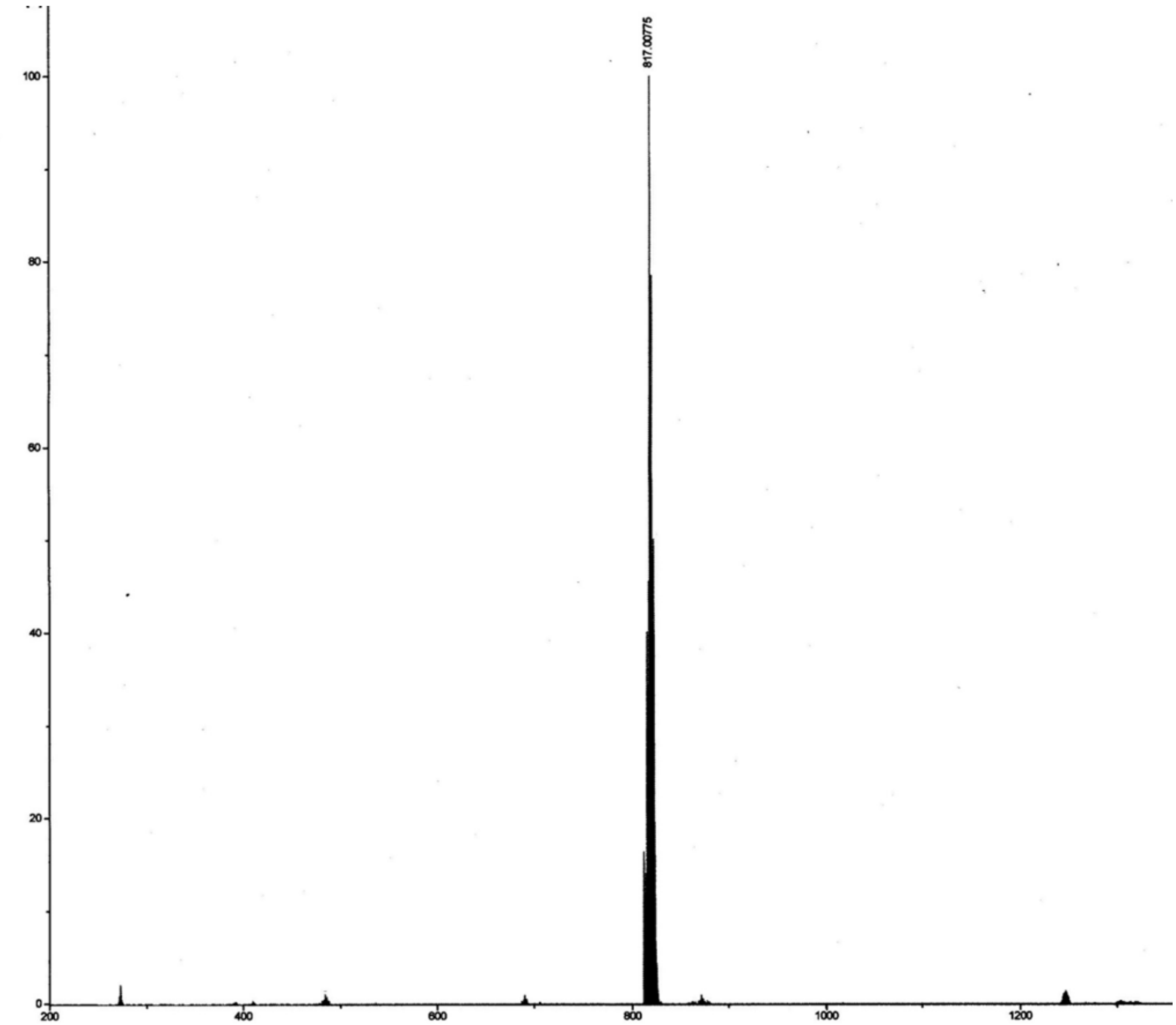

Figure 2.15: ESI mass spectrum of $[\{(bpy)_2Ru^{II}\}(\mu\text{-qlca})Ni^{II}Cl_2]Cl$ with simulation (upper) and experimental (lower)

ESI mass spectrum

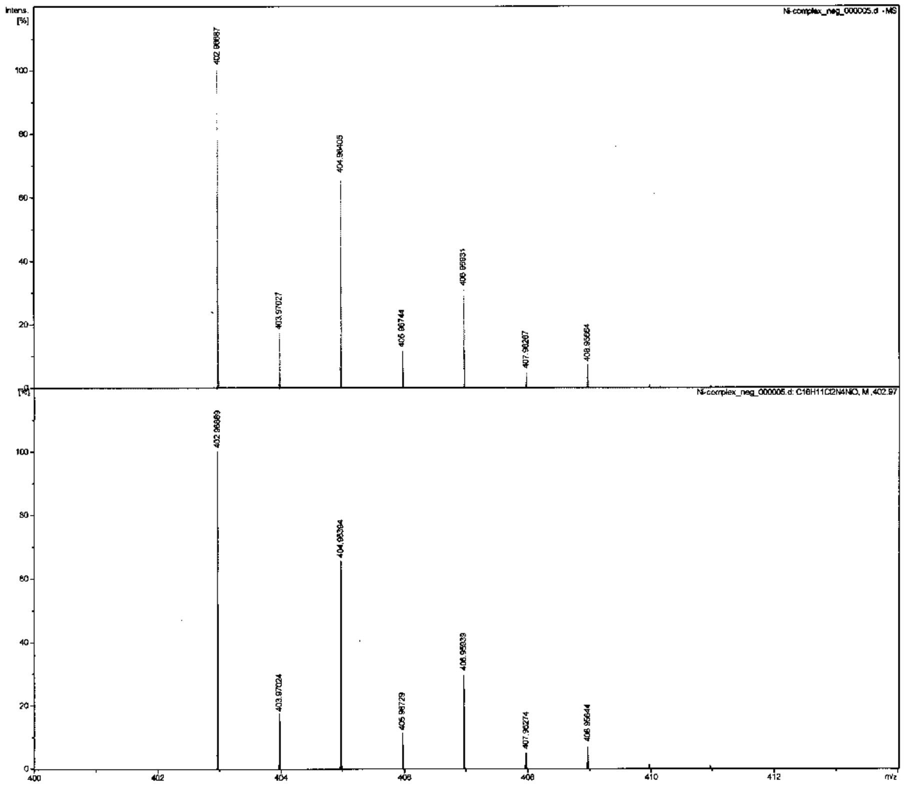

Figure 2.16: ESI mass spectrum of $[Ni(qlca)Cl_2]^-$ with simulation (upper) and experimental (lower)

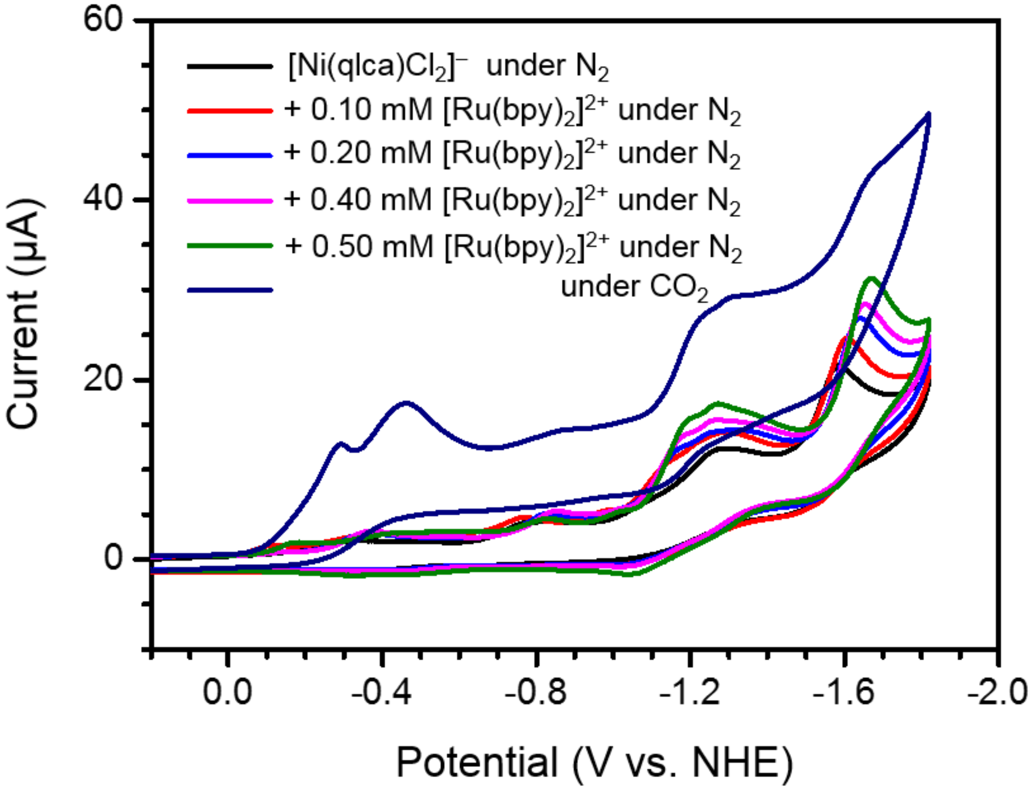

Figure 2.17: Cyclic voltammgrams of (0.5 Mm) [Ni(qlca)Cl$_2$]$^-$ in 5% H_2O and CH_3CN solution mixture with TBAPF$_6$ with adding different amount of {Ru(bpy)$_2$}$^{2+}$. Scan rate 0.1 V/s. The reduction potential of Ni$^{II/I}$ couples are not shifted positively and catalytic current not increase. There are no effect of free {Ru(bpy)$_2$}$^{2+}$ on catalytic process. In oder to decrease reduction potential of Ni$^{II/I}$ couples and increase catalytic current chemical attachment are very important.

The diffusion coefficient D calculation of $[Ni(qlca)Cl_2]^-$ from cyclic voltammogrms

The cathodic peak current (i_p) and square root scan rate showed linear relationship is given by the Randles-Sevcik equation for homogeneous system.[63] The Randles-Sevcik equation is

$$i_\mathrm{p} = 0.4463 n_\mathrm{p} FA[cat](n_\mathrm{p} FvD/RT)^{1/2} \qquad \text{Eq. S1}$$

Where, where i_p is peak current (A), n_p is the number of electron(s) involves in redox system (1 for $Ni^{II/I}$ redox process), F is the Faraday constant (96500 $C \cdot mol^{-1}$), A is the surface area of working electrode (0.071 cm^2), $[cat]$ is catalysts concentration ($mol \cdot cm^{-3}$), v is the scan rate ($V \cdot s^{-1}$), R is the universal gas constant (8.31 $J \cdot K^{-}1 \cdot mol^{-1}$), and T is the temperature (298 K). The diffusion coefficient D is calculated from the slop of i_p vs. $v^{1/2}$ plot.

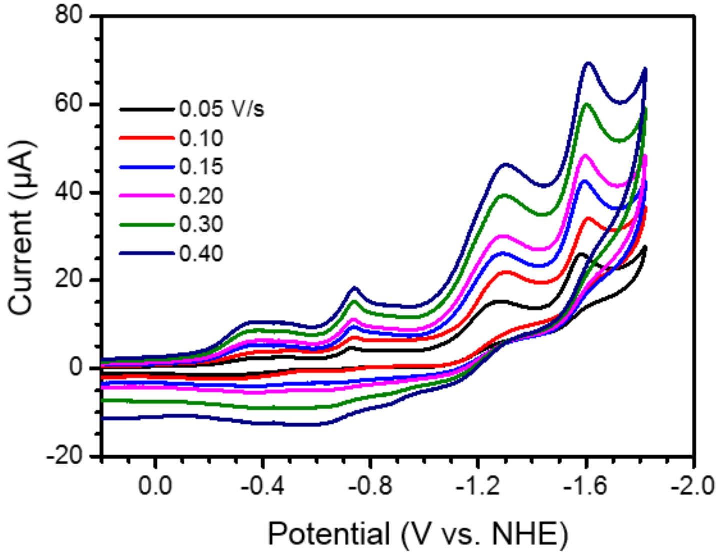

Figure 2.18. Cyclic voltammgrams of 0.5 mM $[Ni(qlca)Cl_2]^-$ in 5% H_2O and CH_3CN (v/v) solution mixture with $TBAPF_6$ at different scan rates. The Ni(II/I) couples are consider for cathodic peak current.

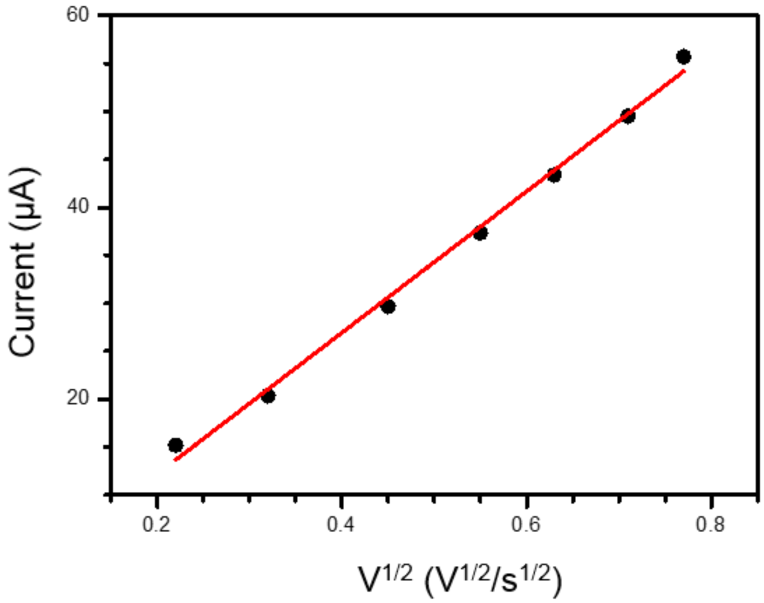

Figure 2.19: Plot of i_p vs. $v^{1/2}$ for $[Ni(qlca)Cl_2]^{-}$, data collected from Figure S6. Peak current consider for $Ni^{II/I}$ reduction couples at corresponding scan rate. The current showing a linear dependence on scan rate, indicating that the reduction of $[Ni(qlca)Cl_2]^{-}$ is a diffusion-controlled process.

The diffusion coefficient for $[Ni(qlca)Cl_2]^{-}$ calculated using Eq. S1 to be 5.13×10^{-5} $cm^2 \cdot s^{-1}$.

The diffusion coefficient D calculation of $[\{(bpy)_2Ru\}(\mu\text{-}qlca)NiCl_2]Cl$ from cyclic voltammogrms

The diffusion coefficient of $[\{(bpy)_2Ru\}(\mu\text{-}qlca)NiCl_2]Cl$ was calculated using Eq. S1.

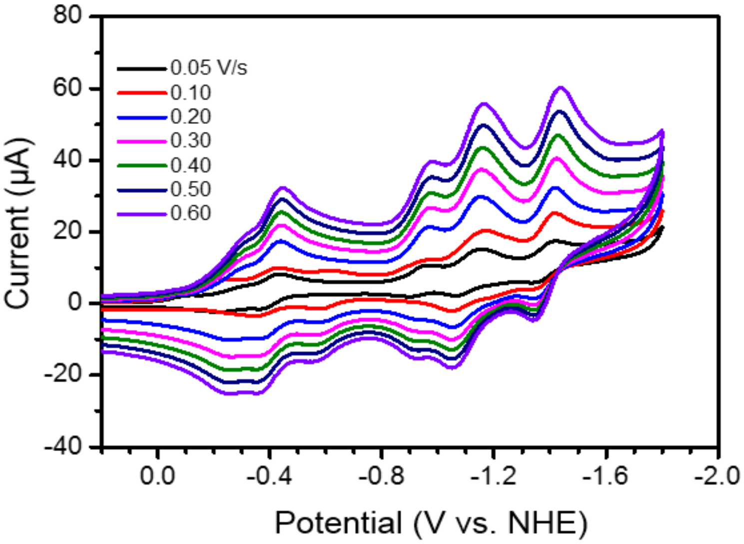

Figure 2.20. Cyclic voltammgrams of 0.5 mM [{(bpy)$_2$Ru}(μ-qlca)NiCl$_2$]Cl in CH$_3$CN solution with TBAPF$_6$ at different scan rates. The Ni$^{II/I}$ couple is consider for cathodic peak current.

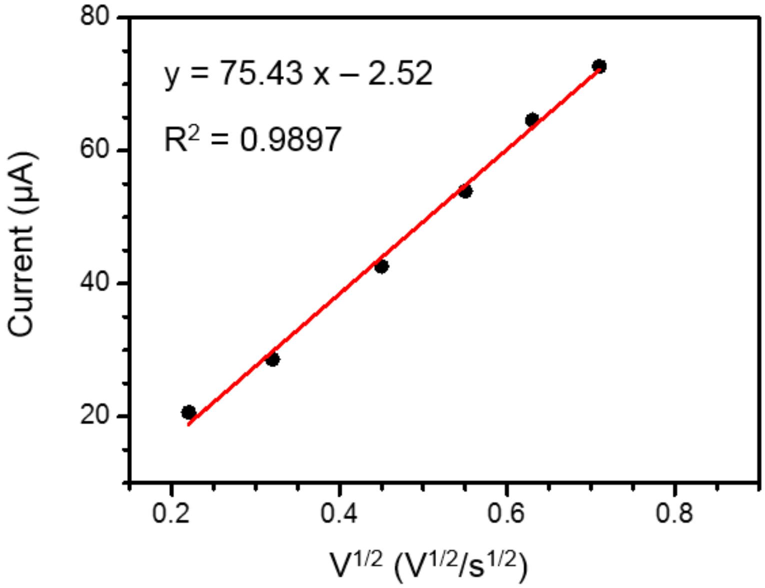

Figure 2.21. Plot of i_p vs. $v^{1/2}$ for [{(bpy)$_2$Ru}(μ-qlca)NiCl$_2$]Cl, data collected from Figure S8. Peak current consider for Ni$^{II/I}$ reduction couples at corresponding scan rate. The current showing a linear dependence on scan rate, indicating that the reduction of [{(bpy)$_2$Ru}(μ-qlca)NiCl$_2$]Cl is a diffusion-controlled process.

The diffusion coefficient for $[\{(bpy)_2Ru\}(\mu\text{-qlca})NiCl_2]Cl$ calculated using Eq. 1 to be $4.86 \times 10^{-5}\ cm^2{\cdot}s^{-1}$.

Turnover frequency (TOF) Calculation Methods

In this work TOF calculation followed by two methods. First method are used for roughly comparison within catalysts and it is underestimated. The method based on, the total amount of CO generated during control potential electrolysis experiments divided by the total amount of catalyst in solution for electrolysis and then divided by time of control potential electrolysis. The equation given below.

$$\text{TOF}_{\text{a}} = \frac{\frac{n[CO]}{n[cat]}}{t} \qquad \text{Eq. S2}$$

Where, n[CO] is the total number of mole CO generate during electrolysis (from GC-MS measurement), n[cat] is the number of moles of catalysts in solution for using for electrolysis and t is the electrolysis time in seconds.

Second method for TOF calculation using cyclic voltammograms and control potentials electrolysis data. The equation used here, modified by McCrory et al from Saveant and co-workers.[64–66]

$$\text{TOF}_{\text{b}} = \frac{(i_{el})^2\ (1 + exp\left[\frac{F}{RT}\left(E_{app} - E_{\frac{1}{2}}\right)\right])}{F^2A^2D[cat]^2} \qquad \text{Eq. S3}$$

Here, i_{el} is average current of CPE for CO generation (A), F is Faraday constant (96500 C·mol), R is the universal gas constant (8.31 $J \cdot K^{-1} \cdot mol^{-1}$), T is the temperature (298 K), E_{app} is the applied potential during CPE, $E_{1/2}$ is the standard redox potential of catalyst, A is the surface area of working electrode(0.194 cm^2), D is the diffusion coefficient for catalyst ($cm^2 \cdot s$) and [cat] is the concentration of catalyst in solution ($mol \cdot cm^{-3}$).

The Faradaic efficiency (FE) is calculated from below equation

$$\mathrm{n[CO]} = \frac{Q_{el} \times FE}{nF} \qquad \text{Eq. S4}$$

Where, n[CO] is the number of mole of CO generated from electrolysis (A), Q_{el} is the charge passed during electrolysis (C) and F is Faraday constant (96500 $C \cdot mol^{-1}$) and n is number of electron needed for conversion of CO_2 to CO (2 electron process).

The average current i_{el} for CO generation during electrolysis is calculated from equation

$$i_{el} = \frac{Q_{el} \times FE}{t} \qquad \text{Eq. 5}$$

Where, Q_{el} is the charge passed during electrolysis (C), FE is Faradaic efficiency of CO (%) and t (s) is time of electrolysis.

TOF calculations of [{(bpy)$_2$Ru}(μ-qlca)NiCl$_2$]Cl catalyst in dry CH$_3$CN solution:

TOF$_a$ was calculated based on, the total amount of CO generated during control potential electrolysis divided by the total amount of catalyst in solution for electrolysis and then divided by time of control potential electrolysis by using Eq. S2

$$\mathrm{TOF}_{\mathrm{a}} = \frac{\frac{n[CO]}{n[cat]}}{t} \qquad \text{Eq. S2}$$

In dry CH$_3$CN solution condition electrolysis was performed at –1.40 V vs. NHE and used 2 mg catalyst in 5 mL solution. So, the catalysts concentration in solution was 4.90×10^{-7} mol·cm^{-3}. The GC-MS analysis confirmed that the CO$_2$ reduction product was CO in gaseous state. The amount of CO generated was 6.7×10^{-7} mol. So, the TOF$_a$ was calculated to be 7.55×10^{-4} s^{-1} by using Eq. S2.

Faradaic efficiency

The Faradaic efficiency is defined as the ratio of the actual amount of CO produce during CPE electrolysis and the amount of CO expected based on charge passed during CPE.

$$\mathrm{n[CO]} = \frac{Q_{el} \times FE}{nF} \qquad \text{Eq. S4}$$

$$FE = \frac{n[CO] \times nF}{Q_{el}} \qquad \text{Eq. S4.1}$$

Where, n[CO] is 6.7 × 10^{-7} mol, n is 2 (reduce CO_2 to CO needed 2 electron), *F* is faraday constants 96500 C·mol and Q_{el} is charge passed during CPE 0.42 C.

Using Eq. S4.1 the Faradaic efficiency was calculated to be 31%.

TOF_b calculation

$$\mathrm{TOF}_{\mathrm{b}} = \frac{(i_{el})^2\ (1 + exp\left[\frac{F}{RT}\left(E_{app} - E_{\frac{1}{2}}\right)\right])}{F^2A^2D[cat]^2} \qquad \text{Eq. S3}$$

Where, i_{el} is the average current value based on Faradaic efficiency (31%) during CPE and calculated by using

$$i_{el} = \frac{Q_{el} \times FE}{t} \qquad \text{Eq. S5}$$

Q_{el} value is 0.42 C, *FE* value is 31% and t is CPE time 1800 s. The i_{el} calculated to be 7.2×10^{-5} A. The *F* is Faraday constant (96500 $C \cdot mol^{-1}$), *A* is the surface area of glassy carbon working electrode (0.196 cm^2), *D* is the diffusion coefficient (4.86×10^{-5} $cm^2 \cdot s^{-1}$), *R* is universal gas constant (8.31 $J \cdot K^{-1} \cdot mol^{-1}$), *T* is the temperature (298 K), E_{app} is the applied potential of CPE (–1.40 V vs. NHE) and the $E_{1/2}$ is the standard redox potential of catalyst (–1.20 V vs. NHE). Using those above value in Eq. S3, the TOF_b for the $[\{(bpy)_2Ru\}(\mu\text{-qlca})NiCl_2]Cl$ catalysts in dry CH_3CN solution condition was calculated to be 2.30 s^{-1}.

TOF calculations of [{(bpy)$_2$Ru}(μ-qlca)NiCl$_2$]Cl catalyst in 5% H_2O and CH_3CN solutions mixture:

TOF$_a$ was calculated based on, the total amount of CO generated during control potential electrolysis divided by the total amount of catalyst in solution for electrolysis and then divided by time of control potential electrolysis by using Eq. S2

$$\text{TOF}_{\text{a}} = \frac{\frac{n[CO]}{n[cat]}}{t} \qquad \text{Eq. S2}$$

In 5% H_2O and CH_3CN solutions mixture condition electrolysis was performed at –1.20 V vs. NHE and used 2 mg catalyst in 5 mL solution. So, the catalysts concentration in solution was 4.90×10^{-7} mol·cm^{-3}. The GC-MS analysis confirmed that the CO_2 reduction product was CO in gaseous state. The amount of CO generated was 4.67×10^{-6} mol. So, the TOF$_a$ was calculated to be 5.29×10^{-3} s^{-1} by using Eq. S2.

Faradaic efficiency

The faradaic efficiency is defined as the ratio of the actual amount of CO produce during CPE and the amount of CO expected based on charge passed during CPE.

$$\text{n[CO]} = \frac{Q_{el} \times FE}{nF} \qquad \text{Eq. S4}$$

$$FE = \frac{n[CO] \times nF}{Q_{el}} \qquad \text{Eq. S4.1}$$

Where, n[CO] is 4.67×10^{-6} mol, n is 2 (reduce CO_2 to CO needed 2 electron), F is Faraday constants 96500 $C \cdot mol^{-1}$ and Q_{el} is charge passed during CPE 1.10 C.

Using Eq. S4.1 the Faradaic efficiency was calculated to be 82%.

TOF_b calculation

$$\mathrm{TOF}_{\mathrm{b}} = \frac{(i_{el})^2\ (1 + exp\left[\frac{F}{RT}\left(E_{app} - E_{\frac{1}{2}}\right)\right])}{F^2 A^2 D[cat]^2} \qquad \text{Eq. 3}$$

Where, i_{el} is the average current value based on Faradaic efficiency (82%) during CPE and calculated by using

$$i_{el} = \frac{Q_{el} \times FE}{t} \qquad \text{Eq. S5}$$

Q_{el} value is 1.10 C, FE value is 82% and t is CPE time 1800 s. The i_{el} calculated to be 5.01×10^{-3} A. The F is Faraday constant (96500 $C \cdot mol^{-1}$), A is the surface area of glassy carbon working electrode (0.196 cm^2), D is the diffusion coefficient (4.86×10^{-5} $cm^2 \cdot s^{-1}$), R is universal gas constant (8.31 $J \cdot K^{-1} \cdot mol^{-1}$), T is the temperature (298 K), E_{app} is the applied potential of CPE (–1.20 V vs. NHE) and the $E_{1/2}$ is the standard redox potential of catalyst (–1.20 V vs. NHE). Using those above value in Eq. S3, the TOF_b for the $[\{(bpy)_2Ru\}(\mu\text{-qlca})NiCl_2]Cl$ catalysts in 5:95 H_2O and CH_3CN solution condition was calculated to be 120 s^{-1}.

TOF calculations of $[Ni(qlca)Cl_2]^-$ catalyst in 5% H_2O and CH_3CN solutions mixture:

TOF_a was calculated based on, the total amount of CO generated during control potential electrolysis divided by the total amount of catalyst in solution for electrolysis and then divided by time of control potential electrolysis by using Eq. S2

$$\mathrm{TOF}_{\mathrm{a}} = \frac{\frac{n[CO]}{n[cat]}}{t} \qquad \text{Eq. S2}$$

In 5% H_2O and CH_3CN solutions mixture condition electrolysis was performed at –1.55 V vs. NHE and used 2 mg catalyst in 5 mL solution. So, the catalysts concentration in solution was 9.9×10^{-7} $\mathrm{mol \cdot cm^{-3}}$. The GC-MS analysis confirmed that the CO_2 reduction product was CO in gaseous state. The amount of CO generated was 5.70×10^{-7} mol. So, the TOF_a was calculated to be 3.16×10^{-4} s^{-1} by using Eq. S2.

Faradaic efficiency

The Faradaic efficiency is defined as the ratio of the actual amount of CO produce during CPE and the amount of CO expected based on charge passed during CPE.

$$\mathrm{n[CO]} = \frac{Q_{el} \times FE}{nF} \qquad \text{Eq. S4}$$

$$FE = \frac{n[CO] \times nF}{Q_{el}} \qquad \text{Eq. S4.1}$$

Where, n[CO] is 5.70×10^{-7} mol, n is 2 (reduce CO_2 to CO needed 2 electron), F is Faraday constants 96500 C·mol and Q_{el} is charge passed during CPE 0.18 C.

Using Eq. S4.1 the Faradaic efficiency was calculated to be 61%.

TOF$_b$ calculation

$$\mathrm{TOF}_b = \frac{(i_{el})^2\ (1 + exp\left[\frac{F}{RT}\left(E_{app} - E_{\frac{1}{2}}\right)\right])}{F^2 A^2 D [cat]^2} \qquad \text{Eq. S3}$$

Where, i_{el} is the average current value based on faradaic efficiency (61%) during CPE and calculated by using

$$i_{el} = \frac{Q_{el} \times FE}{t} \qquad \text{Eq. S5}$$

Q_{el} value is 0.18 C, FE value is 61% and t is CPE time 1800 s. The i_{el} calculated to be 6.10×10^{-4} A. The F is Faraday constant (96500 C·mol), A is the surface area of glassy carbon working electrode (0.196 cm^2), D is the diffusion coefficient (5.13×10^{-5} $cm^2 \cdot s^{-1}$), R is universal gas constant (8.31 $J \cdot K^{-1} \cdot mol^{-1}$), T is the temperature (298 K), E_{app} is the applied potential of CPE (–1.55 V vs. NHE) and the $E_{1/2}$ is the standard redox potential of catalyst (–1.32 V vs. NHE). Using those above value in Eq. S3, the TOF$_b$ for the $[Ni(qlca)Cl_2]^-$ catalysts in in 5% H_2O and CH_3CN solution condition was calculated to be 0.83 s^{-1}.

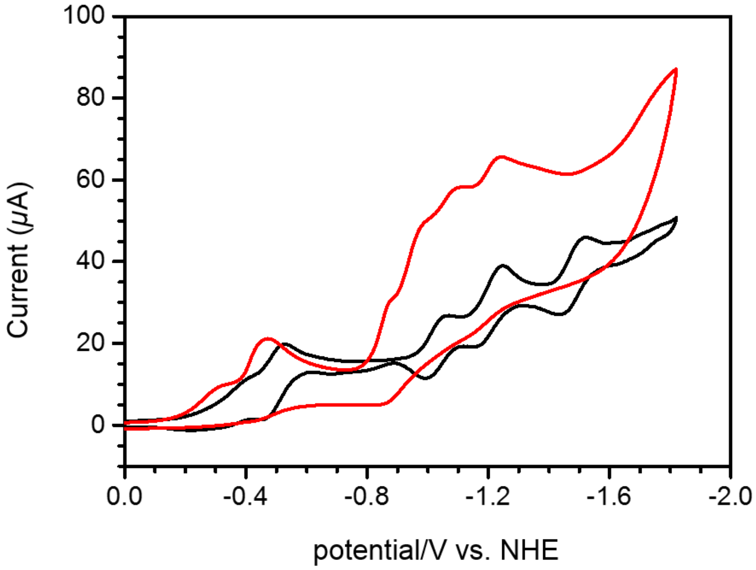

Figure 2.22: CVs of [{(bpy)$_2$Ru}(μ-qlca)NiCl$_2$]Cl before (red) and after (black) control potential electrolysis at –1.20 V vs. NHE in a CO_2 saturated H_2O and CH_3CN. The CVs showed that the solution retains the catalytic activity.

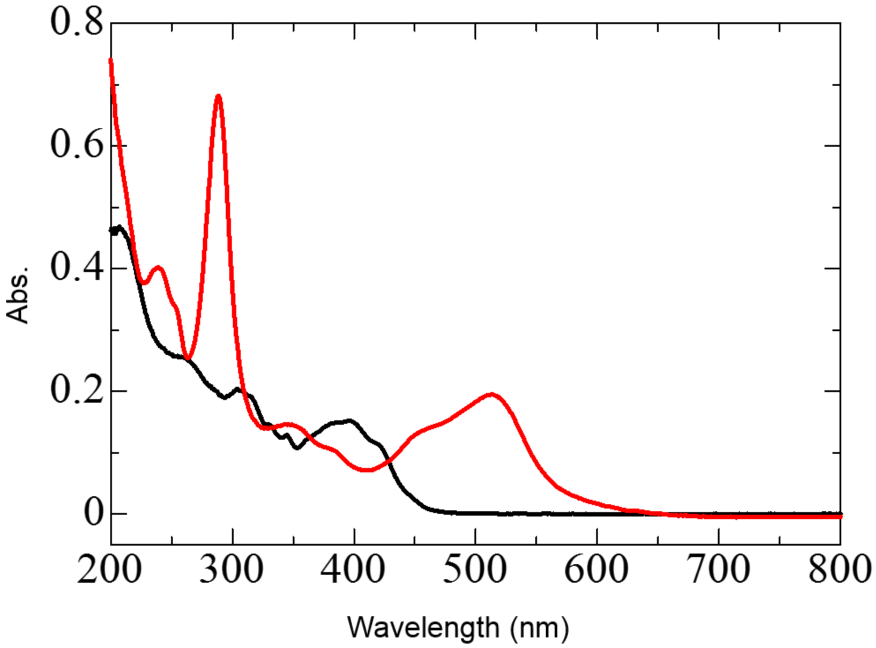

Figure 2.23: UV-Vis spectra of [{(bpy)$_2$Ru}(μ-qlca)NiCl$_2$]Cl (red) and [Ni(qlca)Cl$_2$]$^-$ (black).

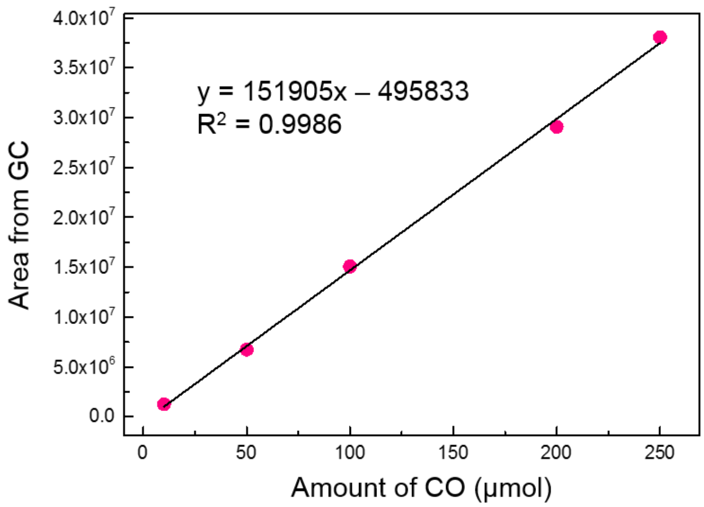

Figure 2.24: Calibration curve for known amount CO from gas chromatography

References

1. J. Qiao, Y. Liu, F. Hong and J. Zhang, *Chem. Soc. Rev.*, 2014, **43**, 631–675.
2. E. E. Benson, C. P. Kubiak, A. J. Sathrum and J. M. Smieja, *Chem. Soc. Rev.*, 2009, **38**, 89–99.
3. D. T. Whipple and P. J. A. Kenis, *J. Phy. Chem. Lett.*, 2010, **1**, 3451–3458.
4. Y. Li, S. H. Chan and Q. Sun, *Nanoscale*, 2015, **7**, 8663–8683.
5. C. Genovese, C. Ampelli, S. Perathoner and G. Centi, *J. Energy, Chem.*, 2013, **22**, 202–213.
6. M. Hammouche, D. Lexa, M. Momenteau and J. M. Saveant, *J. Am. Chem. Soc.*, 1991, **113**, 8455–8466.
7. M. D. Samson and C. P. Kubiak, *J. Am. Chem. Soc*., 2016, **138**, 1386–1393.

8. J. M. Smieja, M. D. Sampson, K. A. Grice, E. E. Benson, J. D. Froehlich and C. P. Kubiak, *Inorg. Chem*., 2013, **52**, 2484–2491.
9. M. D. Sampson, A. D. Nguyen, K. A. Grice, C. E. Moore, A. L. Rheingold and C. P. Kubiak, *J. Am. Chem. Soc.*, 2014, **136**, 5460–5471.
10. C. Riplinger, M. D. Sampson, A. M. Ritzmann, C. P. Kubiak and A. E. Carter, J. Am. Chem. Soc., 2014, 136, 16285–16298.
11. K. T. Ngo, M. McKinnon, B. Mahanti, R. Narayanan, D. C. Grills and M. Z. Ertem, J. Rochford, *J. Am. Chem. Soc.*, 2017, **139**, 2604–2618.
12. C. W. Machan, M. D. Sampson and C. P. Kubiak, *J. Am. Chem. Soc.*, 2015, **137**, 8564–8571.
13. M. L. Clark, K. A. Grice, C. E. Moore, A. Rheingold and C. P. Kubiak, *Chem. Sci*., 2014, **5**, 1894–1900.
14. G. Neri, I. M. Aldous, J. J. Walsh, L. J. Hardwick and A. J. Cowan, *Chem. Sci.*, 2016, **7**, 1521–1526.
15. C. Costentin, S. Drouet, M. Robert and J. M. Saveant, *Science*, 2012, **338**, 90–94.
16. C. W. Machan, S. A. Chabolla and C. P. Kubiak, *organometallics*, 2015, **34**, 4678–4683.
17. M. Bourrez, F. Molton, S. C. Noblat and A. Deronzier, *Angew. Chem. Int. Ed.*, 2011, **50**, 9903–9906.
18. E. Fujita and J. T. Muckerman, *Inorg. Chem*., 2004, **43**, 7636–7647.

19. J. A. Therrien, M. O. Wolf and B. O. Patrick, Inorg. Chem., 2015, 54, 11721–11732.

20. J. M. Smieja and C. P. Kubiak, *Inorg. Chem*., 2010, **49**, 9283–9289.

21. J. A. Keith, K. A. Grices, C. P. Kubiak and E. A. Carter, *J. Am. Chem. Soc.*, 2013, **135**, 15823–15829.

22. Z. Chen, C. Chen, D. R. Weinberg, P. Kang, J. J. Concepcion, D. P. Harrison, M. S. Brookhart and T. J. Meyer, *Chem. Commun.*, 2011, **47**, 12607–12609.

23. W. Nie, C. C. L. McCrory, *Chem. Commun*., 2018, **54**,1579–1582.

24. D. C. Lasy, C. C. L. MaCrory and J. C. Peters, *Inorg. Chem*., 2014, **53**, 4980–4988.

25. X. Su, K. M. McCardle, J. A. Panetier and J. W. Jurss, *Chem. Commun.*, 2018, **54**, 3351–3354.

26. F. W. Liu, J. Bi, Y. Sun, S. Lue and P. Kang, *ChemSusChem*. 2018, **11**, 1–9.

27. T. J. Schmeier, G. E. Dobereiner, R. H. Crabtree and N. Hazari, *J. Am. Chem. Soc.*, 2011, **133**, 9274–9277.

28. R. Langer, Y. D. Posner, G. Leitus, L. J. W. Shimon, Y. B. David and D. Milstein, *Angew. Chem. Int. Ed.*, 2011, **50**, 9948–9952.

29. G. A. Andrade, J. L. DiMeglio, E. T. Guardino, G. P.A. Yap and J. Rosenthal, *Polyhedron*, 2017, **135**, 134–143.

30. W.H. Wang, Y. Himeda, J. T. Muckerman, G. F. Manbeck and E. Fujita, *Chem. Rev*., 2015, **115**, 12936–12973.

31. M. Sheng, N. Jiang, S. Gustafson, B. You, D. H. Ess and Y. Sun, *Dalton, Trans.*, 2015, **44**, 16247–16250.

32. R. Narayanan, M. Mckinnon, B. R. Reed, K. T. Ngo, S. Groysman and J. Rochford, *Dalton Trans.,* 2016, **45**, 15285–15289.

33. B. K. Breedlove, D. Takayama and T. Ito, *Chem. Lett.,* 2004, **33**, 1624– 1625.

34. H. E. Toma and K. Araki, *Coord. Chem. Rev.,* 2000, **196**, 307–329.

35. B. K. Breedlove, R. kandel, H. M. Ahsan and M. Yamashita, *Dalton Trans.,* 2014, **43**, 7683–7686.

36. A. H. Reath, J. W. Ziller, C. Tsay, A. J. Ryan and Y. Yang, *Inorg. Chem.*, 2017, **56**, 3713–3718.

37. A. Mori, T. Suzuki, Y. Sunatsuki, A. Kobayashi, M. Kato, M. Kojima and K. Nakajima, *Eur. J. Inorg. Chem.,* 2014, 186–197.

38. A. Mori, T. Suzuki, Y. Sunatsuki, M. Kojima and K. Nakajima, *Bull. Soc. Jpn.,* 2015, **88**, 186–197.

39. A. Gennaro, A. A. Isse, M. G. Severin, E. Vianello, I. Bhugun and J. M. Saveant, *J. Chem. Soc., Faraday Trans.*, 1996, **92**, 3963–3968.

40. M. D. Sampson and C.P. Kubiak, *Inorg. Chem*., 2015, **54**, 6674–6676.

41. R. Francke, B. Schille and M. Roemelt, *Chem. Rev.*, 2018, **118**, 4631–4701.

42. C. Cometto, L. Chen, P. K. Lo, Z. Guo, K. C. Lau, E. A. Mallart, A. Fave, T C. Lau and M. Robert, *ACS Catal.*, 2018, **8**, 3411–3417.

43. I. Azcarate, C. Costentin, M. Robert and J. M. Saveant, *J. Am. Chem. Soc.*, 2016, **138**, 16639–16644.

44. J. W. Raebiger, J. W. Turner, B. C. Noll, C. J. Curtis, A. Miedaner, B. Cox and D. L. DuBois, *Organometallics*, 2006, **25**, 3345–3351.

45. Z. Chen. C. Chen, D. R. Weinberg, P. Kang, J. J. Concepcion, D. P. Harrison, M. S. Brookhart and T. Meyer, *J. Chem. Commun*., 2011, **47**, 12607–11609.

46. C. Costentin, and J. M. Saveant, *ChemElectroChem*, 2014, **1**, 1226–1236.

47. C. Costentin, M. Robert and J. M. Saveant, *Acc. Chem. Res*., 2015, **48**, 2996–3006.

48. C. Costentin, S. Drouet, M. Robert and J. M. Saveant, *J. Am. Chem. Soc*. 2012, **134**, 11235–11242.

49. I. Azcarate, C. Costentin, M. Robert and J. M. Saveant, *J. Phy. Chem. C*. 2016, **120**, 28951–28960.

50. J. Song, E. L. Klein, F. Neese and S. Ye, *Inorg. Chem*., 2014, **53**, 7500–7507.

51. J. D. Froehlich and C. P. Kubiak, *J. Am. Chem. Soc.*, 2015, **137**, 3565–3573.

52. J. Schneider, H. Jia, J. T. Muckerman and E. Fujita, *Chem. Soc. Rev*., 2012, **41**, 2036–2051.

53. J. D. Froehlich and C. P. Kubiak, *Inorg. Chem*., 2012, **51**, 3932–3934.

54. S. Sakaki, N. Koga and K. Morokuma, *Inorg. Chem.*, 1990, **29**, 3110–3116.

55. A. Dedieu and F. Ingold, *Angew. Chem., Int. Ed. Engl.*, 1989, **28**, 1694–1995.

56. C. Costentin, M. Robert and J. M. Saveant, *Chem. Rev.*, 2010, **110**, PR1–PR40.

57. S. Hammes-Schiffer, *Energy Environ. Sci.*, 2012, **5**, 7696–7703.

58. A. Mori, T. Suzuki, Y. Sunatsuki, M. Kojima and K. Nakajima, *Bull. Soc. Jpn.,* 2015, **88**, 186–197.

59. G. A. Lawrance, D. R. Stranks and S. Suvachittanont, *Inorg. Chem.,* 1978, **17**, 3322–3325.

60. M. C. Burla, R. Caliandro, M. Camalli, B. Carrozzini, G. L. Cascarano, L. D. Caro, C. Giacovazzo, G. Polidoria and R. Spagnac, *J. Appl. Cryst.*, 2005, **38**, 381–388.

61. G. M. Sheldrick, *Acta Crystallogr.,* 2008, **A64**, 112–122.

62. Wakita, K. Yadokari-XG, Software for Crystal Structure Analyses; 2001; Release of Software (Yadokari-XG 2009) for Crystal Structure Analyses, C. Kabuto, S. Akine, T. Nemoto and E. Kwon, *J. Crystallogr. Soc. Jpn.,* 2009, 51, 218–224.

63. A. J. Bard, L. R. Faulkner, Electrochemical Methods: *Fundamentals and Applications*, 2nd ed., John Wiley, New York, 2001.

64. W. Nie, C. C. L. McCrory, *Chem. Commun.*, 2018, **54**,1579–1582.

65. C. Costentin, S. Drouet, M. Robert and J. M. Saveant, *Science,* 2012, **338**, 90–94.

66. C. Costentin, M. Robert and J. M. Saveant, *Chem. Soc. Rev.,* 2013, **42**, 2423–2436.

Chapter 3

Enhancement of electrocatalytic abilities of a modified Ni(cyclen) complex towards CO_2 reduction

3.1 Introduction

Conversion of CO_2 to value-added compounds, like alternative fuels and fuel precursors by electrochemical reduction process still suffers from several challenges, including low catalytic activity, high overpotential and catalyst stability.[1–5] Therefore, it is important to develop a CO_2 reduction electrocatalytic system to overcome those challenges. Many molecular electrocatalytic systems have been applied to improve electrocatalytic abilities, including proton source utilization,[6–10] like Lewis acid cation such as Mg^{2+} utilization and the most popular strategy to utilize H_2O, methanol, trifluoroethanol, trifluoroacetic acid and phenol.[11–21] A variety of electrocatalysts utilize polypyridyl, phosphinyl, porphyrinyl, phthalocyanato and bulky bipyridyl ligands with metal ions have been studied for CO_2 reduction.[22–35] In early 90s, Saveant and co-workers, reported iron(0) porphyrins electrocatalysts for CO_2 reduction.[11] However, the iron(0) porphyrins electrocatalysts were unstable during catalysis process. When a Lewis acid cation, like Mg^{2+} was added, the reactivity of the catalysts increased. Mechanistic studies have shown that the Mg^{2+} ion helps to break a C=O bond in CO_2 coordinate bound to iron ion affording Fe(II)CO and $MgCO_3$. However, formation of $MgCO_3$ was not good because it is insoluble in electrolysis solution. Later, Saveant and co-workers found that CO_2 reduction in the presence of a weak Bronsted acid as a proton source was enhanced, and this method still play a significant role in the development of efficient and selective electrocatalysts.[30]

In 1974, Meshitsuka and co-workers reported the phathalocyanato cobalt and nickel electrocatalysts, which were the first examples of transition metal electrocatalysts for the reduction CO_2.[36] 1,4,8,11-Tetraazacyclotetradecane (cyclam) supported nickel and cobalt metal electrocatalysts were reported by Eisenberg and co-workers in 1980.[37] Their electrocatalysts reduce CO_2 to CO with high current efficiency, but turnover frequencies in water and acetonitrile solution are low. After that, complexes with macrocyclic ligands have been extensively studied as electrocatalysts.[38] Most of nickel macrocyclic complexes have been investigated by using Hg working electrode. However, Balazs and co-workers have shown that the electrocatalytic active species $[Ni(cyclam)]^+$ strongly adsorbs on the mercury electrode surface.[39] Kubiak and co-workers have demonstrated that $[Ni(cyclam)]^+$ is still active for CO_2 reduction after adsorption on a glassy carbon electrode.[40,41] Fujita and co-workers have studied the geometric and electronic effects on catalytic activity using different structural derivatives of $[Ni(cyclam)]^{2+}$.[42] However, $[Ni(cyclam)]^{2+}$ still exhibits low electrocatalytic activity, and electrocatalysis occurs at high potentials. Structural modification of macrocyclic electrocatalysts may improve catalytic activity. The use of a local proton source has been shown to be an important method for improving elecrtocatalytic CO_2 reduction. Saveant and co-workers have reported an iron porphyrin with phenolic groups attached to the porphyrin moiety, which operates electrolysis with high efficiencies at a low overpotential.[10] In addition, $[Ni(cyclam–COOH)]^{2+}$ (Cyclam_COOH = 1,4,8,11-tetraazacyclotetradecane-6-carboxylic acid) has been reported to have electrocatalytic activity greater than only the $[Ni(cyclam)]^{2+}$ in acidic media does.[43]

In this work, the main focus is improving electrocatalytic abilities by using a modified macrocyclic ligand coordinated to a redox-active metal complex. The nitrogenase enzyme consists of two components: Fe and MoFe protein. During catalysis electrons are transfer from the Fe protein to the MoFe protein to facilitate nitrogen fixation at the MoFe site.[44] In this work, $\{Ru(bpy)_2Cl\}^+$ ($[Ru]^+$; bpy = 2,2'-bipyridine) was used similar to the Fe protein of nitrogenase that it can transfer electrons to the active site. 1,4,7,10-Tetraazacyclododecane (cyclen) was modified with 4-pyridyl methyl methyl groups used as the supporting ligand for the CO_2 reduction active site because it is more rigid, and $[Ru]^+$ were connected to the active site via the 4-pyridyl methyl groups The analogous $[ben_4cyclenNiCl]Cl$ (ben = benzyl) was synthesized and investigated to understand the effects of redox-active ligand coordinated metal complex on electrocatalytic properties.

3.2 Results and discussion

The ligand $ben_4cyclen$ was prepared by using benzyl chloride instead of 4-pyridylmethyl chloride. To obtain $ben_4cyclen$, a solution of 1,4,7,10-tetraazacyclododecane (cyclen) and the solution of benzyl chloride in acetonitrile was refluxed in the presence of potassium carbonate.[45] The ligand $ben_4cyclen$ was characterized by using NMR spectroscopy and elemental analysis (Experimental section). [$ben_4cyclenNiCl$]Cl was synthesized by mixing equimolar amounts of $ben_4cyclen$ and

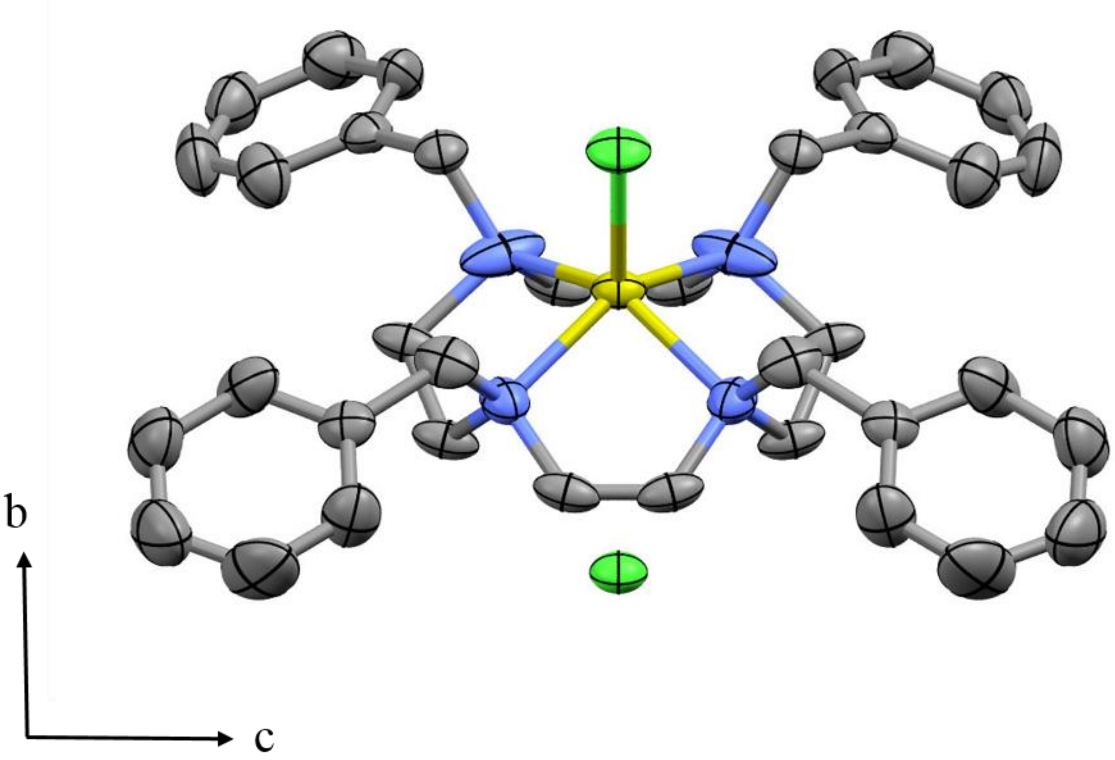

Figure 3.1: ORTEP diagram of [$ben_4cyclenNiCl$]Cl with thermalellepsoids at 50% probability. Hydrogen atoms and disordered carbon atoms are omitted for clarity. Gary: carbon atoms; blue: nitrogen atoms; yellow: nickel atom and green: chloride atoms.

$NiCl_2\cdot 6H_2O$ in ethanolic solution. Green pentagonal plate-like crystals were obtained from methanol and diethylether solution mixture after one day.

An ORTEP diagram of [ben$_4$cyclenNiCl]Cl shown in Figure 2.1, and crystal data aresummarized in Table 3.3. [ben$_4$cyclenNiCl]Cl crystalized in the orthorhombic space group $Ccm2_1$. The Ni^{II} ion adopted a square-pyramidal geometry due to the four nitrogen atoms of cyclen and one chloride atoms. The Ni ion site 0.607(6) Å above the plane of four nitrogen atoms of cyclen ring. The counter anion Cl(2) is at the opposite side of the apical Cl ion (Ni–Cl (2): 4.59(5) Å). Selected bond length and angles are listed in Table 3.1..

Table 3.1: Selected bond distance (Å) and angles (deg) for [ben$_4$cyclenNiCl]Cl

Bond distance	Bond angles
Planar N–Ni = 0.607	N(1)–Ni–Cl(1) = 107.27
Ni–Cl(1) = 2.254(2)	N(2)–Ni–Cl(1) = 107.27
Ni–Cl(1) = 4.597(5)	N(3)–Ni–Cl(1) = 106.17
Ni–N(1) = 2.113(8)	N(4)–Ni–Cl(1) = 106.17
Ni–N(2) = 2.113(8)	
Ni–N(3) = 2.107(4)	
Ni–N(4) = 2.107(4(	

In order to obtain the target electrocatalyst $[\{([Ru]pic)_4cyclen\}NiCl]^{5+}$, $pic_4cyclen$ (pic = 4-methylpyridyl) was synthesized by treating a mixture of cyclen·4HCl and 4-methylpyridylchloride hydrochloride with 6 M NaOH(aq). The ligand $pic_4cyclen$ was characterized by using NMR spectroscopy, elemental analysis, and X-ray crystallography (Experimental section). The ligand was then coordinated to $[Ru]^+$ to obtain $[([Ru]pic)_4cyclen)]^{4+}$. The complexed ligand $[([Ru]pic)_4cyclen)]^{4+}$ was coordinated to $NiCl_2$, which acts as the active site for CO_2 reduction.

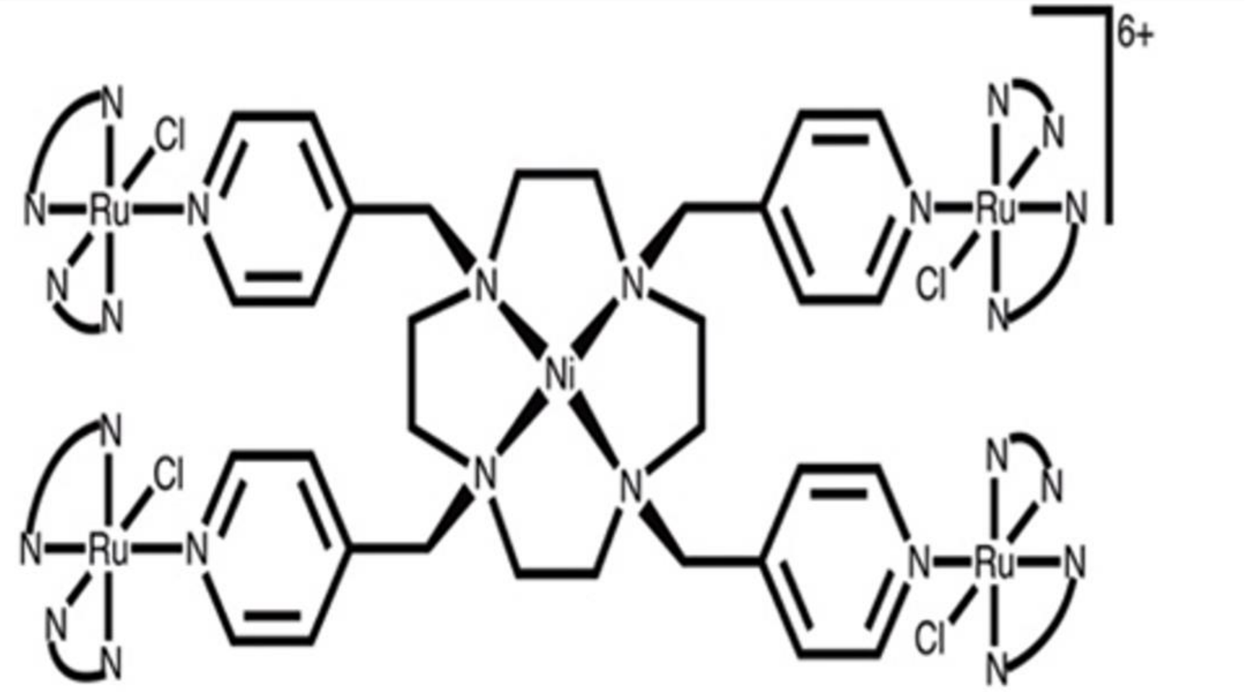

Figure 3.2: Diagram of the electrolectrocatalyst with redox-active coordinate metal complex $[\{([Ru]pic)_4cyclen\}NiCl]^{5+}$ where $[Ru]^+ = [Ru(bpy)_2Cl]^+$ and bpy = 2,2`-bipyridine.

3.3 Electrochemical studies

Cyclic voltammetry (CV) is a powerful electrochemical technique to investigate the reduction and oxidation process of molecular species and important way to study electron transfer initiated chemical reaction, including electrocatalysis. Cyclic voltammetry was performed in 5:95 H_2O/CH_3CN solutions (v/v) containing 0.1M tetrabutylammonium hexafluorophosphate ($TBAPF_6$). The CV using $[\{[Ru]pic_4cyclen\}NiCl]^{5+}$ was performed in dry CH_3CN and 5% H_2O in CH_3CN solutions (v/v) and it was found that CO_2 reduction product depended on the solvent. The CV were performed with $[Ru]^+$, $[([Ru]pic)_4cyclen]^{4+}$, $[\{([Ru]pic)_4cyclen\}Ni^{II}]^{6+}$ and $[ben_4cyclenNiCl]Cl$ to understand the effects of $[Ru]^+$ on the lectrocatalyst.

3.3.1 Cyclic voltammograms of [ben₄cyclenNiCl]Cl

Cyclic voltammograms of $[ben_4cyclenNiCl]Cl$ in 5:95/H_2O CH_3CN solutions (v/v) containing 0.1M $TBAPF_6$ are shown in Figure 3.3. Under N_2, a reversible wave for the $Ni^{II/I}$ couple was observed at –0.55 V vs. NHE. It is at a potential more positive than that for $[Ni(cyclam)]^{2+}$ and analogs due to the effect of benzyl group attached to the amide N atoms on the cyclen ring.[40] The $Ni^{I/0}$ couple is not observed. After saturating the solution with CO_2, the cathodic current increased around –1.45 V vs. NHE. The cathodic wave shifted positively in relation to that observed in the N_2 saturated solution and it was irreversible indicating CO_2 reduction occured. The catalytic current increase is similar to that using $[Ni(cyclam)]^{2+}$ derivatives in mixtures of H_2O and CH_3CN.[37,38, 40–42]

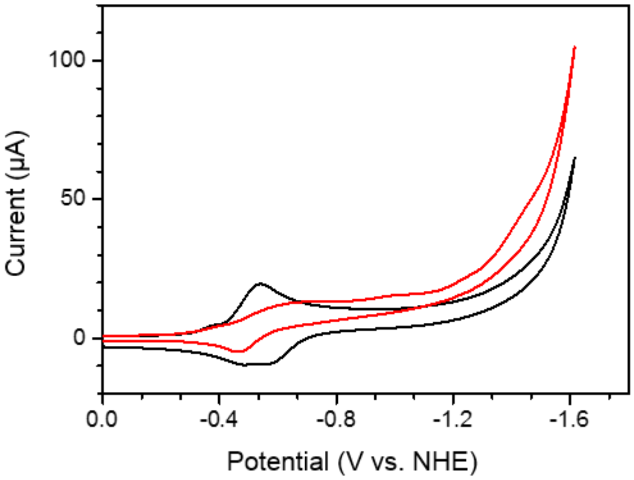

Figure 3.3: Cyclic voltammograms of [ben$_4$cyclenNiCl]Cl in 5% H_2O and CH_3CN solution mixture containing 0.1 M TBAPF$_6$ under N_2 (black) and CO_2 (red). The scan rate was 0.1 Vs^{-1}. A glassy carbon electrode was used as the working electrode.

3.3.2 Cyclic voltammograms of [Ru]$^+$

Cyclic voltammograms of [Ru]$^+$ in H_2O/CH_3CN solutions (v/v) containing 0.1 M TBAPF$_6$ as supporting electrolyte under N_2 (black line) and under CO_2 (red line) atmosphere are shown in Figure 3.4. In the cyclic voltammograms of [Ru]$^+$ two reduction waves at –0.55 V and –1.45 V vs. NHE, which were assigned to the reduction of bpy to bpy$^{\cdot-}$ in the first and second bpy respectively, were observed. Under CO_2, a small increase for catalytic current, which is not surprising because ruthenium ions can activated CO_2.

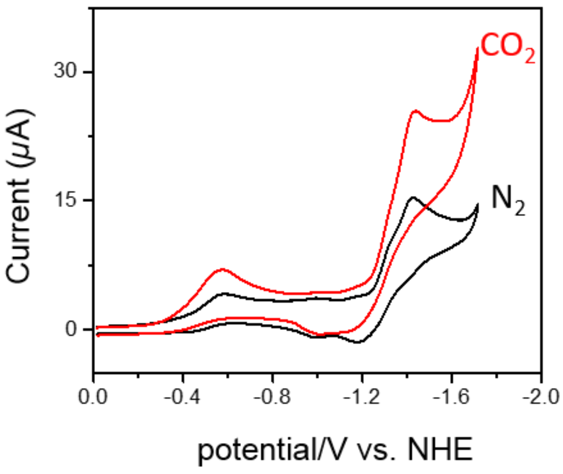

Figure 3.4: Cyclic voltammograms of [Ru] in 5% H_2O and CH_3CN solution mixture containing 0.1 M $TBAPF_6$ under N_2 (black) and CO_2 (red). The scan rate was 0.1 Vs^{-1}. A glassy carbon electrode was used as the working electrode.

3.3.3 Cyclic voltammograms of $[([Ru]pic)_4cyclen]^{4+}$

Cyclic voltammetry was performed on the supporting ligand pic$_4$cyclen coordinated to four $[Ru]^+$ moieties via pyridine N atoms and $[([Ru]pic)_4cyclen]^{4+}$ to better understand the catalytic process, and cyclic voltammograms under N_2 and CO_2 are shown in Figure 3.5. In the cyclic voltammograms of $[([Ru]pic)_4cyclen]^{4+}$, three reduction waves at –0.65 V, –1.30 V and –1.58 V vs. NHE were observed. The first and second waves were due to the reduction of bpy to $bpy^{\cdot-}$, and they are shifted from original $[Ru]^+$ reduction potential. The third reduction wave was assigned to the chloride ion dissociation from $[Ru]^+$ moieties. The catalytic current increased under CO_2 atmosphere, indicating reduction occurred at the ruthenium center. However, this current increase is negligible.

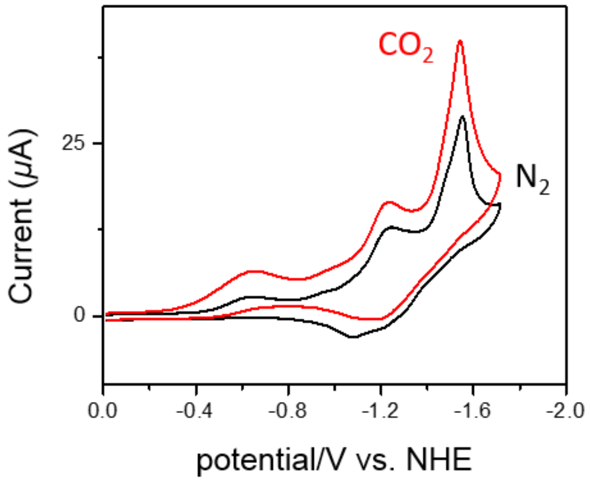

Figure 3.5: Cyclic voltammograms of [([Ru]pic)$_4$cyclen]$^{4+}$ in 5% H_2O and CH_3CN solution mixture containing 0.1 M TBAPF$_6$ under N_2 (black) and CO_2 (red). The scan rate was 0.1 Vs^{-1}. A glassy carbon electrode was used as the working electrode.

3.3.4 Cyclic voltammograms of [{([Ru]pic)$_4$cyclen}NiCl]$^{5+}$ in dry CH_3CN

Cyclic voltammograms of [{([Ru]pic)$_4$cyclen}NiCl]$^{5+}$ in dry CH_3CN solution containing 0.1 M TBAPF$_6$ are shown in Figure 3.6. In the cyclic voltammograms four reduction waves were observed under N_2 atmosphere. The reduction wave at –1.06 V vs. NHE assigned for Ni$^{II/I}$,[46] which shifted to a more negative value upon coordination by [Ru]$^+$. The reduction wave at –1.28 V vs. NHE was assigned to the reduction of one of the bpy ligand and the wave at –1.56 V vs. NHE was due to the reduction of the second bpy ligand. The reduction wave at –1.78 V vs. NHE was assigned to Ni$^{I/0}$ couple. When cyclic voltammograms was performed under CO_2 atmosphere, a large current increase at –1.60 V vs. NHE was observed, indicating reduction of CO_2. The cathodic current was higher than those using other macrocyclic based electrocatalysts, showing that the

$[Ru]^+$ moieties electronically affect the electrocatalyst. The catalytic active site Ni(II) ion and the four redox-active $[Ru]^+$ moieties are reduced before CO_2 reduction process, and electrons transferred from $[Ru]^+$ to the active site. From a comparison with [ben$_4$cyclenNiCl]Cl, it is clear that the redox-active ligand coordinated metal complexes tethered to the catalytic active site have a big effect on the on the electrocatalytic activity.

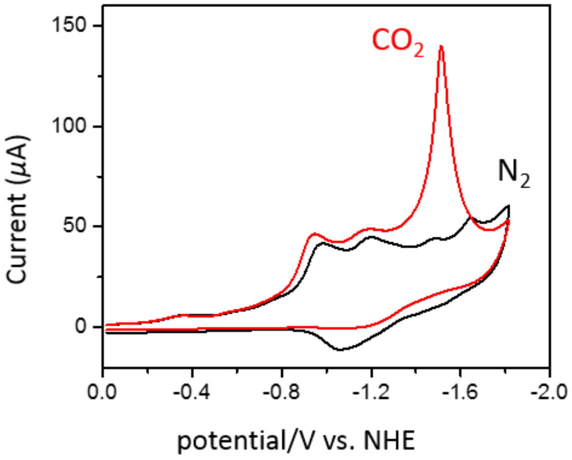

Figure 3.6: Cyclic voltammograms of $[\{([Ru]pic)_4cyclen\}NiCl]^{5+}$ in dry CH_3CN containing 0.1 M $TBAPF_6$ under N_2 (black) and CO_2 (red). The scan rate was 0.1 Vs^{-1}. A glassy carbon electrode was used as the working electrode.

3.3.5 Cyclic voltammograms of $[\{([Ru]pic)_4cyclen\}Ni^{II}]^{6+}$ in 5:95 H_2O/CH_3Cn (v/v)

Cyclic voltammograms of $[\{([Ru]pic)_4cyclen\}NiCl]^{5+}$ in a mixture of H_2O and CH_3CN containing 0.1 M $TBAPF_6$ are shown in Figure 3.7. Four prominent reduction waves were observed in the negative potential region. The wave at –1.02 V vs. NHE was assigned to the Ni$^{II/I}$ couple.[46] The reduction wave at –1.30 V vs. NHE was assigned to the reduction of one bpy ligand,and the wave at –1.52 V vs. NHE was due to the reduction of the second one. The wave at –1.75 V vs. NHE was assigned to be the Ni$^{I/0}$ couple. After the wave at –1.75 V was shifted positively to –1.60 V, and the current increased dramatically, indicating the electrocatalytic reduction of CO_2.

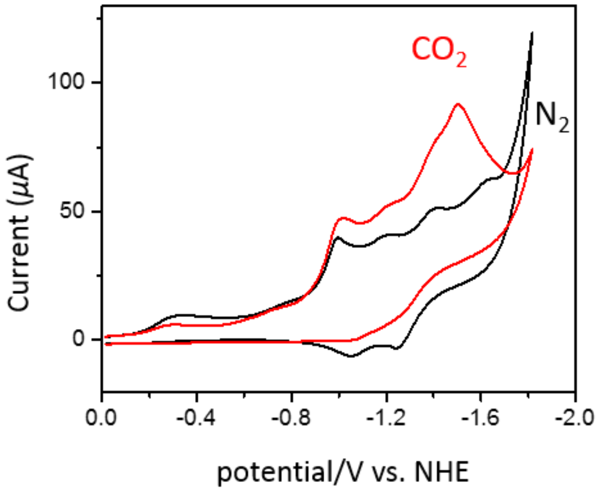

Figure 3.7: Cyclic voltammograms of [{[Ru]pic$_4$cyclen}NiCl]$^{5+}$ in 5% H_2O and CH_3CN solution mixture containing 0.1 M TBAPF$_6$ under N_2 (black) and CO_2 (red). The scan rate was 0.1 Vs^{-1}. A glassy carbon electrode was used as the working electrode.

3.4 Controlled potential electrolysis (CPE) experiments.

3.4.1 CPE of [ben$_4$cyclenNiCl]Cl in 5:95 H_2O/CH_3CN (v/v)

Controlled potential electrolysis (CPE) experiment was performed using in in 5:95 H_2O/CH_3CN (v/v) and a Pt coil working electrode in a sealed cell to confirm the catalytic abilities of [ben$_4$cyclenNiCl]Cl towards CO_2 reduction. The CPE experiments were perform 30 min, and a blank CPE experiment was perform at –1.45 V vs. NHE to confirm the electrocatalysis occurs due to electrocatalysts, during which no activity was observed. Although, the catalyst bind CO_2 at –0.55 V vs. NHE but electrolysis occurs at more negative potential at –1.45 V vs. NHE. Therefore, the CPE experiments were performed at –1.45 V vs. NHE for 30 min. After 30 min electrolysis, it was determined that gaseous product was CO, and the faradaic efficiency and turnover frequency (TOF) value were determined to be 77% and 8.53 s^{-1}, respectively. The values are similar to those using $[Ni(cyclam)]^{2+}$ based electrocatalysts.[37,38, 40–42] The overpotential using [ben$_4$cyclenNiCl]Cl was calculated to be 730 mV (standard reduction potential of CO_2 to CO –0.72 V vs. NHE)[51], which is similarto previously studied electrocatalysts.

3.4.2 CPE of $[\{([Ru]pic)_4cyclen\}NiCl]^{5+}$ in 5:95 H_2O/CH_3Cn (v/v)

CPE experiments using $[\{([Ru]pic)_4cyclen\}NiCl]^{5+}$ were performed in CH_3CN and 5% H_2O solutions to confirm the catalytic activity for 30 min. Although, in the cyclic voltammograms experiments (Figure 3.7) electrocatalysis occurred at –1.60 V vs. NHE (according to cyclic voltammograms). In this work, the electrons from ligand-coordinated redox-active metal complex were used to enhance electrocatalysis at a lower overpotential. So, the CPE experiment were performed at –1.22 V vs. NHE, which is the reduction potential of bpy. The CPE experiment were performed for 30 min, after which headspace gas analysis was performed by using gas chromatography to confirm that the CO_2 reduction product was CO. The faradaic efficiency was 84% and TOF value was 708 s^{-1}. The TOF value 83-times higher than that using [ben$_4$cyclenNiCl]Cl only catalysts analog, indicating the electronic influence of the ligand-coordinated redox-active metal complex on the electrocatalytic active. To the best of our knowledge, the TOF value of $[\{([Ru]pic)_4cyclen\}NiCl]^{5+}$ is the highest value reported for azamacrocycle containing electrocatalysts.[37,38,40–42] Moreover, the overpotential needed using this electrocatalysts (500 mV) much lower than analogous electrocatalysts. In the case of [ben$_4$cyclenNiCl]Cl, CPE experiment was performed at –1.45 V vs. NHE, whereas it could be performed at –1.22 V vs. NHE using [{([Ru]pic)$_4$cyclen}NiCl]$^{5+}$. So, the overpotential decrease by 230 mV for [{([Ru]pic)$_4$cyclen}NiCl]$^{5+}$ due to excess electron presence on catalytic active site form [Ru]$^+$ moieties. In other words, ligand-coordinated redox-active metal complex tethered to catalytic active site is an effective way to improve the electrocatalytic abilities and to decrease the overpotential. Although the faradaic efficiency was slightly lower due to the generation of H_2, the electrocatalysis was still reasonably efficient, and the efficiency should increase when a two-compartment cell is used.

3.5 Catalytic tafel plot

The details of catalytic tafel plots as function of the overpotential (η) and turnover frequency (TOF) were described in chapter 2. The catalytic rate constant under certain conditions corresponds to maximum efficiency of the electrocatalyst 100%[50] is determined from cyclic voltammogram data.[12,47,51–54]

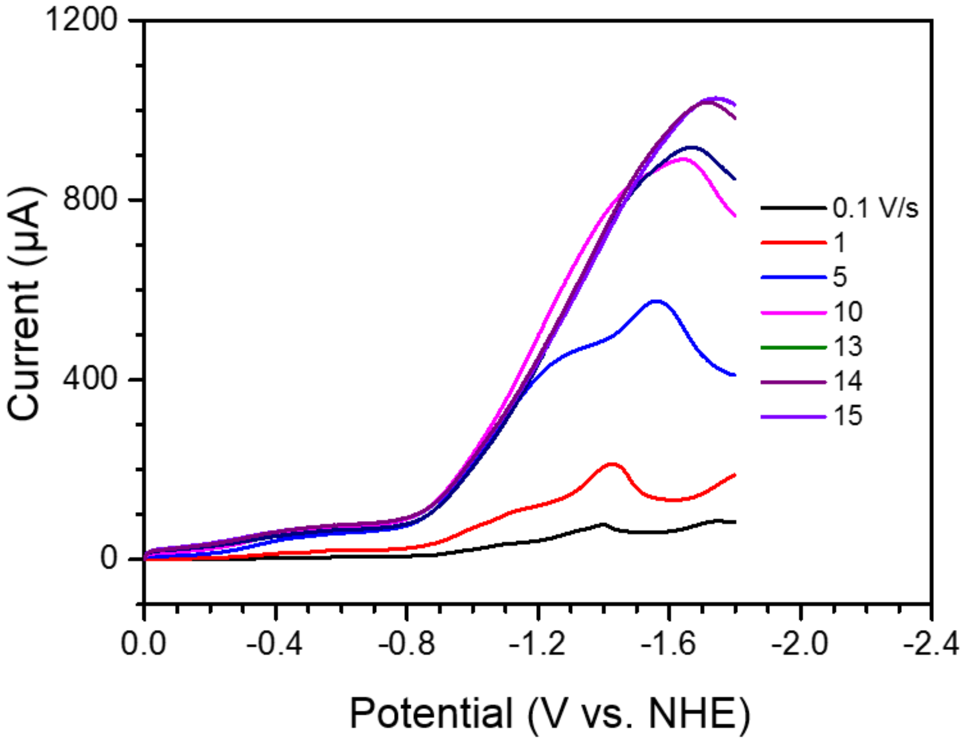

Figure 3.8. Linear sweep voltammograms (LSV) using $[\{([Ru]pic)_4cyclen\}Ni^{II}]^{6+}$ in 5% H_2O and CH_3CN (v/v) solution containing 0.1M $TBAPF_6$ under CO_2 atmosphere using glassy carbon working electrode at the following scan rates (V/s): 0.1, 1, 5, 10, 13, 14 and 15. The catalytic rate independent scan is obtain at scan rate 15 V/s, which is catalytic highest active form.

At a scan rate of 15 V/s a catalytic plateau independent scan rate is obtained, indicating pure kinetic conditions resulting from correlation between catalyst diffusion and fast catalytic rate. The catalytic plateau current is given by Eq. 1:

$$i_{\text{plateau}} = 2FS \times C^{o}_{\text{cat}} \times \sqrt{D_{\text{cat}}} \times \sqrt{k_{\text{cat}}} \qquad \text{....... Eq. 1}$$

where i_{plateau} is the catalytic plateau current, C^{o}_{cat} is the catalytic concentration in the solution, D_{cat} is the diffusion coefficient and k_{cat} is catalytic rate constant.

On the other hand, the one electron diffusion current of the catalysts is given by Eq. 2

$$i^{0}_{\text{peak}} = 0.446 \times \mathrm{FS} \times C^{o}_{\text{cat}} \times \sqrt{D_{\text{cat}}} \times \sqrt{Fv/RT} \qquad \text{........Eq. 2}$$

where i^{0}_{peak} is the noncatalytic current, F is the Faraday constant, v is the scan rate of noncatalytic current (0.1 v/s), R is the universal gas constant and T is the temperature. Dividing Eq. 1 by Eq. 2 affords the $i_{\text{plateau}}/ i^{0}_{\text{peak}}$ ratio which indipendent of S and D_{cat} (Eq. 3)

$$k_{\text{cat}} = (i_{\text{plateau}}/i^{0}_{\text{peak}})^{2} \times 1/ (2 \times 2.24)^{2} \times Fv/RT \qquad \text{...........Eq. 3}$$

From CV data, $i_{\text{plateau}} = 1050$ µA and $i^{0}_{\text{peak}} = 15$ µA.

Thus, using Eq. 3 k_{cat} was calculated to be 836 s^{-1}. The tafel plot for $[\{([\text{Ru}]\text{pic})_4\text{cyclen}\}\text{NiCl}]^{5+}$ was made using Eq. 4.

$$\mathrm{TOF}_{\max} = \frac{k_{cat}}{1+\exp\left[\frac{F}{RT}\left(E^{o}_{CO_2/CO} - E_{\frac{1}{2}}\right)\right] \times \exp\left(-\frac{\mathrm{F}}{\mathrm{RT}}\eta\right)} \qquad \text{..... Eq. 4}$$

In this Eq. 4, $E^{o}_{CO_2/CO}$ is −0.72 V vs. NHE,[41] $E_{1/2}$ is the half-plateau potential of −1.26 V vs. NHE. In this experiment, using η = 800 mV, TOF_{max} was calculated to be 836 s^{-1}. Therefore, log TOF_{max} was 2.92 s^{-1} at 800 mV overpotential and log TOF_0 was −6.19 s^{-1} at zero overpotential.

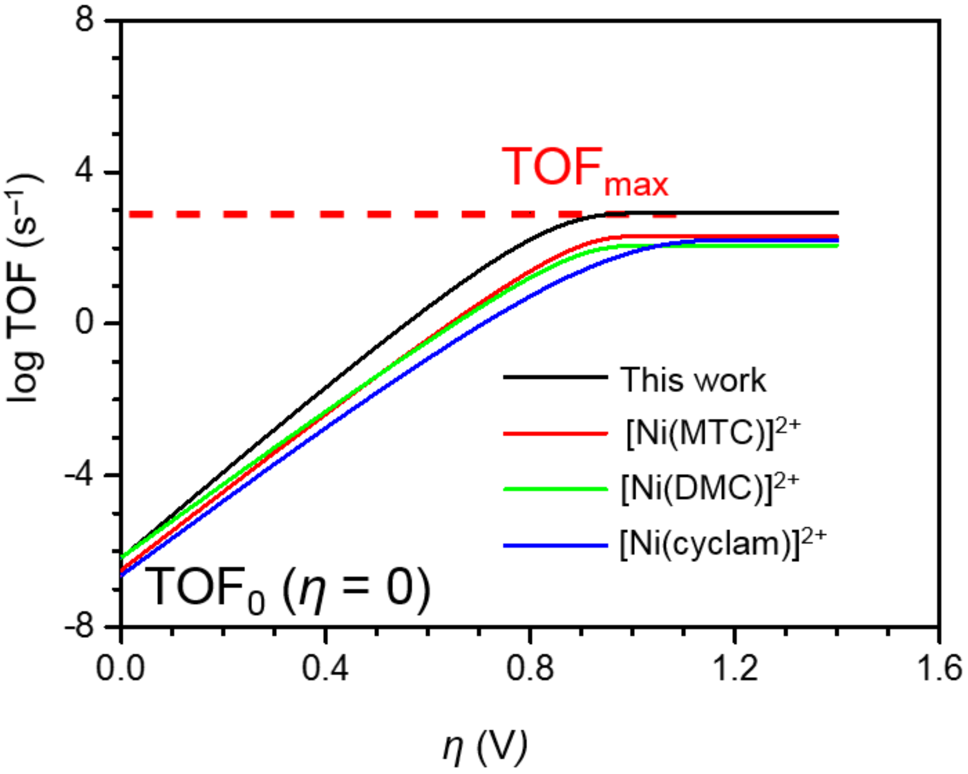

Figure 3.9. Catalytic tafel plots for [{([Ru]pic)$_4$cyclen}NiCl]$^{5+}$, ([Ni(MTC)]$^{2+}$,[42] [Ni(DMC)]$^{2+}$,[42] and [Ni(cyclam)]$^{2+}$.[40]

It can be seen from Figure 3.9 that [{([Ru]pic)$_4$cyclen}NiCl]$^{5+}$ is an excellent electrocatalysts than other macrocycle type electrocatalysts. [{([Ru]pic)$_4$cyclen}NiCl]$^{5+}$ had a higher TOF_{max} at lower overpotential. TOF_{max} for [{([Ru]pic)$_4$cyclen}NiCl]$^{5+}$ at a low overpotential showing in comparison to the value for analogous electrocatalyststhe electronic influence of the ligand-coordinated redox-active metal complex.

3.7 Conclusions

A ligand-coordinate redox-active metal complex tethered the electrocatalytic active site improves electrocatalytic abilities. The electrocatalytic reduction of CO_2 was investigated using $[\{([Ru]pic)_4cyclen\}NiCl]^{5+}$ and $[ben_4cyclenNiCl]Cl$, and I found that both electrocatalysts reduce CO_2 to CO in the presence of water. The faradaic efficiency increased by 7%, and the turnover frequency 83 times higher using $[\{([Ru]pic)_4cyclen\}NiCl]^{5+}$ than it was using $[ben_4cyclenNiCl]Cl$. The redox-active metal complex transfers electrons to the catalytic active site enhancing the electrocatalytic process. Moreover, due to inductive effects from $[Ru]^+$, the electrocatalyst operated at a lower overpotential. The electrocatalytic abilities of $[ben_4cyclenNiCl]Cl$ are similar to those of $[Ni(cyclam)]^{2+}$, the electrocatalysis process occurs very negative potential. The ligand-coordinated redox-active metal complex causes a decrease in the electrocatalytic potential of about 230 mV in comparison to that using $[ben_4cyclenNiCl]Cl$. Utilizing a redox-active metal complex tethered to the electrocatalytic active site via the supporting ligand is a new way of improving the abilities of an electrocatalyst.

3.8 Experimental Section

General Considerations. All reagents were purchased from TCI (Tokyo, Japan) and used without further purification. Solvents were purchased from Wako and used without further purification. $[Ru(bpy)_2Cl_2]$ was prepared following a reported procedure.[61] ^1H and ^{13}C NMR spectroscopies were performed on a Bruker AV500 and referenced to internal tetramethylsilane. Tetrabutylammonium hexafluorophosphate ($TBAPF_6$, Aldrich, 98%) was recrystallized from hot ethanol and dried in vacue at 90 °C overnight. Mass spectra were acquired on a Waters Xevo G2 Q-TOF spectrometer equipped with electrospray ionization (ESI). Elemental analyses were performed at the Research and Analytical Center for Giant Molecules, Tohoku University.

Characterization and Instrumentation

X-ray Crystallography. For X-ray single crystal structure analysis, single crystals of compounds were mounted on a glass loop rod with paratone-N (Hampton). Data collection were performed on a Rigaku Varimax diffractometer equipped with Saturn724+ CCD detector using graphite monochromated Mo Kα radiation (λ = 0.71073Å) in a N_2 stream. An empirical absorption correction based on azimuthal scans of several reflections was applied. The data were corrected for Lorentz and polarization effects. All non-hydrogen atoms were refined anisotropically using a least-squares method, and hydrogen atoms were fixed at calculated positions and refined using a riding model. SHELXTL was used for structure refinement.

Electrochemistry. Electrochemical experiments were performed using an ALS/HCH Model 620D electrochemical analyser. A glassy carbon (3 mm diameter) electrode was used as a working electrode, Pt wire was used as a counter electrode, and Ag wire was used as a reference electrode. The supporting electrolyte was 0.1 M tetrabutylammonium hexafluorophosphate ($TBAPF_6$) in 5:95 H_2O/CH_3CN (v/v). N_2 and CO_2 gas were bubbled into the solutions at least for 30 min before cyclic voltammetry was performed. All potentials were converted to NHE.

Controlled Potential Electrolysis. Controlled potential electrolysis (CPE) experiments were performed by using an ALS/HCH Model 620D electrochemical analyser. A Gamry five-neck cell was used for all experiments. A cell was equipped with three Ace-Thread ports used for each electrode and two joints used for gas purging and gas collection after electrolysis. A spherical platinum wire was used for the working electrode (surface area 0.94 cm^2). A piece of Pt wire was used for the counter electrode and Ag wire for reference electrode. Both are separated from the bulk solution by the porous frit. The experiment was performed using 0.1 M $TBAPF_6$ in 5 in 5:95 H_2O/CH_3CN (v/v). The solution was purged with CO_2 gas for 30 min before electrolysis. Gas-phase products were sampled using a gas-tight syringe to determine the gasous CO_2 reduction products. A gas chromatograph (Agilent 6890N, 5975C) equipped with Agilent HP-MOLESIEVE, length 30 m, ID, 0.32 mm, film 12 μm columns was used for product identification. Helium (99.99%) was used as the carrier gas, and the *m*/*z* range was 10–100. Gas chromatography calibration curve was prepared using a known volume of CO gas. CPE measurements were performed three times for every sample. The faradic efficiency was calculated by dividing the actual amount of CO produce during control potential experiment (CPE), and the amount of CO expected based on the charge passed during the CPE experiments. The Turnover frequency (TOF) was calculated based on Eq. S1 and Eq. S3. The reported TOF and Faradic efficiency are averaged values.

Synthesis of 1,4,7,10-tetra(4-methylpyridyl)-1,4,7,10-tetraazacyclododecane (pic_4cyclen). 1,4,7,10-tetraazacyclododecane tetrahydrochloride (cyclen·4HCl) (318 mg, 1 mmol) was dissolved in 20 mL deionized water. To the solution, an aqueous solution of 0.2 N NaOH was added to adjust pH to 12. 4-Pyridylmethyl chloride hydrochloride (820 mg, 5 mmol) was added slowly while the pH was maintained at 12. The reaction mixture was stirred for 24 h during this time a pink solid formed. The solid was collected by filtration and washed with 10 mL of water and 10 mL of ether. The compound was recrystallized from dichloromethane and hexane. Yield: 76%. Confirm by crystal structure, ESI-MS: *m/z* 537.34 ($C_{32}H_{40}N_8$). Elemental analysis, calculated for $C_{32}H_{40}N_8$: C, 71.61; H, 7.51; N, 20.88%; found: C, 71.52; H, 7.42; N, 20.53%. ^{1}H NMR ($CDCl_3$, δ): 8.45 (d, 2H), 7.32 (d, 2H), 3.44 (s, 2H), 2.69 (t, 4H). ^{13}C NMR ($CDCl_3$, δ): 53.45 (─N─**C**H$_2$─**C**H$_2$─N─), 59.00 (─N─**C**H$_2$─C─), 149.10 (─CH$_2$─**C**─CH─CH─N─), 123.60 (─C─**C**H─CH─N─), 149.68 (─C─CH─**C**H─N─).

Synthesis of [([Ru]pic$_4$cyclen)]$^{4+}$. Ru(bpy)$_2$Cl$_2$ (452.42 mg, 0.94 mmol) was added to a 50 mL pear-shaped flask containing 5 mL water and 20 mL ethanol. The solution was degassed with N_2 for 10 min before heating for 30 min at 75 °C. pic$_4$cyclen (100 mg, 0.19 mmol) was dissolved in 5 mL ethanol, and the solution was added slowly to the above mixture. The reaction mixture was reflux at 100 °C for 72 h. The solvent was removed using rotary evaporator. The remaining solid was dissolved in a small amount water, and the complex was precipitated by adding excess amount of NH_4PF_6. After removing excess ammonium salt, the solid was purified by using size-exclusion column chromatography through bio-Beads S-X1. ESI-MS (*m/z*): 583.09. Elemental analysis, calculated for $[C_{112}H_{104}Cl_4F_{24}N_{24}P_4Ru_4]\cdot CH_3CH_2OH\cdot 2H_2O$: C, 44.73; H, 3.84; N, 11.23%; found C, 45.69, H, 3.87; N, 11.21%.

Synthesis of [{[Ru]pic$_4$cyclen}NiCl]Cl[PF$_6$]$_4$. [([Ru]pic$_4$cyclen)]$^{4+}$ (291.2 mg, 0.1 mmol) and $NiCl_2\cdot 6H_2O$ (28.45 mg, 0.12 mmol) were added to a 50 mL pear-shaped flask containing 15 mL ethanol. This solution mixture was heated at 75 °C for 6 h. A black-red precipitate formed. The solution was filtered, and the solid was washed with 5 ml ether. The solid was then dried under a vacuum overnight. Elemental analysis, calculated for

$(C_{112}H_{104}Cl_6F_{24}N_{24}NiP_4Ru_4)\cdot 3CH_3CH_2OH\cdot 2H_2O$: C, 44.07; H, 3.95; N, 10.45%; found C, 44.03, H, 3.99; N, 10.48%.

Synthesis of ben$_4$cyclen: ben$_4$cyclen was synthesized following method.[62] 1,4,7,10-tetraazacyclododecane tetrahydrochloride (cyclen·4HCl) (447 mg, 1.5 mmol) and potassium carbonate (2.07 g , 15 mmol) were added to boiling anhydrous acetonitrile (50 mL), the solution of benzylchloride (0.76 mL, 6.6 mmol) in acetonitrile (10 mL) was added dropwise and then reaction mixture was reflux for 12 h. Upon cooling to room temperature, the precipitate was filtered. The solution was evaporate evaporated to dryness. The product was extracted with boiling heptane (2 × 50 mL). The solution was evaporated to dryness under reduced pressure and recrystallized from acetonitrile. Yield 622 mg (77%). Elemental analysis for $C_{36}H_{44}N_4$: C, 81.16; H, 8.32; N, 10.52%. Found: C, 80.99; H, 8.34; N, 10.57 %. ^{1}H NMR ($CDCl_3$, δ): 2.68 (s, 16 H), 3.42 (s, 8H), 7.18─7.36 (m, 20H). ^{13}C NMR ($CDCl_3$, δ): 53.01 (─N─**C**H$_2$─**C**H$_2$─N─), 60.10 (─N─**C**H$_2$─C─), 126.51 (─N─CH$_2$─**C**─), 1128.00 (─CH$_2$─C─**C(O)**H─), 128.91 (─C─CH─**C**(m)H─), 149.68 140.09 (─C─CH─CH─**C(p)**H).

Synthesis of [ben$_4$cyclenNiCl]Cl: ben$_4$cyclen (53 mg, o.1 mmol) and $NiCl_2\cdot 6H_2O$ (28.45 mg, 0.12 mmol) were added to a 50 mL pear-shaped flask containing 20 mL ethanol. The solution was heated at 60 °C for 6 h. A green-yellow color precipitated formed. The solution was filter and wash with small amount of ethanol. The compound was recrystallized from methanol and diethyl ether by slow evaporation. Yield 82%. Elemental analysis. [$C_{36}H_{44}N_4NiCl$]: C, 65.28; H, 6.70; N, 8.46%. Found: C, 64.92; H, 6.72; N, 8.50 %.

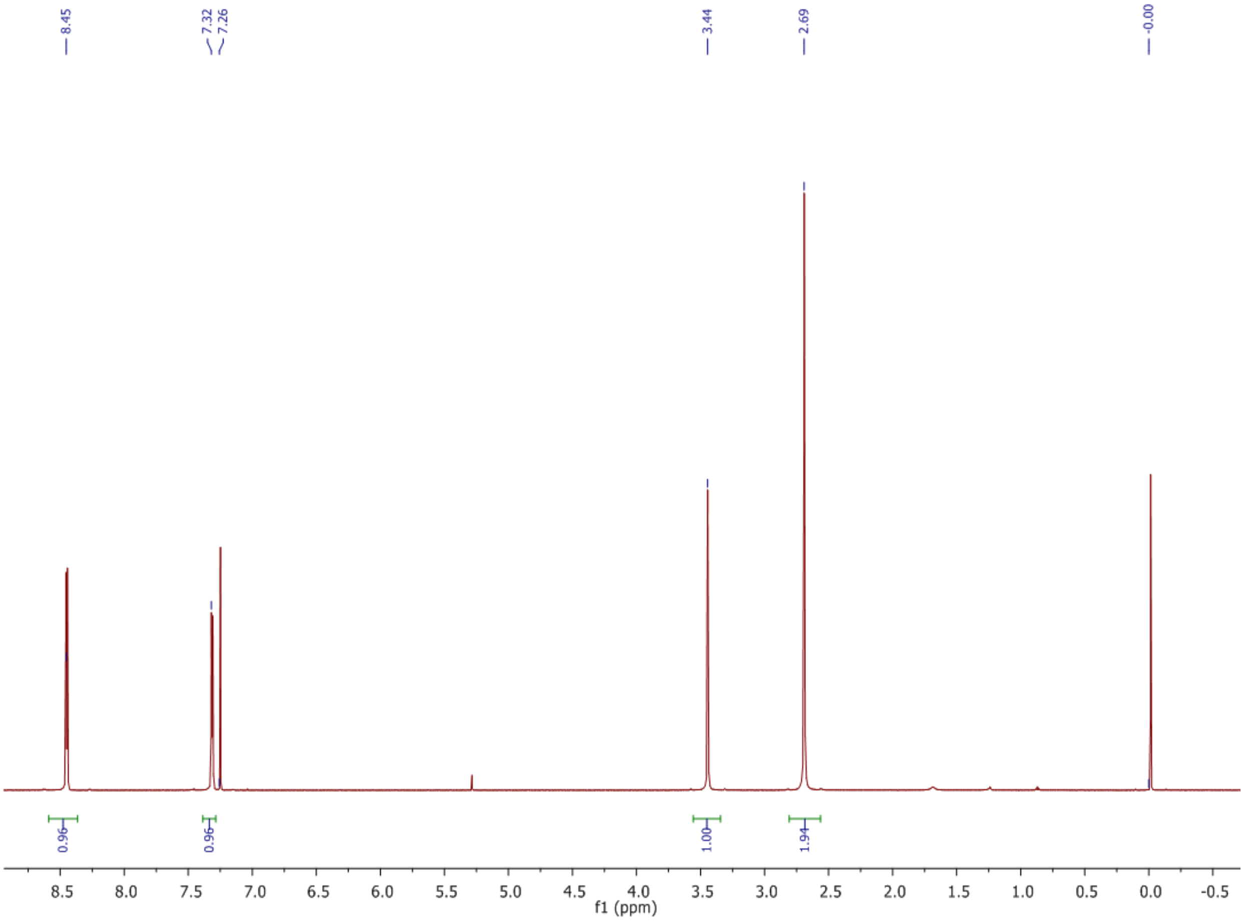

Figure 3.11: ^{1}H NMR spectrum of (pic$_4$cyclen)

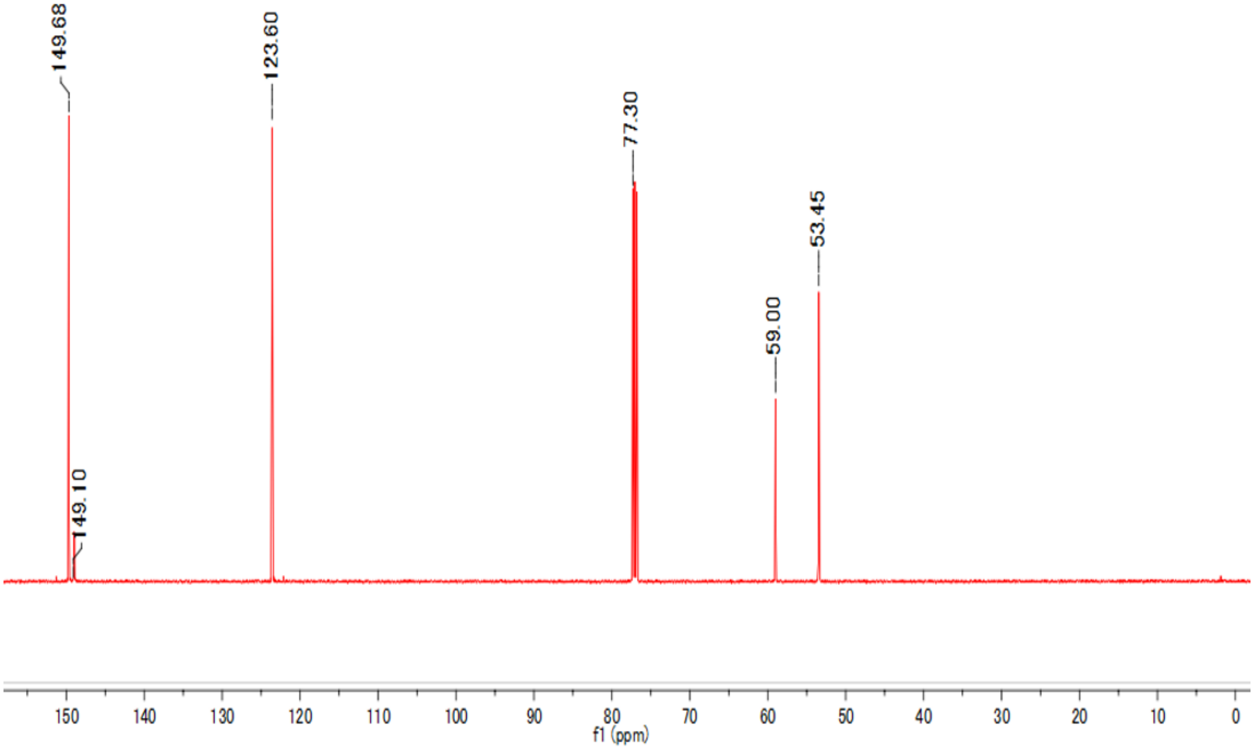

Figure 3.12: ^{13}C NMR spectrum of (pic$_4$cyclen)

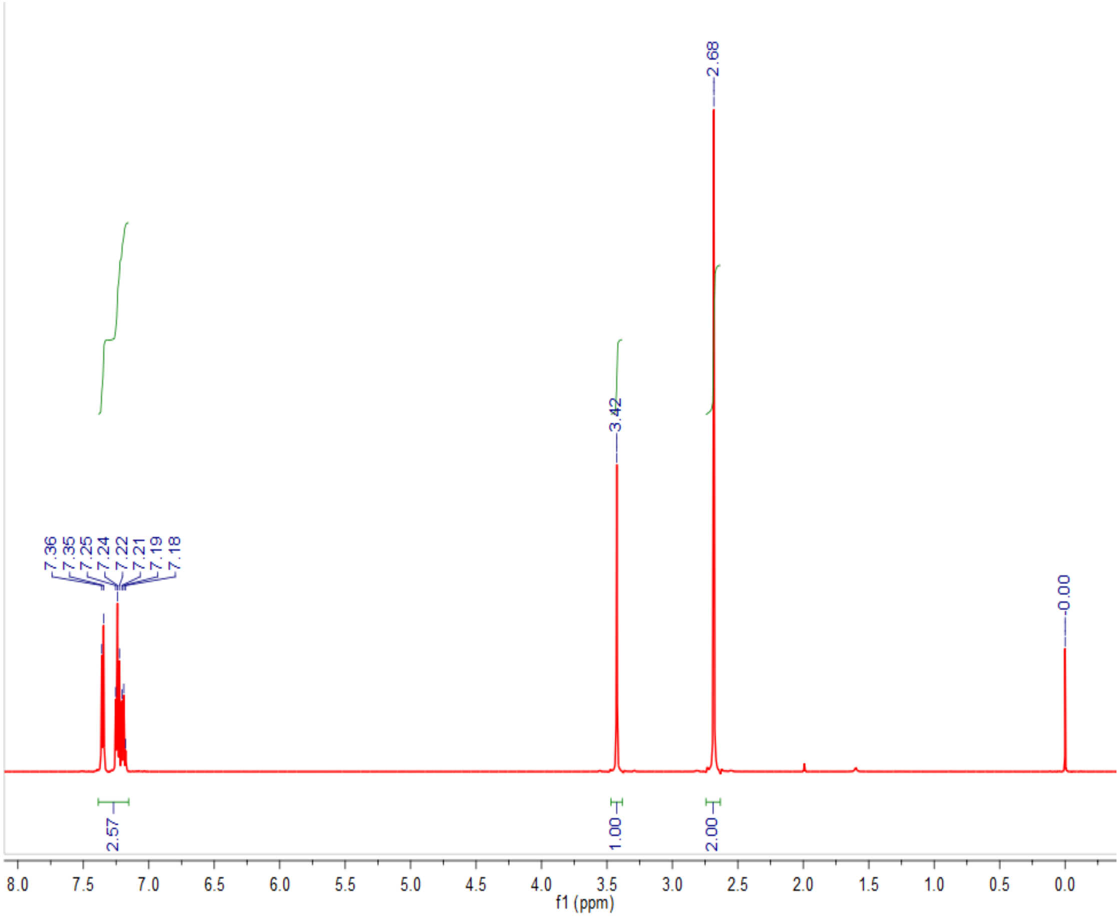

Figure 3.13: ^{1}H NMR spectrum of (ben$_4$cyclen

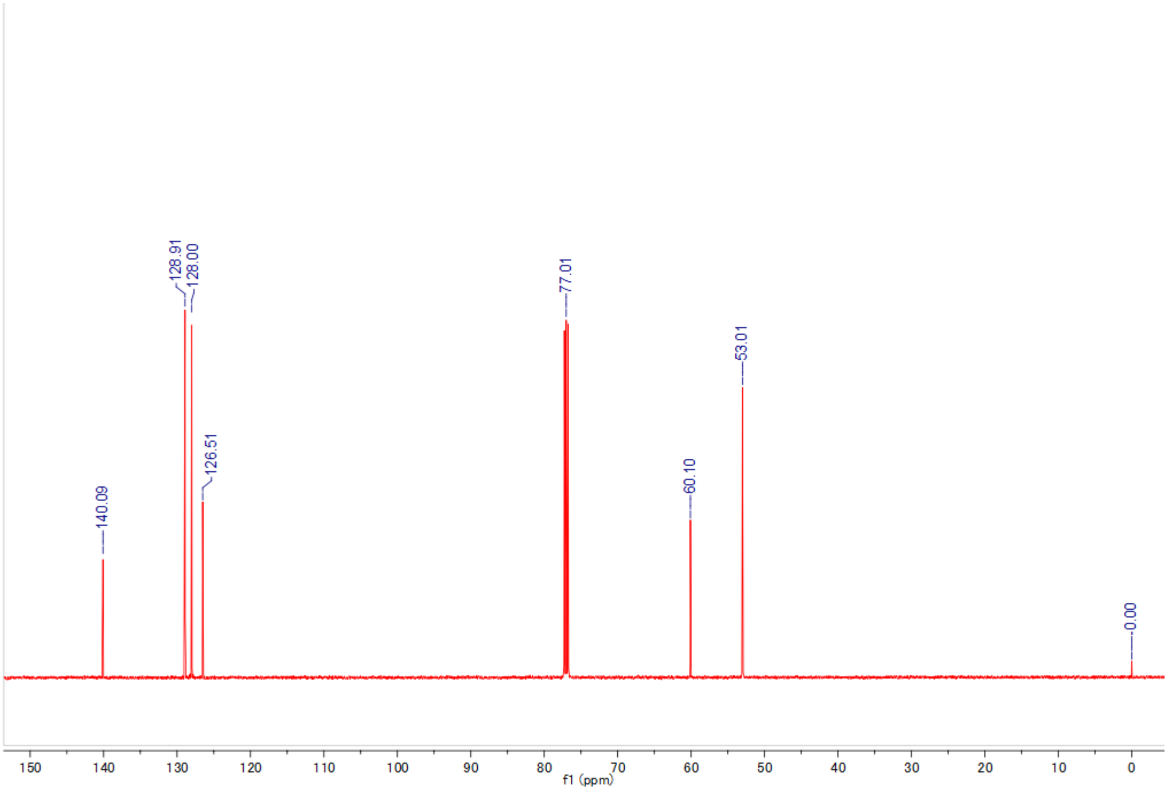

Figure 3.14: ^{13}C NMR spectrum of (ben$_4$cyclen)

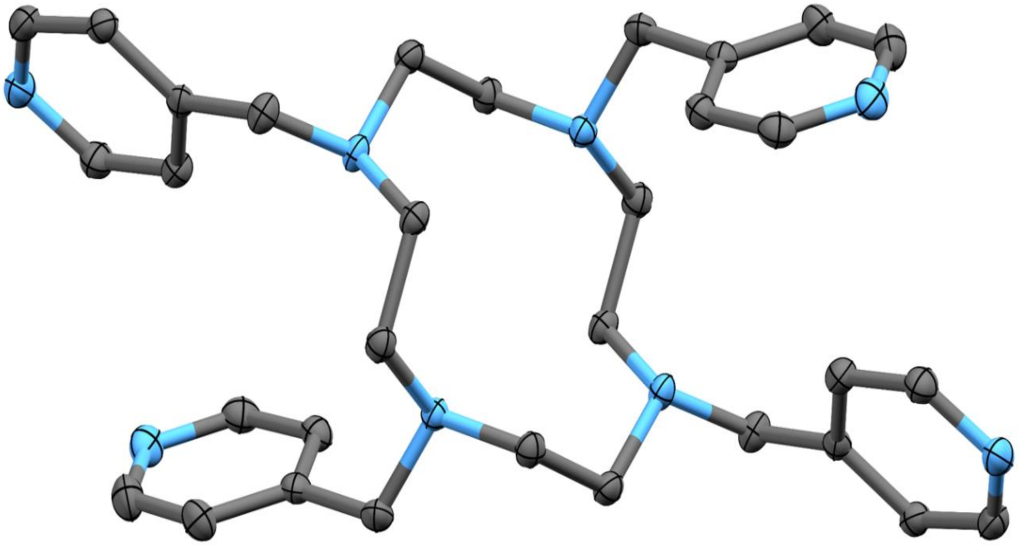

Figure 3.15: ORTEP diagram of (pic)$_4$cyclen with thermal ellipsoid drawn at the 50% probability. Hydrogen atoms are omitted for clarity. Light blue, N; gray, C.

Table 3.2: Crystal data for (pic)$_4$cyclen.

Radiation type, wavelength	Mo Kα, 0.71073
Formula	$C_{32}H_{40}N_8$
Formula weight	536.72
Crystal system	Triclinic
Space group	P–1
a (Å)	9.328(6)
b (Å)	9.338(5)
c (Å)	10.156(6)
α (deg)	95.874(3)
β (deg)	116.949(5)
γ (deg)	108.364(5)
V (Å^3)	716.3(7)
Z	1
T (K)	93
d (g/cm^3)	1.244
μ (mm^{-1})	0.077
R_1, wR_2 [$I > 2\sigma$(I)]	0.0463
R_1, wR_2 [all data]	0.1605
R_{int}	0.0290
F(000)	288
GOF	1.046

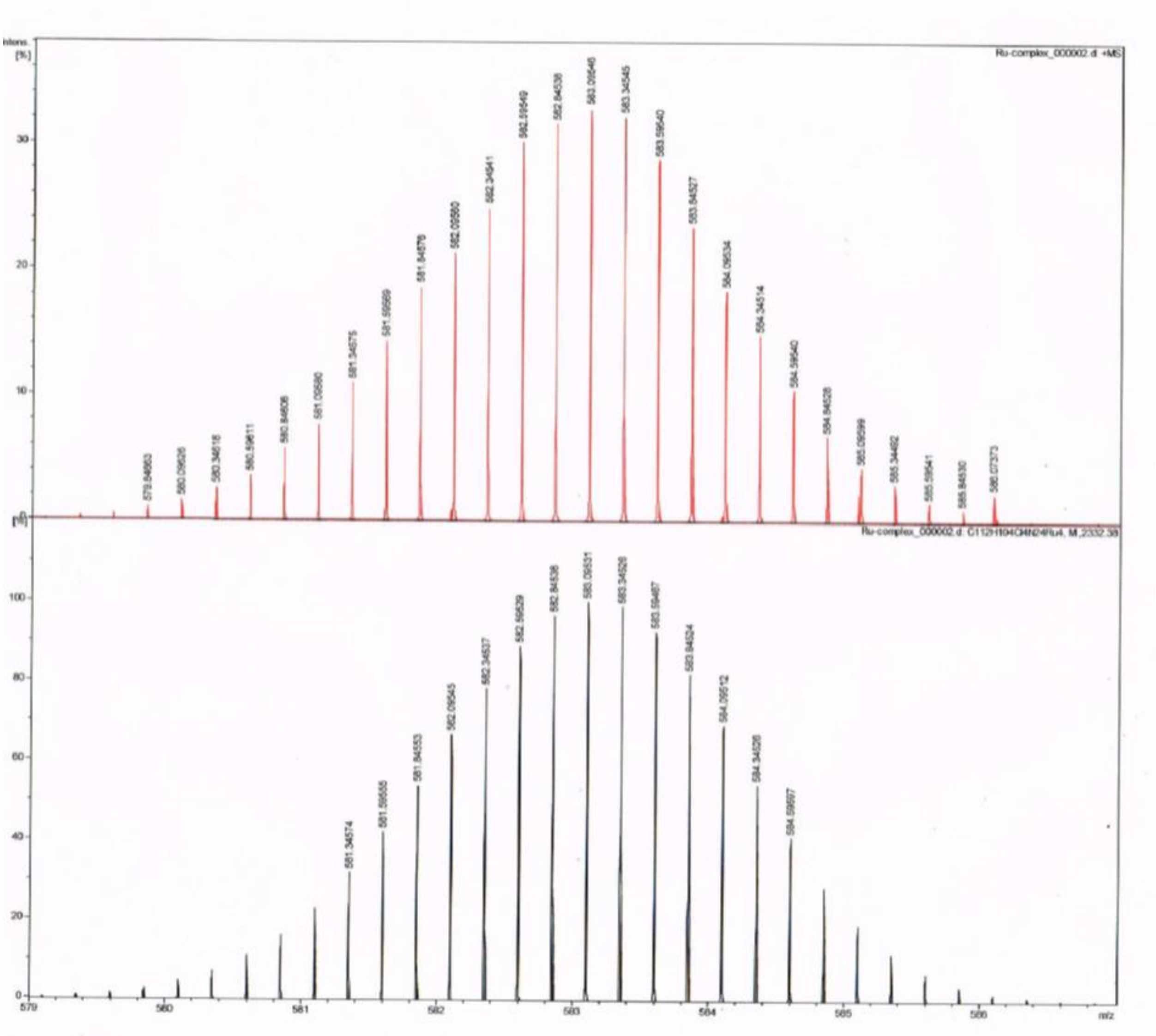

Figure 3.16: ESI-Mass of [([Ru]pic)$_4$cyclen]$^{4+}$

Table 3.3: Crystal data for [ben$_4$cyclenNiCl]Cl.

Radiation type, wavelength (nm)	Mo Kα, 0.71073
Formula	$C_{36}H_{44}N_4NiCl_2$
Formula weight	662.36
Crystal system	Orthorhombic
Space group	$Ccm2_1$
a (Å)	7.7774(8)
b (Å)	25.294(3)
c (Å)	16.4763(17)
α (deg)	95.874(3)
β (deg)	90
γ (deg)	90
V (Å^3)	90
Z	4
T (K)	298(2)
d (g/cm^3)	1.357
μ (mm^{-1})	0.795
R_1, wR_2 [$I > 2\sigma(I)$]	0.0530, 0.1327
R_1, wR_2 [all data]	0.0714, 0.1428
$F(000)$	1400
GOF	0.998

.

The diffusion coefficient D calculation of $[\{([Ru]pic)_4cyclen\}NiCl]^{5+}$

The relationship between the cathodic peak current (i_p) and square root of the scan rate is given by the Randles-Sevcik equation for a homogeneous system.[63]

$$i_p = 0.4463 n_p F A [cat] (n_p F v D / RT)^{1/2} \qquad \text{Eq. S1}$$

where i_p is peak current (A), n_p is the number of electron(s) involved in the redox system (1 for $Ni^{II/I}$ redox process), F is the Faraday constant (96500 $C \cdot mol^{-1}$), A is the surface area of working electrode (0.071 cm^2), $[cat]$ is catalysts concentration ($mol \cdot cm^{-3}$), v is the scan rate ($V \cdot s^{-1}$), R is the universal gas constant (8.31 $J \cdot K^{-}1 \cdot mol^{-1}$), and T is the temperature (298 K). The diffusion coefficient D is calculated from the slop of i_p vs. $v^{1/2}$ plot.

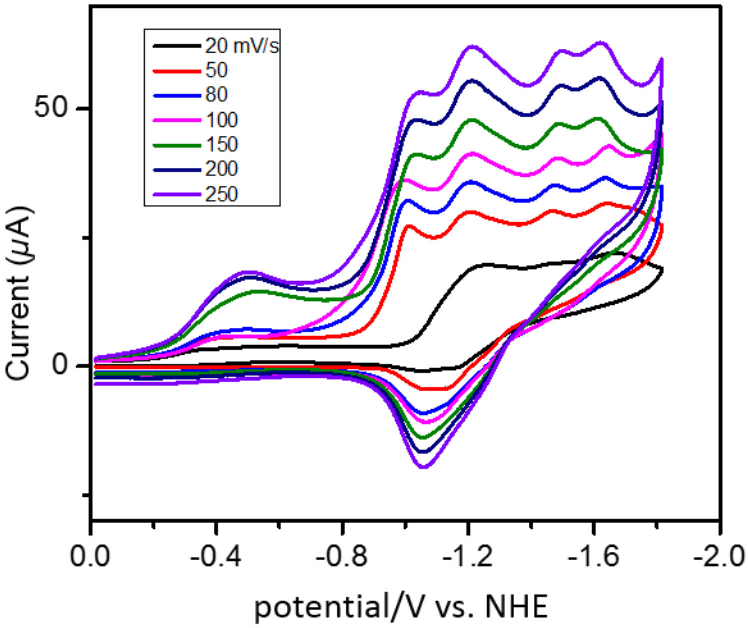

Figure 3.17: Cyclic voltammograms of $[\{([Ru]pic)_4cyclen\}NiCl]^{5+}$ in CH_3CN containing 0.1 M $TBAPF_6$ at different scan rates. The $Ni^{II/I}$ couple was used as the cathodic peak current.

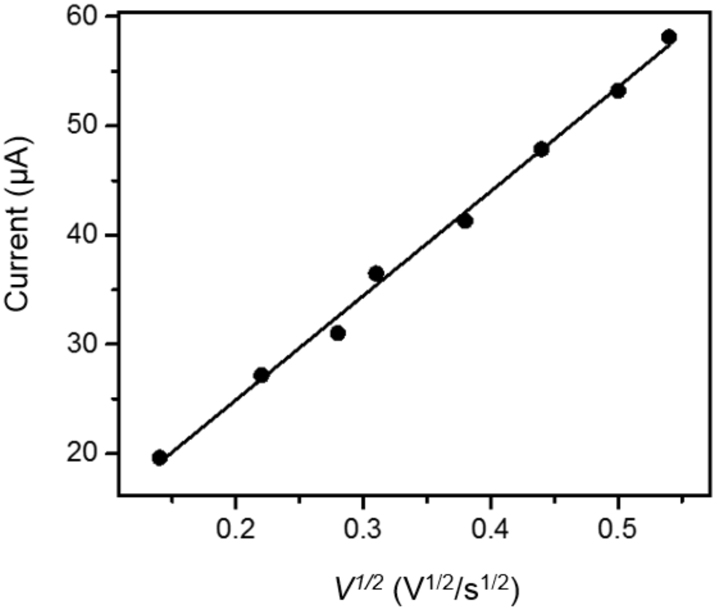

Figure 3.18: Plot of i_p vs. $v^{1/2}$ for [{([Ru]pic)$_4$cyclen}NiCl]$^{5+}$, data collected from Figure S7. Peak current consider for Ni$^{II/I}$ reduction couples at corresponding scan rate. The current showing a linear dependence on scan rate, indicating that the reduction of for [{([Ru]pic)$_4$cyclen}NiCl]$^{5+}$ is a diffusion-controlled process.

The diffusion coefficient for for [{([Ru]pic)$_4$cyclen}NiCl]$^{5+}$ calculated using Eq. S1 to be 1.95 × 10^{-5} cm^2·s^{-1}.

Turnover frequency (TOF) Calculation Methods

In this work TOF values were calculate using two methods. The first method uses the classical definition of the TOF (eq. S2) and the TOF is only a rough estimate.

$$\mathrm{TOF}_{\,a} = \frac{\frac{n[CO]}{n[cat]}}{t} \qquad \text{Eq. S2}$$

where, n[CO] is the total number of mole CO generate during electrolysis (from GC-MS measurement), n[cat] is the number of moles of catalysts in solution for using for electrolysis and t is the electrolysis time in seconds.

The second method for calculating TOF uses cyclic voltammogram and control potential electrolysis data.[64–66]

$$\mathrm{TOF}_{\mathrm{b}} = \frac{(i_{el})^2\ (1 + exp\left[\frac{F}{RT}\left(E_{app} - E_{\frac{1}{2}}\right)\right])}{F^2A^2D[cat]^2} \qquad \text{Eq. S3}$$

where, i_{el} is average current of CPE for CO generation (A), F is Faraday constant (96500 C·mol), R is the universal gas constant (8.31 $\mathrm{J{\cdot}K^{-1}{\cdot}mol^{-1}}$), T is the temperature (298 K), E_{app} is the applied potential during CPE, $E_{1/2}$ is the standard redox potential of catalyst, A is the surface area of working electrode(0.94 $\mathrm{cm^2}$), D is the diffusion coefficient for catalyst ($\mathrm{cm^2{\cdot}s}$) and [cat] is the concentration of catalyst in solution ($\mathrm{mol{\cdot}cm^{-3}}$).

The Faradaic efficiency (FE) using the following equation:

$$\mathrm{n[CO]} = \frac{Q_{el} \times FE}{nF} \qquad \text{Eq. S4}$$

where, n[CO] is the number of mole of CO generated from electrolysis (A), Q_{el} is the charge passed during electrolysis (C) and F is Faraday constant (96500 $\mathrm{C{\cdot}mol^{-1}}$) and n is number of electron needed for conversion of CO_2 to CO (2 electron process).

The average current i_{el} for CO generation during electrolysis is calculated from equation

$$i_{el} = \frac{Q_{el} \times FE}{t} \qquad \text{Eq. 5}$$

where, Q_{el} is the charge passed during electrolysis (C), FE is Faradaic efficiency of CO (%) and t (s) is time of electrolysis.

TOF using [{([Ru]pic)$_4$cyclen}NiCl]$^{5+}$ in 5:95 H_2O CH_3CN (v/v)

Using data from CPE experiments with in 5 mL solution. So, the catalysts concentration in solution was 4.90×10^{-7} mol·cm^{-3}. The GC-MS analysis confirmed that the CO_2 reduction product was CO in gaseous state. The amount of CO generated was 3.23×10^{-3} mol. So, the TOF$_a$ was calculated to be 2.64×10^{-2} s^{-1} by using Eq. S2.

Faradaic efficiency

The Faradaic efficiency is defined as the ratio of the actual amount of CO produce during CPE electrolysis and the amount of CO expected based on charge passed during CPE.

$$\mathrm{n[CO]} = \frac{Q_{el} \times FE}{nF} \qquad \text{Eq. S4}$$

$$FE = \frac{n[CO] \times nF}{Q_{el}} \qquad \text{Eq. S4.1}$$

Where, n[CO] is 2.33×10^{-3} mol, n is 2 (reduce CO_2 to CO needed 2 electron), *F* is faraday constants 96500 C·mol and Q_{el} is charge passed during CPE 6.08 C.

Using Eq. S4.1 the Faradaic efficiency was calculated to be 84%.

TOF_b calculation

$$\mathrm{TOF}_{\mathrm{b}} = \frac{(i_{el})^2\ (1 + exp\left[\frac{F}{RT}\left(E_{app} - E_{\frac{1}{2}}\right)\right])}{F^2 A^2 D[cat]^2} \qquad \text{Eq. S3}$$

Where, i_{el} is the average current value based on Faradaic efficiency (84%) during CPE and calculated by using

$$i_{el} = \frac{Q_{el} \times FE}{t} \qquad \text{Eq. S5}$$

Q_{el} value is 8.06 C, *FE* value is 84% and t is CPE time 1800 s. The i_{el} calculated to be 2.83×10^{-3} A. The *F* is Faraday constant (96500 $C{\cdot}mol^{-1}$), *A* is the surface area of glassy carbon working electrode (0.94 cm^2), *D* is the diffusion coefficient (1.95×10^{-5} $cm^2{\cdot}s^{-1}$), *R* is universal gas constant (8.31 $J{\cdot}K^{-1}{\cdot}mol^{-1}$), *T* is the temperature (298 K), E_{app} is the applied potential of CPE (–1.22 V vs. NHE) and the $E_{1/2}$ is the standard redox potential of catalyst (–1.26 V vs. NHE). Using those above value in Eq. S3, the TOF_b for the $[\{([Ru]pic)_4cyclen\}Ni^{II}]^{6+}$ catalysts in 5% H_2O and CH_3CN solution was calculated to be 708 s^{-1}.

References

1. K. L. Materna, R. H. Crabtree and G. W. Brudvig, *Chem. Soc. Rev.*, 2017, **46**, 6099–6110.
2. J. Qiao, Y. Liu, F. Hong and J. Zhang, *Chem. Soc. Rev.*, 2014, **45**, 631–675.
3. M. Aresta and A. Dibenedetto, *Dalton Trans.*, 2007, 2975–2992.
4. J. Albo, M. A. Guerra, P. Castano and A. Irabien, *Green Chem.*, 2015, **17**, 2304–2324.
5. H. Takeda, C. Cometto and O. Ishitani, M. Robert, *ACS. Catal.*, 2017, **7**, 70–88.
6. K. T. Ngo, M. McKinnon, B. Mahanti, R. Narayanan, D. C. Grills and M. Z. Ertem, J. Rochford, *J. Am. Chem. Soc.,* 2017, **139**, 2604–2618.
7. M. L. Clark, K. A. Grice, C. E. Moore, A. Rheingold and C. P. Kubiak, *Chem. Sci.*, 2014, **5**, 1894–1900.
8. C. W. Machan, S. A. Chabolla and C. P. Kubiak, *organometallics*, 2015, **34**, 4678–4683.
9. G. Neri, I. M. Aldous, J. J. Walsh, L. J. Hardwick and A. J. Cowan, *Chem. Sci.*, 2016, **7**, 1521–1526.
10. C. Costentin, S. Drouet, M. Robert and J. M. Saveant, *Science*, 2012, **338**, 90–94.
11. M. Hammouche, D. Lexa, M. Momenteau and J. M. Saveant, J. Am. Chem. Soc., 1991, **113**, 8455–8466.
12. M. D. Sampson and C. P. Kubiak, *J. Am. Chem. Soc.*, 2016, **138**, 1386–1396.

13. J. M. Smieja, M. D. Sampson, K. A. Grice, E. E. Benson, J. D. Froehlich and C. P. Kubiak, *Inorg. Chem*., 2013, **52**, 2484–2491.
14. M. D. Sampson, A. D. Nguyen, K. A. Grice, C. E. Moore, A. L. Rheingold and C. P. Kubiak, *J. Am. Chem. Soc.*, 2014, **136**, 5460–5471.
15. C. Riplinger, M. D. Sampson, A. M. Ritzmann, C. P. Kubiak and A. E. Carter, J. Am. Chem. Soc., 2014, 136, 16285–16298.
16. K. T. Ngo, M. McKinnon, B. Mahanti, R. Narayanan, D. C. Grills and M. Z. Ertem, J. Rochford, *J. Am. Chem. Soc.*, 2017, **139**, 2604–2618.
17. C. W. Machan, M. D. Sampson and C. P. Kubiak, *J. Am. Chem. Soc.,* 2015, **137**, 8564–8571.
18. M. L. Clark, K. A. Grice, C. E. Moore, A. Rheingold and C. P. Kubiak, *Chem. Sci*., 2014, **5**, 1894–1900.
19. G. Neri, I. M. Aldous, J. J. Walsh, L. J. Hardwick and A. J. Cowan, *Chem. Sci.,* 2016, **7**, 1521–1526.
20. C. Costentin, S. Drouet, M. Robert and J. M. Saveant, *Science,* 2012, **338**, 90–94.
21. C. W. Machan, S. A. Chabolla and C. P. Kubiak, *organometallics,* 2015, **34**, 4678–4683.
22. S. A. Chabolla, E. A. Dellamary, C. W. Machan, F. A. Tezcan, and C. P. Kubiak , *Inorganica Chimica Acta,* 2014, **422**, 109–113.
23. K. A. Grice and C. P. Kubiak, *Inorg. Chem.,* 2016, 55, 6240–6246.

24. M. L. Clark, B. Rudshteyn, A. Ge, A. S. Chabolla, C. W. Machan, B. T. Psciuk, J. Song, G. Canzi, T. Lian, V. S. Batista and C. P. Kubiak, *J. Phy. Chem. C*, 2016, **120**, 1657–1665.

25. S. A. Chabolla, C. W. Machan, J. Yin, E. A. Dellamary, S. Sahu, N. C. Gianneschi, M. K. Gilson, F. A. Tezcan and C. P. Kubiak, *Faraday Discuss.*, 2017, **198**, 279–300.

26. C. W. Machan, J. Yin, S. A. Chabolla, M. K. Gilson and C. P. Kubiak et al., *J. Am. Chem. Soc.,* 2016, **138**, 8184–8193

27. C. W. Machan, C. J. Stanton, J. E. Vandezande, G. F. Majetich, H. F. Schaefer, C. P. Kubiak and J. Agarwal, *Inorg. Chem*., 2015, **54**, 8894–8856

28. M. V. Vollmer, C. W. Machan, M. L. Clark, W. E. Antholine, J. Agarwal, H. F. Schaefer, C. P. Kubiak and J. R. Walensky, *Organometallics*, 2015, **34**, 3–12.

29. C. W. Machan and C. P. Kubiak, *Dalton Trans.,* 2016, **45**, 17179–17186.

30. I. Bhugun, D. Lexa and J. M. Saveant, *J. Am. Chem. Soc.*, 1996, **118**, 1769–1776.

31. J. Grodkowski, P. Neta, E. Fujita, A. Mahammed, L. Simkhovich and Z. Gross, *J. Phys. Chem. A*, 2002, **106**,4774–4778.

32. C. M. Lieber and N. S. Lewis, *J. Am. Chem. Soc.*, 1984, **106**, 5033–5034.

33. E. Simon-Manso and C. P. Kubiak, *Organometallics*, 2005, **24**, 90–102.

34. M. Rakowski Dubois and D. L. Dubois, *Acc. Chem. Res.*, 2009, **42**, 1974–1982.

35. P. Kang, C. Cheng, Z. Chen, C. K. Schauer, T. J. Meyer and M. Brookhart, *J. Am. Chem. Soc.*, 2012, **134**, 5500–5503.

36. S. Meshitsuka, M. Ichikawa and K. Tamaru, *J. Chem. Soc., Chem. Commun.*, 1974, **0**. 158–159.

37. B. Fisher and R. Eisenberg, *J. Am. Chem. Soc.*, 1980, **102**, 7361–7363.

38. M. Beley, J. P. Collin, R. Ruppert and J. P. Sauvage, *J. Am. Chem. Soc*., 1986, **108**, 7461–7467.

39. G. B. Balazs and F. C. Anson, *J. Electroanal. Chem.*, 1993, **361**, 149–157.

40. J. D. Froehlich and C. P. Kubiak, *Inorg. Chem.*, 2012, **51**, 3932–3934.

41. J. D. Froehlich and C. P. Kubiak, *J. Am. Chem. Soc.*, 2015, **137**, 3565–3573.

42. J. Schneider, H. Jia, K. Kobiro, D. E. Cabelli, J. T. Muckerman and E. Fujita, *Energy Environ. Sci.*, 2012, **5**, 9502–9510.

43. G. Neri, I. M. Aldous, J. J. Walsh, L. J. Hardwick and A. J. Cowan, *Chem. Sci*., 2016, **7**, 1521–1526.

44. B. K. Burgess and D. J. Lowe et al., *Chem. Rev.*, 1996, **96**, 2983–3011.

45. V. O. Gelmboldt, E. V. Ganin, S. S. Basok, E. Y. Kulygona, M. M. Botoshansky, V. C. Kravtsov and M. S. Fonari, *CrystEngComm*, 2011, **13**, 3682–3685.

46. E. Kimura, X. Bu, M. Shionoya, S. Wada and S. Maruyama, *Inorg. Chem.*, 1992, **31**, 4542–4546.

47. I. Azcarate, C. Costentin, M. Robert and J. M. Saveant, *J. Am. Chem. Soc.*, 2016, **138**, 16639–16644.

48. J. W. Raebiger, J. W. Turner, B. C. Noll, C. J. Curtis, A. Miedaner, B. Cox and D. L. DuBois, *Organometallics*, 2006, **25**, 3345–3351.

49. Z. Chen. C. Chen, D. R. Weinberg, P. Kang, J. J. Concepcion, D. P. Harrison, M. S. Brookhart and T. Meyer, *J. Chem. Commun*., 2011, **47**, 12607–11609.

50. C. Costentin, and J. M. Saveant, *ChemElectroChem*, 2014, **1**, 1226–1236.

51. C. Cometto, L. Chen, P. K. Lo, Z. Guo, K. C. Lau, E. A. Mallart, A. Fave, T C. Lau and M. Robert, *ACS Catal.*, 2018, **8**, 3411–3417.

52. C. Costentin, M. Robert and J. M. Saveant, *Acc. Chem. Res*., 2015, **48**, 2996–3006.

53. C. Costentin, S. Drouet, M. Robert and J. M. Saveant, *J. Am. Chem. Soc*. 2012, **134**, 11235–11242.

54. I. Azcarate, C. Costentin, M. Robert and J. M. Saveant, *J. Phy. Chem. C*. 2016, **120**, 28951–28960.

55. J. Song, E. L. Klein, F. Neese and S. Ye, *Inorg. Chem*., 2014, **53**, 7500–7507.

56. J. Schneider, H. Jia, J. T. Muckerman and E. Fujita, *Chem. Soc. Rev*., 2012, **41**, 2036–2051.

57. S. Sakaki, N. Koga and K. Morokuma, *Inorg. Chem*., 1990, **29**, 3110–3116.

58. A. Dedieu and F. Ingold, *Angew. Chem., Int. Ed. Engl.*, 1989, **28**, 1694–1995.

59. C. Costentin, M. Robert and J. M. Saveant, *Chem. Rev.*, 2010, **110**, PR1–PR40.

60. S. Hammes-Schiffer, *Energy Environ. Sci.*, 2012, **5**, 7696–7703.

61. G. A. Lawrance, D. R. Stranks and S. Suvachittanont, *Inorg. Chem.*, 1978, **17**, 3322–3325.

62. V. O. Gelmboldt, E. V. Ganin, S. S. Basok, E. Y. Kulygona, M. M. Botoshansky, V. C. Kravtsov and M. S. Fonari, *CrystEngComm*, 2011, **13**, 3682–3685.

63. A. J. Bard, L. R. Faulkner, Electrochemical Methods: *Fundamentals and Applications*, 2nd ed., John Wiley, New York, 2001.

64. W. Nie, C. C. L. McCrory, *Chem. Commun*., 2018, **54**,1579–1582.

65. C. Costentin, S. Drouet, M. Robert and J. M. Saveant, *Science*, 2012, **338**, 90–94.

66. C. Costentin, M. Robert and J. M. Saveant, *Chem. Soc. Rev.*, 2013, **42**, 2423–2436.